

Handbook for Designing MMOD Protection

Astromaterials Research and Exploration Science Directorate
Human Exploration Science Office
NASA Johnson Space Center

Dr. Eric L. Christiansen
MMOD Protection Lead
NASA Johnson Space Center
Houston, TX 77058

Co-Authors and Contributors:
Jim Arnold, University of California at Santa Cruz
Alan Davis, ESCG, NASA Johnson Space Center
James Hyde, ESCG, NASA Johnson Space Center
Dana Lear, NASA Johnson Space Center
J.-C. Liou, Ph.D., NASA Johnson Space Center
Frankel Lyons, ESCG, NASA Johnson Space Center
Thomas Prior, ESCG, NASA Johnson Space Center
Martin Ratliff, Ph.D., NASA Jet Propulsion Laboratory
Shannon Ryan, Ph.D., Lunar and Planetary Institute
Frank Giovane, Virginia Tech
Bob Corsaro, Naval Research Lab
George Studor, NASA Johnson Space Center

THE NASA STI PROGRAM OFFICE . . . IN PROFILE

Since its founding, NASA has been dedicated to the advancement of aeronautics and space science. The NASA Scientific and Technical Information (STI) Program Office plays a key part in helping NASA maintain this important role.

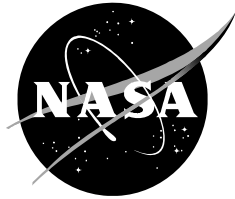
The NASA STI Program Office is operated by Langley Research Center, the lead center for NASA's scientific and technical information. The NASA STI Program Office provides access to the NASA STI Database, the largest collection of aeronautical and space science STI in the world. The Program Office is also NASA's institutional mechanism for disseminating the results of its research and development activities. These results are published by NASA in the NASA STI Report Series, which includes the following report types:

- **TECHNICAL PUBLICATION.** Reports of completed research or a major significant phase of research that present the results of NASA programs and include extensive data or theoretical analysis. Includes compilations of significant scientific and technical data and information deemed to be of continuing reference value. NASA's counterpart of peer-reviewed formal professional papers but has less stringent limitations on manuscript length and extent of graphic presentations.
- **TECHNICAL MEMORANDUM.** Scientific and technical findings that are preliminary or of specialized interest, e.g., quick release reports, working papers, and bibliographies that contain minimal annotation. Does not contain extensive analysis.
- **CONTRACTOR REPORT.** Scientific and technical findings by NASA-sponsored contractors and grantees.
- **CONFERENCE PUBLICATION.** Collected papers from scientific and technical conferences, symposia, seminars, or other meetings sponsored or cosponsored by NASA.
- **SPECIAL PUBLICATION.** Scientific, technical, or historical information from NASA programs, projects, and mission, often concerned with subjects having substantial public interest.
- **TECHNICAL TRANSLATION.** English-language translations of foreign scientific and technical material pertinent to NASA's mission.

Specialized services that complement the STI Program Office's diverse offerings include creating custom thesauri, building customized databases, organizing and publishing research results . . . even providing videos.

For more information about the NASA STI Program Office, see the following:

- Access the NASA STI Program Home Page at <http://www.sti.nasa.gov>
- E-mail your question via the internet to help@sti.nasa.gov
- Fax your question to the NASA Access Help Desk at (301) 621-0134
- Telephone the NASA Access Help Desk at (301) 621-0390
- Write to:
NASA Access Help Desk
NASA Center for AeroSpace Information
7115 Standard
Hanover, MD 21076-1320



Handbook for Designing MMOD Protection

Astromaterials Research and Exploration Science Directorate
Human Exploration Science Office
NASA Johnson Space Center

Dr. Eric L. Christiansen
MMOD Protection Lead
NASA Johnson Space Center
Houston, TX 77058

Co-Authors and Contributors:
Jim Arnold, University of California at Santa Cruz
Alan Davis, ESCG, NASA Johnson Space Center
James Hyde, ESCG, NASA Johnson Space Center
Dana Lear, NASA Johnson Space Center
J.-C. Liou, Ph.D., NASA Johnson Space Center
Frankel Lyons, ESCG, NASA Johnson Space Center
Thomas Prior, ESCG, NASA Johnson Space Center
Martin Ratliff, Ph.D., NASA Jet Propulsion Laboratory
Shannon Ryan, Ph.D., Lunar and Planetary Institute
Frank Giovane, Virginia Tech
Bob Corsaro, Naval Research Lab
George Studor, NASA Johnson Space Center

Available from:

NASA Center for AeroSpace Information
7115 Standard Drive
Hanover, MD 21076-1320
301-621-0390

National Technical Information Service
5285 Port Royal Road
Springfield, VA 22161
703-605-6000

This report is also available in electronic form at <http://ston.jsc.nasa.gov/collections/TRS/>

Table of Contents

Table of Contents	i
List of Figures.....	iv
List of Tables	vii
Acronyms and Abbreviations	viii
Glossary of Terms.....	x
Contributions.....	xii
1 Introduction	1
1.1 MMOD Shielding Background	2
1.2 MMOD Trade Space.....	3
1.2.1 Mission Duration and Spacecraft Size	3
1.2.2 Mission Phases and MMOD Environment Models	4
1.2.3 Required Level of Protection	4
1.2.4 Type of Shielding.....	5
1.2.5 Flight Attitude	5
1.2.6 Failure Criteria.....	5
1.2.7 Impact Damage Detection and Location.....	6
1.2.8 Risk Reduction and Optimization.....	6
1.3 Organization of the MMOD Protection Handbook	7
2 MMOD Protection Design Process	8
2.1 Spacecraft Geometry Model	8
2.2 Failure Criteria	10
2.3 Ballistic Limit Equations.....	12
2.4 Hypervelocity Impact Tests.....	13
2.5 Analysis and Simulation	14
2.6 MMOD Environment Models.....	15
2.6.1 Micro-Meteoroid Environment Model	15
2.6.2 Orbital Debris Environment Model	15
2.6.3 Lunar Secondary Ejecta Environment Model	16
2.7 MMOD Risk Assessment Tools: <i>Bumper</i> Code	16
2.8 Spacecraft Operating Parameters	17
2.8.1 Duration	17
2.8.2 Spacecraft Orientation	17
2.8.3 Orbital Altitude	19
2.8.4 Year of Mission	19
2.8.5 Orbit Inclination.....	20
2.9 Spacecraft Operational Methods to Reduce MMOD Risk	21
2.9.1 Collision Warning and Debris Avoidance	21
2.9.2 Hatch Protocol	21
2.9.3 Damage Detection and Mitigation	21
2.10 MMOD Protection Requirements	22
2.10.1 Requirements Influence on MMOD Protection Capability	23
2.11 Iteration of Analysis Process to Meet MMOD Protection Requirements.....	24

2.11.1	Find MMOD Risk Drivers.....	24
2.11.2	Re-Examine Analysis Assumptions for Risk Drivers.....	24
2.11.3	Incorporate Directional Shielding.....	24
2.11.4	Reduce MMOD Risk by Maximizing Shadowing.....	25
2.11.5	Reduce MMOD Risk by Changing Spacecraft Orientation.....	25
2.11.6	Improve Shielding Performance.....	25
2.11.7	Implement Advanced Shielding.....	26
2.11.8	Incorporate Toughened Multi-Layer Insulation Thermal Blanket.....	27
2.11.9	Inert Stored Energy Equipment.....	28
2.11.10	Reduce Hazards if Shield Penetration Occurs.....	28
2.11.11	Critical Damage Detection, Repair, and Replacement.....	28
2.12	MMOD Risk Reduction Opportunities During Spacecraft Operations.....	28
3	Applications	29
3.1	Changing Shuttle Orientation while Docked to ISS.....	29
3.2	Late Inspection of Space Shuttle WLE and NC for MMOD Damage.....	30
3.3	Shuttle Impact Sensors and On-Orbit Repair.....	31
4	Equations for Designing MMOD Shields	33
4.1	Single-Wall Shielding.....	34
4.1.1	Aluminum Monolithic Shields.....	34
4.1.2	Titanium Monolithic Shield.....	37
4.1.3	Stainless Steel Monolithic Shield.....	39
4.1.4	Carbon-Fiber Reinforced Plastic Single-Wall Shields.....	39
4.1.5	Fiberglass Composite Single-Wall Shields.....	41
4.1.6	Effect of MLI on Ballistic Limits.....	42
4.2	Dual-Wall Whipple Shield.....	42
4.2.1	Impact Physics.....	43
4.2.2	Whipple Shield Design Equations.....	46
4.2.3	Whipple Shield Performance Equations.....	47
4.2.4	Whipple Shield Performance Equations as Function of Bumper Thickness.....	49
4.2.5	Effect of MLI on Whipple Shield Performance Equations.....	50
4.2.6	Performance Equations for ISS Whipple Shields.....	51
4.2.7	Performance Equations for ISS Node Whipple Shields.....	53
4.3	Triple-Wall: Nextel/Kevlar Stuffed Whipple Shield.....	58
4.3.1	Stuffed Whipple Shield Design Equations.....	58
4.3.2	Stuffed Whipple Shield Performance Equations.....	60
4.4	All-Aluminum Triple-Wall Shield.....	65
4.5	Multi-Shock Shields.....	66
4.5.1	Multi-Shock Shield Design Equations.....	68
4.5.2	Performance Equations for MS Shields with Aluminum Rear Wall.....	69
4.5.3	Performance Equations for MS Shields with Kevlar Rear Wall.....	72
4.6	Hybrid MS Shield.....	74
4.7	Mesh Double-Bumper Shield.....	76
4.7.1	MDB Shield Design Equations.....	78
4.7.2	MDB Shield Performance Equations.....	79
5	Equations for Predicting Protection Limits of Thermal Protection System Materials.....	81
5.1	TPS Failure Criteria.....	81

5.2	Low-Density Ceramic Tile Penetration Equations.....	81
5.2.1	LI-900 and LI-2200 Tile Penetration Equations.....	81
5.2.2	TUFI-coated AETB-8 Tile Penetration Equations.....	83
5.3	Tile and Aluminum Substructure Penetration Equations.....	84
5.4	Tile and Composite Honeycomb Substructure Penetration Equations.....	87
5.5	Penetration Equations for Insulated Aluminum Rear Wall behind Tile and Composite Substrate.....	88
5.6	Advanced Flexible Reusable Surface Insulation Blanket Penetration Equation.....	90
5.7	AFRSI and Composite Honeycomb Substructure Penetration Equations.....	90
5.8	Penetration Equations for Insulated Aluminum Rear Wall behind AFRSI Blanket and Composite Substrate.....	91
5.9	Reinforced Carbon-Carbon Penetration Equations.....	92
5.10	Penetration Equations for Ablators.....	95
5.10.1	Phenolic Impregnated Carbon Ablator Penetration Equation.....	95
5.10.2	Avcoat Ablator Penetration Equation.....	96
6	Equations for Predicting Failure Limits of Spacecraft Hardware.....	98
6.1	Honeycomb Panels.....	98
6.2	Toughened MLI.....	98
6.3	Transparent Materials.....	102
6.3.1	Fused Silica Penetration Equations.....	102
6.3.2	Penetration Equations for Polycarbonate.....	103
7	MMOD Damage Detection Sensors.....	105
7.1	Impact Damage Detection using Piezoelectric Film Sensors.....	105
7.1.1	Application of Piezoelectric Blanket Strike Detector to Spacecraft.....	106
7.1.2	Inside a Strike Detector Panel.....	107
7.1.3	Testing and Characterization of the Strike Detector.....	109
7.1.4	Specifications of the Strike Detector.....	110
7.1.5	Example Application.....	112
7.1.6	Operational Scenario.....	113
7.1.7	Number of Detectors.....	114
7.2	Acoustic Sensor Detector.....	115
7.2.1	PINDROP Acoustic Sensor System.....	116
7.2.2	Acoustic Sensor Application Considerations for Metallic Modules.....	117
7.2.3	Acoustic Sensor Application Considerations for Inflatable Modules.....	120
7.3	Fiber Optic Micrometeoroid Impact Sensor.....	121
7.4	Resistive Grid Sensor System.....	123
7.5	Micrometeoroid Impact Detection System.....	125
7.6	Debris Resistive Acoustic Grid Orbital Navy Sensor.....	126
7.7	Secondary Ejecta Detection System and Dual-Layer Optical Curtain Sensor.....	126
8	Concluding Remarks.....	127
9	References.....	128

List of Figures

Figure 1-1.	Whipple shield schematic.	2
Figure 1-2.	Debris cloud observed in high-speed camera film.	3
Figure 1-3.	Mission duration effect on MMOD risk, and effect of number of missions on cumulative MMOD risk (baseline risk = 0.5% or 1 in 200 over 14-day mission).	3
Figure 1-4.	Shielding weight increase as requirements for MMOD protection increase (notional).	4
Figure 1-5.	Effect of shielding type on shield mass needed to meet required MMOD protection levels (notional).	5
Figure 1-6.	Effect of shield standoff on shield mass (notional).	5
Figure 2-1.	Process to evaluate and design MMOD protection.	8
Figure 2-2.	BUMPER Geometry Model of the ISS circa 2006. Each color represents a different shield type. This model excludes solar arrays. Approximately 150,000 elements are in the ISS geometry finite element model (FEM), with an average element size of 20 cm x 20 cm.	9
Figure 2-3.	WLC and NC failure criteria map.	11
Figure 2-4.	Reinforced Carbon-Carbon (RCC) impact damage due to 0.8 mm aluminum projectile at 7.1 km/s (normal impact). On left, damage before arc-jet test. On right, damage after arc-jet test simulating reentry conditions indicating burn-through (test stopped when burn-through detected).	12
Figure 2-5.	White Sands Test Facility .50 caliber two-stage light-gas gun.	13
Figure 2-6.	SwRI's ISCL. Several different size charges are available that are capable of launching 0.25 g to 2 g aluminum projectiles up to 11.5 km/s (left view). Projectiles are typically in the shape of a hollow cylinder (right view).	14
Figure 2-7.	Flux of meteoroids and orbital debris in LEO (in 2006).	16
Figure 2-8.	Space Shuttle MMOD risk of critical damage (LOV) as function of flight orientation (10-day duration, 400 km altitude, 51.6 deg inclination, year 2008). Flight direction to left with Earth direction toward bottom of page.	18
Figure 2-9.	Spacecraft orientation can reduce MMOD risk. Bases of calculation: 1-m-diameter x 1.5-m-long cylinder, year 2010, duration 1 year, 0.13 cm Al 6061T6 bumper, 10 cm standoff, 0.32 cm Al 2219T87 rear wall, debris ORDEM2000, meteoroids SSP30425B, 400 km altitude.	25
Figure 2-10.	MMOD shielding mass as a function of standoff distance. Bases of calculation: constant PNP, Whipple shield with 0.127 cm Al 6061T6 bumper and Al 2219T87 rear wall (rear wall thickness varies to maintain same PNP as standoff is increased), 1-m-diameter x 1.5-m-long cylinder, assumed 30% of bumper mass for standoff substructure mass (shield mass = bumper + rear wall + standoff structure mass).	26
Figure 2-11.	Shielding comparison.	27

Figure 3-1.	MMOD risk contour for the port wing of the Space Shuttle vehicle (underside/belly of vehicle toward bottom of page) – red areas correspond to high risk of MMOD impact damage exceeding failure criteria, blue areas correspond to low risk.....	29
Figure 3-2.	Shuttle-ISS mated flight orientation changed to –XVV (right image) to reduce MMOD risks by factor of 5.....	30
Figure 3-3.	OBSS.....	31
Figure 4-1.	MMOD shield types.....	34
Figure 4-2.	HVI damage modes in aluminum: (a) craters in semi-infinite targets; (b) attached spall; (c) detached spall; and (d) complete penetration or perforation of the target. Impact damage from soda-lime glass projectiles into Al 1100 targets at 5.9 km/s; target thickness to projectile diameter ratio are: (a) $t/d = 10$, (b) $t/d = 4$, (c) $t/d = 3.4$, (d) $t/d = 3$ [26].....	35
Figure 4-3.	Ballistic limits for titanium 15-3-3-3 sheet and bar stock.....	38
Figure 4-4.	Ballistic limits for equal mass monolithic and Whipple shields. Monolithic target is 0.44 cm thick Al 6061-T6. Whipple shield consists of 0.12 cm thick Al 6061T6 bumper followed at 10 cm by 0.32 cm thick Al 6061T6 rear wall.....	45
Figure 4-5.	ISS Node Whipple shields.....	54
Figure 4-6.	Predicted ballistic limits for Whipple shield using Node 2/3 BLEs with 0.16-cm-thick bumper, 12 cm standoff, and 0.48-cm-thick rear wall.....	57
Figure 4-7.	Predicted ballistic limits using Node 2/3 BLEs for a Whipple shield with 0.25 cm bumper thickness, 12 cm standoff, and 0.64 cm rear wall thickness.....	58
Figure 4-8.	Stuffed Whipple shield cross-sectional diagram.....	60
Figure 4-9.	Stuffed Whipple ballistic limits. 0.2 cm Al 6061T6 bumper, 6 Nextel AF62 + 6 Kevlar 710 intermediate bumper, 10.7 cm overall standoff, 0.48 cm Al 2219T87 rear wall.....	65
Figure 4-10.	MS shield configurations.....	67
Figure 4-11.	MS shield ballistic limit curves. MS consists of four Nextel AF26 bumpers (0.043 g/cm ² each), 0.051 cm Al 2024T3 rear wall, 2.54 cm gap between bumpers, 10.2 cm overall spacing.....	72
Figure 4-12.	Hybrid Nextel/aluminum MS shield.....	74
Figure 4-13.	MDB shield.....	77
Figure 5-1.	Hypervelocity damage modes for TPS tiles.....	87
Figure 5-2.	Hypervelocity impact damage modes and kinetic energy thresholds for RCC.....	94
Figure 5-3.	Results from Test HITF-6023. Nominal density PICA. Top view on left, x-ray side view on right. Projectile: 0.32-cm-diameter Al 2017-T4 sphere, 6.59 km/s, 0° impact angle (normal to target). Damage size: 2.0x2.3cm entry hole, 6.1 cm cavity depth, 3.8 cm maximum cavity diameter.....	96

Figure 5-4.	Results from Test HITF-8360 on Avcoat. On left is a top view and on right is an x-ray side view. Projectile: 0.34 cm diameter Al 2017-T4 sphere, 6.98 km/s, 0° impact angle (normal to target). Damage size: 2.8 x 2.9 cm entry hole/surface damage size, 3.3 cm cavity depth.	97
Figure 6-1.	Hyzod and Fused Silica mass per unit area to prevent perforation, as a function of impact velocity for a 0.2-cm-diameter aluminum projectile at 0° impact angle.	104
Figure 7-1.	PVDF film.	106
Figure 7-2.	Panels arranged into a detector array.	107
Figure 7-3.	Picture of film divided into 48 pixels.	108
Figure 7-4.	Cross-section of panel construction.	111
Figure 7-5.	Piezoelectric pixels encapsulated with polyimide layers and conductive ink circuitry applied.	112
Figure 7-6.	Application example showing 16 panels (2 ft wide x 30 ft long) to cover spacecraft shell.	113
Figure 7-7.	Typical sensor signals from 1 milli-Joul impact.	116
Figure 7-8.	Typical signal from impact with aluminum plate (with envelope and exponential fit).	118
Figure 7-9.	Small-scale test structure designed to evaluate signal propagation.	119
Figure 7-10.	Measured signal voltage and Q for hypervelocity 1 mm particle impacts. (Q is the inverse of the loss factor.)	120
Figure 7-11.	Fiber optic displacement sensor (exaggerated size).	121
Figure 7-12.	Test unit containing three sensors (one shown), for HVI studies.	122
Figure 7-13.	RGS.	123
Figure 7-14.	Damage from a 100 um glass hypervelocity impact.	124
Figure 7-15.	MIDS.	125

List of Tables

Table 2-1.	Damage Modes and Failure Criteria for Space Station Elements	10
Table 2-2.	Annual Number of MMOD Impacts on a Cube in 400 km Altitude, 51.6 deg Inclination Orbit, Year 2002, Orbital Density = 2.8 g/cm ³ , Meteoroid Density = 1.0 g/cm ³ . Environment Models: ORDEM2000 [3] and SSP30425B [4].	18
Table 2-3.	Effect of Operational Altitude on Orbital Debris and Micro-Meteoroid Flux of 3 mm and Larger MMOD Particles on a Randomly Tumbling Object, in 51.6 deg Inclination Orbit, Year 2010, Environment Models: ORDEM2000 [3] and SSP30425B [4].	19
Table 2-4.	Yearly change in orbital debris flux of 3 mm and larger particles on a randomly tumbling object in 51.6 deg. inclination orbit, altitude 400 km, ORDEM2000 [3].	20
Table 2-5.	Effect of orbit inclination on orbital debris flux of 3 mm and larger particles on a randomly tumbling object in 400 km altitude orbit, year 2010, ORDEM2000 [3] debris model.	20
Table 2-6.	MMOD Damage Detection and Location Systems Used on the Space Shuttle and ISS	22
Table 2-7.	MMOD Protection Requirements for Various Spacecraft	23
Table 4-1.	Application Comments for Aluminum Single Plate BLE	36
Table 4-2.	Titanium Alloy Physical Properties	38
Table 4-3.	Application Comments for CFRP BLEs	41
Table 4-4.	CALE Hydrocode Results for Projectile Solid/Liquid Fraction in the Debris Cloud as a Function of Velocity (V) and Bumper Thickness to Projectile Diameter Ratio (t/d)	46
Table 4-5.	BLE Coefficients and Shield Parameters for ISS Whipple Shields	53
Table 4-6.	Parameters for Node 2/3 Whipple Shield BLEs.....	56
Table 4-7.	Stuffed Whipple and All-Aluminum Shield Impact Data [10]	63
Table 4-8.	Shield Parameters for Stuffed Whipple and All-Aluminum Impact Tests.....	64
Table 4-9.	Triple-Wall Damage Equation Terms	66
Table 4-10.	Parameter Values for the Triple-Wall BLE.....	66
Table 4-11.	Comparison of Whipple, MS and Mesh Double-Bumper Shield Impact Data.	68
Table 6-1.	Example Aluminum Particle Diameters at Ballistic Limit of two MLI Configurations (baseline and Nextel/Kevlar toughened) at 1.5 cm Standoff from 0.19-cm-thick Aluminum AMG6 Rear Wall.....	101
Table 6-2.	MMOD Penetration Risk over 15 years for Soyuz Protection Options [10]. Penetration is defined as a hole or through-crack in the pressure shell or critical damage to propellant tanks.	101

Acronyms and Abbreviations

AD	Areal Density (mass per unit area)
AETB-8	Alumina Enhanced Thermal Barrier tile (8 lb/ft ³ nominal density)
AFRSI	Advanced Flexible Reusable Surface Insulation
Al	Aluminum
All-Al	All Aluminum
ARC	Ames Research Center
BLE	Ballistic Limit Equation
CFRP	Carbon Fiber Reinforced Plastic
DOCS	Dual-layer Optical Curtain Sensor
DRAGONS	Debris Resistive Acoustic Grid Orbital Navy Sensor
ESA	European Space Agency
ESCG	Engineering Services Contract Group
EVA	Extravehicular Activity
FEM	Finite Element Model
FOD	Fiber Optic Displacement
FOMIS	Fiber Optic Micrometeoroid Impact Sensor
FTA	First to Arrive
HDPE	High Density Polyethylene
HITF	Hypervelocity Impact Technology Facility
HVI	Hypervelocity Impact
HVL	Hypervelocity Launcher
ISCL	Inhibited Shaped Charge Launcher
ISS	International Space Station
JSC	Johnson Space Center
Ksi	1000 psi = 1000 lb _f /in ² = 6.895 MPa
KX	Human Exploration Science Office of the Astromaterials Research and Exploration Science Directorate
LAD-C	Large Area Debris Collector
LEO	Low-Earth Orbit
LI-900 and LI-2200	Lockheed Insulation ceramic tiles, nominally 9 lb/ft ³ and 22 lb/ft ³ density, respectively
LOV	Loss of Vehicle
MDB	Mesh Double-Bumper
MDPS	Meteoroid and Debris Protection System

MIDS	Micrometeoroid Impact Detection System
MLI	Multi-Layer Insulation
MMOD	Micro-Meteoroid Orbital Debris (micro-meteoroids and orbital debris)
MS	Multi-Shock
NASA	National Aeronautics and Space Administration
NC	Nose Cap
NOAX	Non-Oxide Adhesive Experimental Sealant
OBSS	Orbiter Boom Sensor System
ORDEM2000	Orbital Debris Engineering Model 2000
PICA	Phenolic Impregnated Carbon Ablator
PINDROP	Particle Impact Noise Detection and Ranging on Autonomous Platform
PNI	Probability of No Impact
PNP	Probability of No Penetration
PVDF	Polyvinylidene Fluoride
RCC	Reinforced Carbon-Carbon
RGS	Resistive Grid Sensor
SEDS	Secondary Ejecta Detection System
SIP	Strain Isolation Pad
SM	Service Module
SNL	Sandia National Laboratories
SSP	Space Shuttle Program
STS	Space Transportation System
SW	Stuffed Whipple
SwRI	Southwest Research Institute
TPS	Thermal Protection System
TRL	Technology Readiness Level
TUFI	Toughened Unipiece Fibrous Insulation
USL	US Laboratory
WLE	Wing Leading Edge
WLEIDS	Wing Leading Edge Impact Detection Sensor System

Glossary of Terms

Areal density	Mass per unit area
BUMPER or <i>Bumper</i> Code bumper	Software application used for spacecraft MMOD risk assessments
Contour	Outermost shield layer used to break up MMOD particles
Critical Item	A graphical image showing MMOD risk (either impact risk, penetration risk or other failure risk) as color gradient overlay on a FEM
	An item whose failure or loss of function endangers crew or vehicle survivability. For ISS, critical items include modules inhabited by crew as well as external stored energy devices, such as pressurized vessels, propellant tanks, and control moment gyros. For ISS, pressurized lines are not considered MMOD critical items.
Detached spall	A damage mode where solid particles are released from the surface opposite the impact point. Detached spall is caused when reflection of a compressive wave as a tensile wave at the free-surface results in tensile stresses that exceed the tensile strength of the material. Detached spall can occur even when the target is not completely penetrated. Detached spall fragments can have sufficient mass and velocity to cause internal damage to spacecraft components or occupants. Attached spall occurs when there is not sufficient impact energy to cause release of spall fragments. Attached spall will leave a bump on the back of a target and internal hollow cavity within the target.
Flux	Cumulative number of micro-meteoroid and/or orbital debris particles of a given diameter (or mass) and greater per unit area and time. Typical units are number/(m ² – year). The cross-sectional flux, F_c , is in terms of cross-sectional area, whereas surface flux, F_s , is in terms of surface area. For a sphere or randomly tumbling plate, the cross-sectional area is exactly ¼ the surface area. The relationship between F_c and F_s is: $F_c = 4 F_s$.
Node 3	ISS attached pressurized module
Penetration	Can mean either partial penetration (i.e., cratering) or complete penetration of a surface or shield. Additional clarification is provided when used. For ISS, penetration means complete penetration or detached spall from the last layer of shielding. Perforation is a frequently used word to describe complete penetration creating a “through hole” and/or “through crack”.
Probability of No Impact (PNI)	Probability that MMOD of a certain size or greater will not impact an item of interest over a specific time period.
Probability of No Penetration (PNP)	Probability that MMOD will not penetrate a shield, target or item of interest over a specific time period used in the PNP calculation.
Probability of No Catastrophic Failure (PNCF)	Probability that MMOD will not cause loss of crew or loss of spacecraft over a specific time period used in the PNCF calculation. Catastrophic failures usually are a subset of MMOD penetrations (i.e., not all penetrations lead to catastrophic loss).
Rear wall	Last layer of a shield

Shield	All layers providing MMOD protection; i.e., including all bumpers and rear wall
TransHab	An inflatable module concept proposed by NASA for ISS and Mars missions (Transportation Habitat)
Witness plates	Plate(s) added to HVI test article to record damage from penetration of rear wall (witness plates added behind target), or damage from secondary ejecta (witness plates added in front of target)

Contributions

Section	Author	Co-Authors/Contributors
1.0-3.0, 8.0, 9.0	E.L. Christiansen	D. Lear, J. Hyde, T. Prior
4.0, 6.0	E.L. Christiansen	M. Ratliff, S. Ryan, F. Lyons, A. Davis
5.0	E.L. Christiansen	F. Lyons, A. Davis
7.1	T. Byers	E.L. Christiansen
7.2-7.7	J.-C. Liou	F. Giovane, Bob Corsaro, E.L. Christiansen

1 Introduction

Spacecraft are subject to micro-meteoroid and orbital debris (MMOD) impact damage which have the potential to degrade performance, shorten the mission, or result in catastrophic loss of the vehicle. Specific MMOD protection requirements are established by NASA for each spacecraft early in the program/project life to ensure the spacecraft meets desired safety and mission success goals. Both the design and operations influences spacecraft survivability in the MMOD environment, and NASA considers both in meeting MMOD protection requirements.

The purpose of this handbook is to provide spacecraft designers and operations personnel with knowledge gained by NASA in implementing effective MMOD protection for the International Space Station (ISS), Space Shuttle, and various science spacecraft. It has been drawn from a number of previous publications [10-14], as well as new work. This handbook documents design and operational methods to reduce MMOD risk. In addition, this handbook describes tools and equations needed to design proper MMOD protection. It is a living report in that it will be updated and re-released periodically in future with additional information.

Providing effective and efficient MMOD protection is essential for ensuring safe and successful operations of spacecraft and satellites. A variety of shields protect crew modules, external pressurized vessels, and critical equipment from MMOD on the ISS. Certain Space Shuttle Orbiter vehicle systems are hardened from MMOD impact, and operational rules are established to reduce the risk from MMOD (i.e., flight attitudes are selected and late inspection of sensitive thermal protection surfaces are conducted to reduce MMOD impacts). Science spacecraft include specific provisions to meet MMOD protection requirements in their design (e.g., Stardust & GLAST). Commercial satellites such as Iridium and Bigelow Aerospace Genesis spacecraft incorporate MMOD protection. The development of low-weight, effective MMOD protection has enabled these spacecraft missions to be performed successfully. This handbook describes these shielding techniques. For future exploration activities to the moon and Mars, implementing high-performance MMOD shielding will be necessary to meet protection requirements with minimum mass penalty.

A current area of technology development in MMOD shielding is the incorporation of sensors to detect and locate MMOD impact damage. Depending on the type of sensor, the signals from the sensor can be processed to infer the location of the impact and the extent of damage. The objective of the sensors is to locate critical damage (such as an air leak from crew module or critical damage to thermal protection system of reentry vehicles) that would endanger the spacecraft or crew immediately or during reentry. The information from the sensors can then be used with repair kits, patch kits, hatch closure, or other appropriate remedial techniques to reduce MMOD risk.

1.1 MMOD Shielding Background

In the 1940s, Fred Whipple proposed a meteoroid shield for spacecraft consisting of a thin “sacrificial” bumper followed at a distance from a rear wall [9]. The Whipple shield is shown in figure 1-1. The function of the first sheet or “bumper” is to break up the projectile into a cloud of material containing both projectile and bumper debris (figure 1-2). This cloud expands while moving across the standoff, resulting in the impactor momentum being distributed over a wide area of the rear wall. The back sheet (or “rear wall”) must be thick enough to withstand the blast loading from the debris cloud and any solid fragments that remain. For most conditions, a Whipple shield results in a significant weight reduction over a single plate, which must contend with deposition of the projectile kinetic energy in a very localized area.

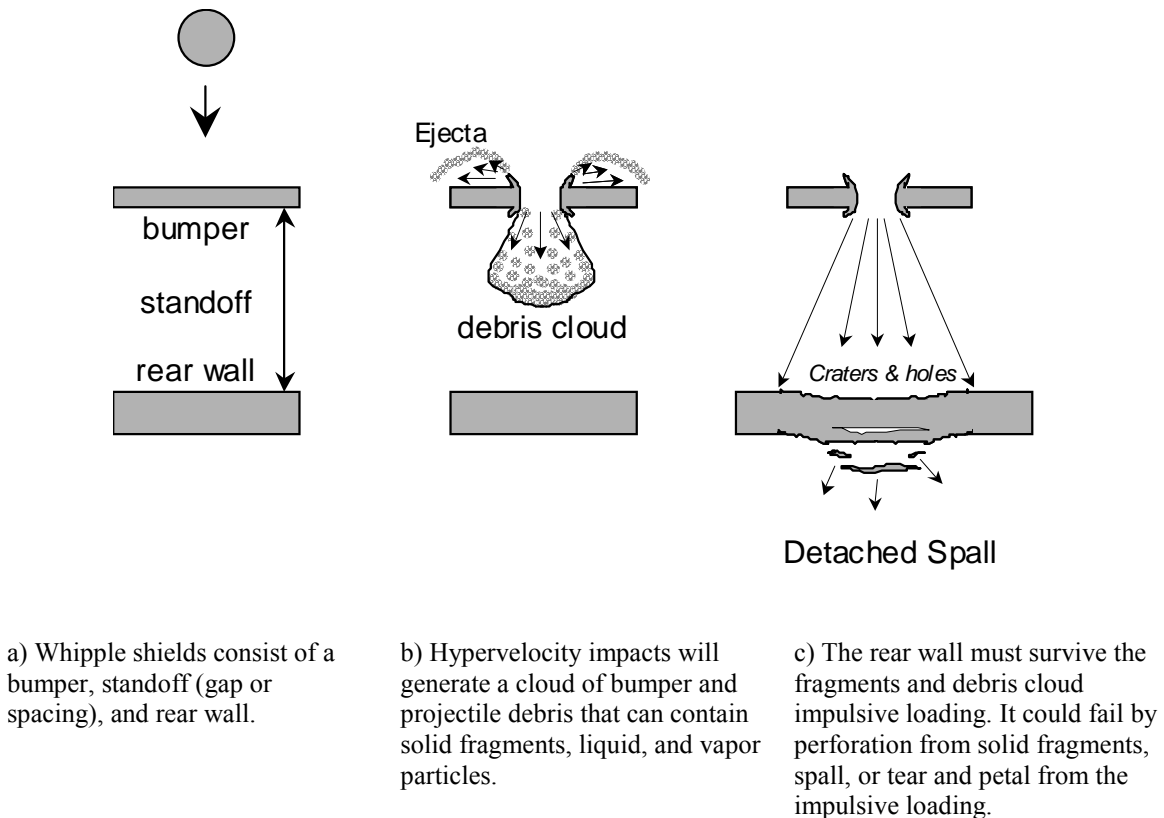
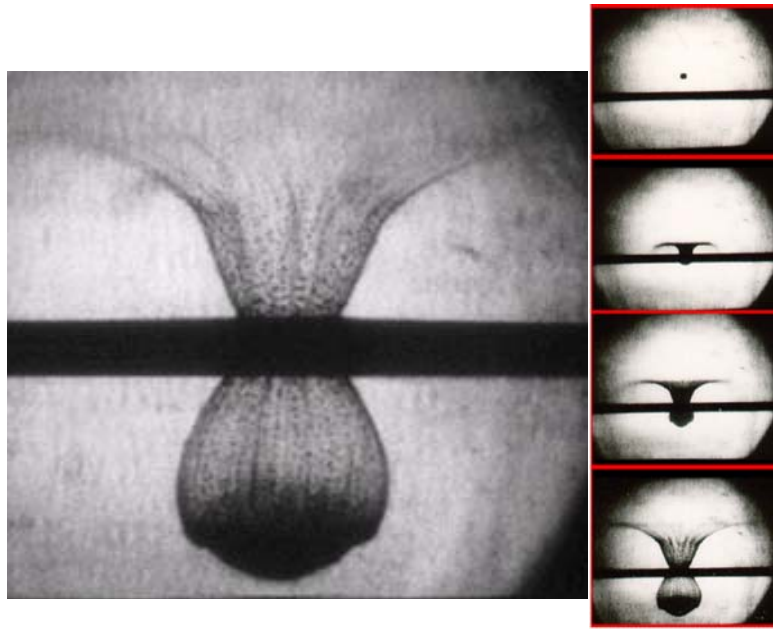


Figure 1-1. Whipple shield schematic.



On left is a close-up of the ejecta and debris cloud. On right, a 0.32-cm-diameter projectile impacts bumper at 6.8 km/s and at an impact angle normal to bumper.

Figure 1-2. Debris cloud observed in high-speed camera film.

1.2 MMOD Trade Space

Designing an effective and efficient protection system for a spacecraft should consider several factors, as follows.

1.2.1 Mission Duration and Spacecraft Size

MMOD risk increases relatively proportionally as mission duration and spacecraft size increase. MMOD risk will roughly double as spacecraft size or duration increases. Figure 1-3 illustrates the effect on MMOD risk for a single mission as mission duration increases, and the cumulative effect on MMOD risk as the number of missions increases.

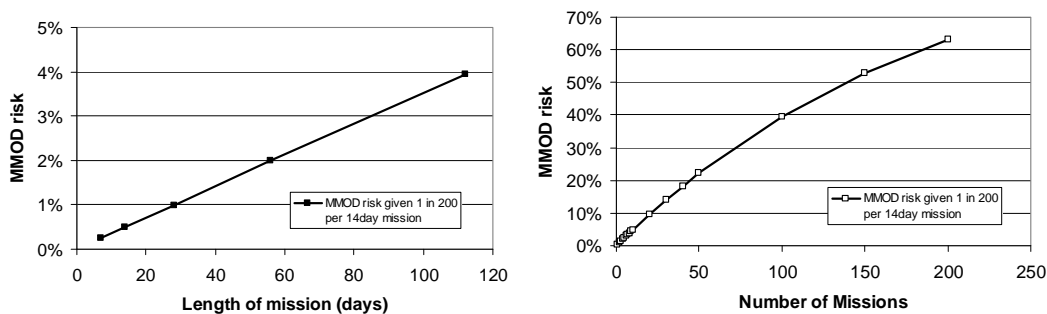


Figure 1-3. Mission duration effect on MMOD risk, and effect of number of missions on cumulative MMOD risk (baseline risk = 0.5% or 1 in 200 over 14-day mission).

1.2.2 Mission Phases and MMOD Environment Models

Orbital debris is a design issue in Earth orbit, but it does not contribute in lunar orbit or lunar surface. Orbital debris consists of high-density (metals, primarily) impacting at hypervelocity (1 km/s to 15 km/s). Orbital debris is dynamic, generally increasing with altitude up to about 2000 km, and is subject to increase due to future growth. Meteoroids are a hypervelocity threat (10 km/s to 70 km/s) present in Earth and lunar orbit, as well as the lunar surface. There is a slight concentration of meteoroids in low-Earth orbit (LEO) from gravitational focusing by Earth, compared to lunar orbit, offset to some extent (depending on orbital altitude) by shadowing from the Earth/moon. MMOD risk is higher in LEO compared to lunar orbit, primarily due to orbital debris encountered in LEO which is not present in lunar orbit. Lunar surface elements are subject to impacts by meteoroids as well as low-velocity secondary impacts from ejecta, impacting primarily from 0.1 km/s to 1 km/s. The most effective type of shield and materials of construction vary depending on where the mission occurs. Longer standoff (greater volume) MMOD shields are very effective against orbital debris and meteoroids in LEO and low-lunar orbit, but not against secondaries on the lunar surface. Low-density, high-strength materials work well as outer shielding layers for meteoroids, but are not effective against orbital debris because their low density does not produce good projectile breakup against higher-density orbital debris. However, high strength to weight materials are universally effective as inner shielding layers.

1.2.3 Required Level of Protection

The requirements for MMOD protection influence the amount of shielding. Generally, requirements for MMOD protection are expressed in terms of either (a) minimum probability of no failure from MMOD impact damage that results in loss of spacecraft function or endangers crew survivability (i.e., a reliability level), or (b) maximum acceptable risk level (i.e., opposite of reliability). As probability of no failure increases, or acceptable risk decreases, spacecraft shielding weight increases, typically exponentially (figure 1-4).

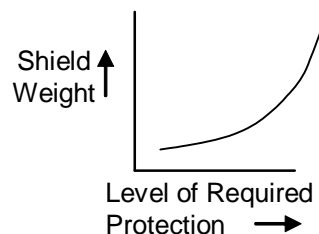


Figure 1-4. Shielding weight increase as requirements for MMOD protection increase (notional).

1.2.4 Type of Shielding

The type of shielding applied to meeting MMOD requirements has a large bearing on the overall mass of the shielding system. Figure 1-5 illustrates how 2-wall Whipple shields using aluminum bumpers compare in shielding mass to 3-wall “stuffed Whipple” shields using ceramic and Kevlar fabrics in the intermediate shield layer. The 3-wall shield system can save 50% or more of the shielding mass. A 4-wall shield system can save even more mass, given sufficient shield “standoff” or volume for the shielding (figure 1-6). Greater shield standoff is usually better, if it is available, in terms of reducing shield mass.

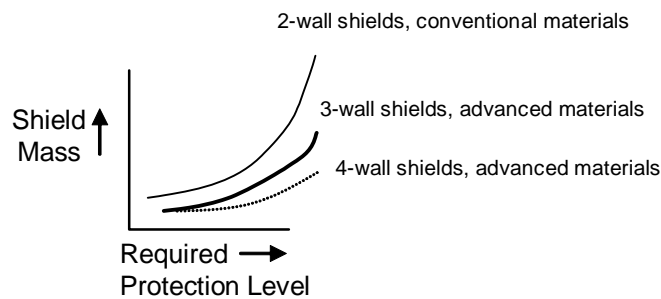


Figure 1-5. Effect of shielding type on shield mass needed to meet required MMOD protection levels (notional).

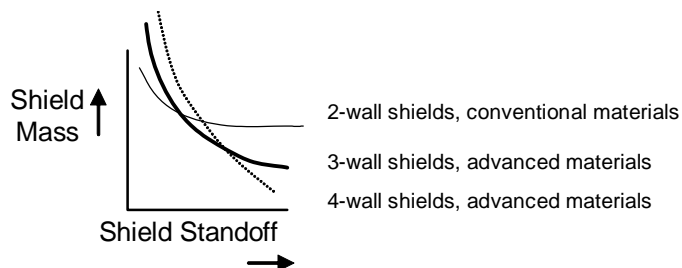


Figure 1-6. Effect of shield standoff on shield mass (notional).

1.2.5 Flight Attitude

Spacecraft orientation or flight attitude can have a major affect on MMOD risks because the MMOD environment is directional (for example, 20 times more impacts occur on forward face than aft face for LEO spacecraft), and because a spacecraft is more vulnerable to MMOD damage in some locations compared to others. For the Space Shuttle, certain flight attitudes are 10 times more risky from MMOD than other attitudes.

1.2.6 Failure Criteria

A clear definition of the maximum allowable damage is required to perform an MMOD risk assessment. Failure occurs if the vehicle sustains MMOD damage just above the maximum allowed. The definition of the failure criteria typically has a big effect on MMOD risks and the best means to mitigate those risks. For reentry vehicles, the failure

criterion of the thermal protection system (TPS) is of concern. TPS failure criteria vary by location on the reentry vehicle and are defined in terms of the maximum amount of MMOD damage that can be tolerated for successful reentry. If allowable damage is limited to the TPS itself, then the best protection approach is to select the most damage-resistant TPS material or thicken the TPS. If damage to the TPS and substrate can be tolerated (failure criterion is defined as critical damage to a critical component behind the substrate), then the best protection approach may be to toughen up the substrate or add interior blankets. For crew modules, on spacecraft not exposed to reentry heating, typical failure criteria are any through-hole or through-crack in the pressure shell which would result in loss of atmosphere. This allows the crew cabin pressure shell to serve as part of the MMOD protection shield (i.e., as the rear wall of the shield). Due to higher level of stress in the walls of pressurized propellant tanks and gaseous/liquid storage tanks, the allowable damage is usually much less than a complete penetration of the pressure shell itself. Many spacecraft systems (power, thermal control, etc.) are designed with redundancy, such that a single MMOD impact failure of one system will not result in loss of the spacecraft. MMOD damage resistance can be relatively easily designed and implemented for exposed redundant spacecraft hardware such as radiator panels, power and data lines, and other systems. Failure of one or more of these systems could represent partial loss of spacecraft functionality, but not loss of the spacecraft unless complete system functionality was lost.

1.2.7 Impact Damage Detection and Location

Impact damage detection and location can improve mission success for both crewed and non-crewed spacecraft. For crewed vehicles, damage detection/location of leaks in pressure shells of crew modules can provide for time to implement repairs or isolation of the damaged module. For reentry vehicles, damage detection/location of critical TPS damage could allow time for repair of the TPS, launch of a replacement vehicle, or change in the reentry trajectory to limit heating to the damaged TPS. For spacecraft that periodically encounter impact hazards (such as spacecraft in orbit about a planet with a dust ring, or spacecraft that have multiple encounters with comets), damage detection sensors integrated into the spacecraft shielding can help operations determine safe encounter distances from the threat; i.e., if shielding was known to be comprised, it may be possible to target future encounters farther away from the threat; or if shield integrity was confirmed good, more risky near approaches could be planned with higher science return.

1.2.8 Risk Reduction and Optimization

The most important step in reducing MMOD risk in the most mass-effective manner is to identify MMOD risk drivers for the spacecraft (i.e., the most vulnerable areas of the spacecraft). A key to reducing shield mass is through optimization of the distribution of shield mass across the spacecraft by equalizing risk per unit area across the spacecraft.

1.3 Organization of the MMOD Protection Handbook

The MMOD protection handbook is organized, as follows. The process used in designing MMOD protection is described in Section 2. A key part of the process is to identify risk drivers for the spacecraft, and focus on these drivers in reducing MMOD risk. Operations options to reduce MMOD risk include selecting flight attitudes that reduce exposure of sensitive spacecraft surfaces to MMOD impact are provided in Sections 2.8, 2.9, and 2.11. Spacecraft design options to meet protection requirements, including robust shielding and redundant systems, are explained in Section 2.11. Section 3 provides some selected examples where the process to reduce MMOD risk was exercised on Space Shuttle and the ISS. Ballistic limit equations (BLEs) used to design and determine the performance of MMOD shielding are discussed in Sections 4, 5, and 6. Impact damage detection and location sensors and described in Section 7. These sensors, combined with a means to mitigate detected damage, provide another system design option to reduce MMOD risk. Section 8 provides concluding remarks.

This handbook will be re-released periodically in the future to reflect additional methods to reduce MMOD risk, provide new/updated BLEs, add information on software tools available to assist users in design of various shielding options, and provide information on MMOD damage identified on ISS, Shuttle, and Hubble Space Telescope.

2 MMOD Protection Design Process

Figure 2-1 illustrates the approach to evaluate and design MMOD protection. In using this methodology, the analyst will accurately evaluate spacecraft risks from MMOD impact, identify zones and areas of the spacecraft that are the “risk drivers” that control the MMOD risk, and evaluate options to reduce risk. The following sections describe each major step in the risk assessment process.

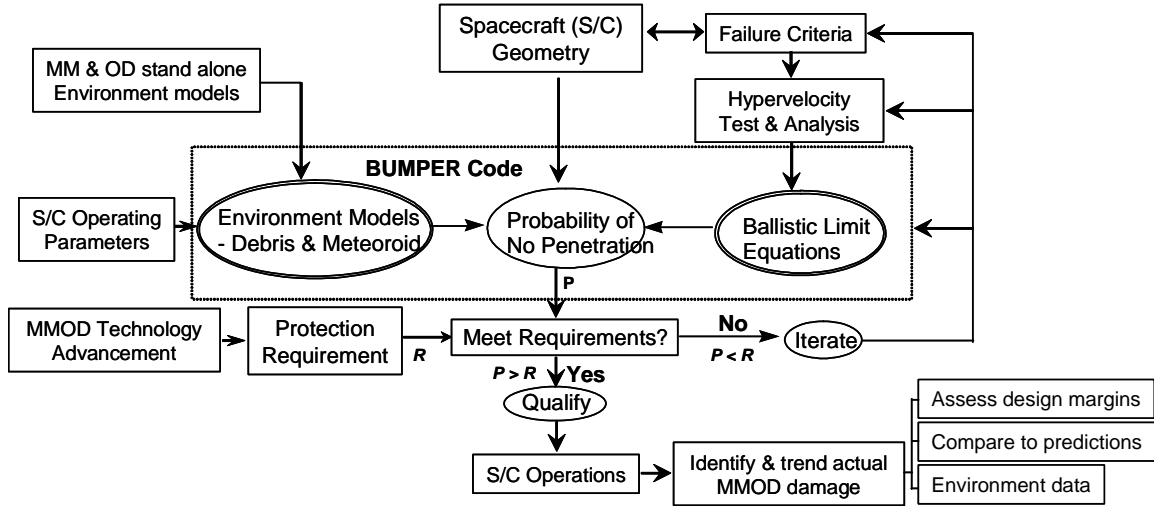


Figure 2-1. Process to evaluate and design MMOD protection.

2.1 Spacecraft Geometry Model

The spacecraft geometry model dictates the size of the spacecraft, and the size of the spacecraft has a direct bearing on MMOD risks. MMOD impact and failure risk increases in direct proportion to increasing area and time exposed to the MMOD flux. This proportionality is illustrated in Equation 2-1 which shows the number of impacts, N , causing failure is equal to the sum of the impact failures in each region (N_i) over all regions ($i = 1$ to n) of the spacecraft. N for each region is found from the product of the cumulative flux, F (number/ m^2 -year), of meteoroid and debris impacts that exceed the failure limits (or ballistic limits), the exposed area, A (m^2), and duration or time exposed to the MMOD flux, t (year).

$$N = \sum_{i=1}^n N_i = \sum_{i=1}^n (FA t)_i \quad (2-1)$$

MMOD risk is related to N , the expected number of impacts causing damage exceeding the failure criteria, through Poisson statistics. Equations 2-2 and 2-3 show the relationship between the probability of no penetration (PNP), MMOD risk, and the number of impacts causing penetration failure from Equation 2-1. Poisson statistics have been used by NASA since Apollo to assess risk from MMOD impact. The same approach is used to assess risks for loss of noncritical hardware (functional failure) from MMOD,

or risks of impact damage exceeding any user-defined damage size (diameter or depth) as long as relevant damage equations exist relating MMOD impactor diameter to damage size.

$$PNP = \exp(-N) \quad (2-2)$$

$$Risk = 1 - PNP \quad (2-3)$$

The spacecraft geometry model physically encompasses the outer mold-line of the spacecraft with different regions defined on the surface of the geometry model, corresponding to regions with different materials of construction, shielding configurations, material thickness, and/or failure criteria. Generally, the geometry model becomes more detailed as the design matures and more emphasis is placed on better identification of risk drivers and on reducing risk. For instance, there are hundreds (over 500) different shield regions defined on the ISS geometry model (figure 2-2), indicating the different shields protecting habitable modules and external critical items (pressure vessels, control moment gyros).

The large number of different shields on the ISS is partly a reflection of the directionality of the MMOD environment. For a spacecraft with fixed orientation relative to the velocity direction, the front (ram surface) and sides of a spacecraft are more exposed to orbital debris impact while the front, sides, and top (zenith) are more exposed to micro-meteoroid impact. More robust shielding, which is more capable from MMOD protection standpoint, is located where MMOD impact rates are highest.

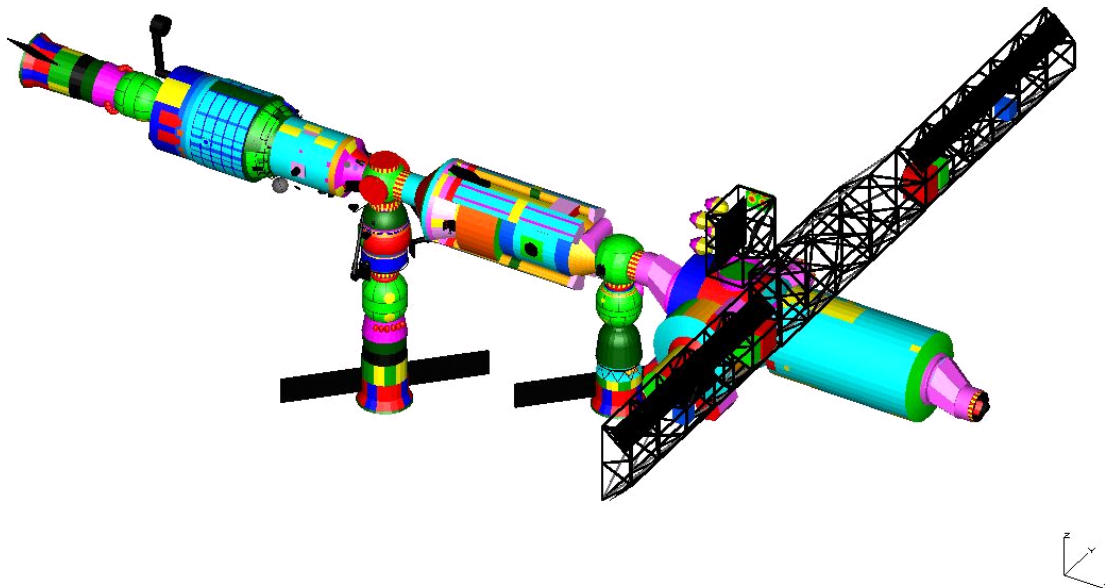


Figure 2-2. BUMPER Geometry Model of the ISS circa 2006. Each color represents a different shield type. This model excludes solar arrays. Approximately 150,000 elements are in the ISS geometry finite element model (FEM), with an average element size of 20 cm x 20 cm.

2.2 Failure Criteria

The criteria that defines the failure threshold from MMOD impact has a significant influence on MMOD risk. A key step, therefore, in the risk assessment process is to precisely define what is meant by “failure”; that is, to quantify the minimum amount of damage that can lead to failure of spacecraft hardware. The “maximum acceptable damage” limit is another way to think of the failure criteria.

A failure criterion or criteria is assigned to each region of the spacecraft geometry model. There can be several failure modes, but the one that results from the smallest MMOD particle controls MMOD risk for the vehicle or element. For instance, MMOD damage modes and failure criteria for elements of the Space Station are given in Table 2-1. Generally, the failure mode in the left most column is created by smaller MMOD particles and is, therefore, more likely to occur than failure modes on the right side of the table. There are two types of Space Station elements: (1) critical; and (2) functional. Critical elements are those whose failure could cause loss of crew or vehicle. Functional elements are those whose loss would degrade the functionality of the vehicle, but they would not result in loss of vehicle (LOV) or crew.

Table 2-1. Damage Modes and Failure Criteria for Space Station Elements

Critical Elements & Components	TPS Damage	Spall or Perforation of Pressure Shell or last layer of shielding	Damage exceeding allowables to Pressure Vessel	Uncontrolled Depressurization	Catastrophic Rupture	Detonation or Deflagration
Crew Modules		X		X	X	
Windows		X*		X	X	
Pressure vessels			X	X	X	
Propellant tanks			X		X	X
Control moment gyros		X			X	
Cargo transfer vehicles		X	X	X	X	X
Crew transfer vehicles	X	X	X	X	X	X
*Window failure criteria is detached spall from redundant pressure pane (which is exterior of primary pressure pane).						

Functional Elements & Components	Surface degradation	Leak	Short or open circuit
Radiator panels	X		
Radiator panel tubes and connection flex/hard lines		X	
Thermal loop lines		X	
Power lines			X
Data lines			X
Batteries		X	X
Solar array	X		X
Window outer pane	X		

Figure 2-3 is indicative of the complexity of the Shuttle Orbiter vehicle failure criteria for MMOD damage that leads to LOV during reentry. This figure shows that the upper regions of the wing leading edge (WLE) and nose cap (NC) of the vehicle are less sensitive to MMOD damage than lower regions. For instance, 1 inch (2.5 cm) diameter through-holes can be tolerated in upper surfaces of the WLE and NC, while much less damage is allowed to lower surfaces. In some areas of the lower surface, non-perforating damage, which only leaves a crater exposing 0.09 inch (0.2 cm) diameter of carbon-carbon substrate, is the defined failure criteria for LOV. A 0.8-mm-diameter aluminum projectile impacting at 7 km/s will create damage in the WLE material that exceeds this lower surface failure criteria (figure 2-4).

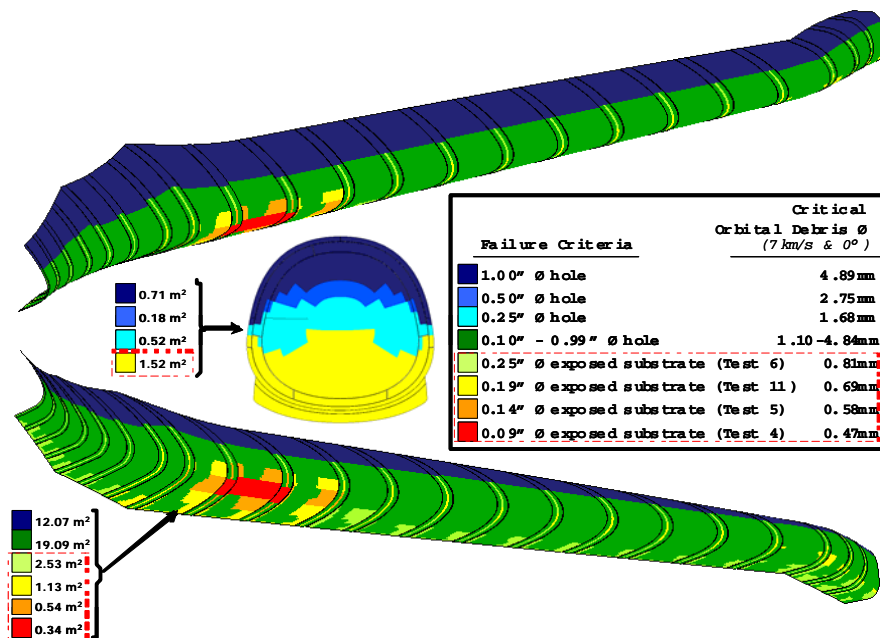


Figure 2-3. WLC and NC failure criteria map.

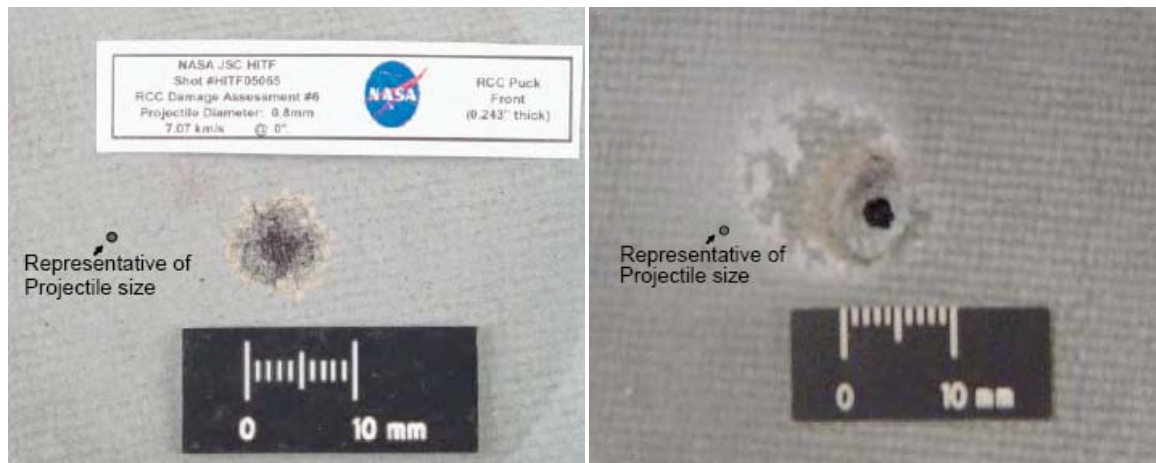


Figure 2-4. Reinforced Carbon-Carbon (RCC) impact damage due to 0.8 mm aluminum projectile at 7.1 km/s (normal impact). On left, damage before arc-jet test. On right, damage after arc-jet test simulating reentry conditions indicating burn-through (test stopped when burn-through detected).

2.3 Ballistic Limit Equations

BLEs define impact conditions (i.e., particle size, particle density, impact velocity, and impact angle) that result in threshold failure of specific spacecraft shields, components, or subsystems. A combination of hypervelocity impact (HVI) test results and analyses are used to determine the BLEs. Many BLEs are semi-empirical, combining data from impact tests as well as the results of analytical models or numerical simulations.

Two types of BLEs are typically defined for a particular spacecraft shield or component:

- (1) Design equations. These are used to determine the dimensions of a shield (e.g., thicknesses/areal densities, spacing, etc.) for a “design” impact condition (projectile diameter, density, impact velocity, and angle).
- (2) Performance equations. These equations relate particle size on threshold failure of a shield or component to impact and target parameters.

Sections 4-6 provide details of several BLEs used for shields and spacecraft components. Specific characteristics of each BLE are described including:

- the relevant spacecraft shield type, subsystem, or component (name, use, configuration, materials, thickness, gaps, etc.)
- the damage mode or failure mode of the shield/component
- the specific BLEs with appropriate nomenclature defined

An Excel program has been developed which enables the user to quickly and simply perform ballistic limit calculations for shield configurations subject to hypervelocity MMOD impacts. This ballistic limit analysis program contains both design and performance modules for each type of spacecraft shield and component. This program will be documented in a later release of the protection handbook.

2.4 Hypervelocity Impact Tests

HVI tests are an integral part of the analyses conducted to ensure adequate design of spacecraft MMOD shielding. Test data are not only used to derive BLEs in the testable velocity range, but also to establish damage modes and material behavior to HVI conditions. Test data are extremely useful to validate numerical simulations.

Two-stage light-gas guns are used to accelerate projectiles up to 7 km/s (figure 2-5). Light-gas guns are capable of launching a variety of different and well-controlled projectile shapes. A disadvantage is that light-gas guns are capable of velocities that cover only a fraction of the orbital debris threat. Since average orbital debris velocity in LEO is on the order of 9 km/s, light-gas guns can directly simulate only 40% of the orbital debris threat.

Other techniques exist to launch projectiles over 10 km/s. For instance, an inhibited shaped charge launcher (ISCL) at Southwest Research Institute (SwRI) is capable of launching aluminum projectiles, 0.25 g to 2 g mass, in the shape of a hollow cylinder to 11.5 km/s (figure 2-6). Another high-speed launcher that has provided useful information on shield capabilities in excess of 10 km/s is the three-stage hypervelocity launcher (HVL) developed at Sandia National Laboratories. This launches thin disks (projectile length to diameter ratio = 0.1 to 0.2, mass 0.2 g to 1 g) of aluminum and titanium from 10-15 km/s with some bowing and tilting of the projectile.



Figure 2-5. White Sands Test Facility .50 caliber two-stage light-gas gun.

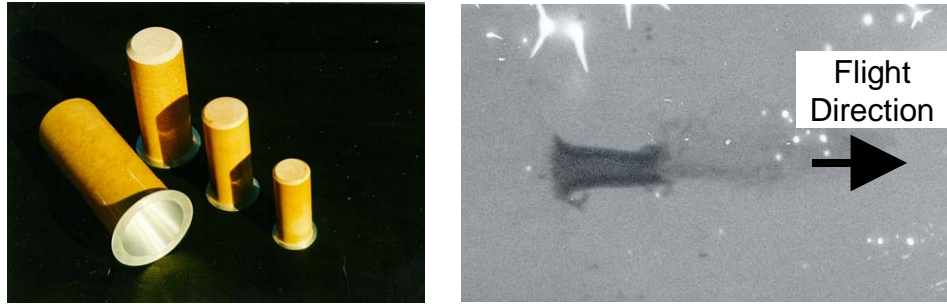


Figure 2-6. SwRI's ISCL. Several different size charges are available that are capable of launching 0.25 g to 2 g aluminum projectiles up to 11.5 km/s (left view). Projectiles are typically in the shape of a hollow cylinder (right view).

2.5 Analysis and Simulation

Analyses and simulations are used along with test data to develop BLEs for use in MMOD risk assessments. The most straightforward method of deriving BLEs is to run a series of HVI experiments and to correlate the damage data collected with target and impact parameters. BLEs must span the impact velocity ranges of on-orbit impacts; i.e., 1 to 16 km/s for orbital debris and 11 to 72 km/s for micro-meteoroids. Since these velocities are beyond the capabilities of laboratory HVLs, BLEs should be obtained from a combination of laboratory experiments, analytical models, and numerical simulations.

Analytical models are possible for simple geometries, initial conditions, and boundary conditions. For instance, one-dimensional approaches can be taken to determine conditions at the projectile/target interface during HVI. Analytical models start with governing physical laws and often employ empirical data to determine necessary material constants.

Numerical simulations of HVI are often referred to as hydrocodes. These simulations solve all the fundamental conservation equations (mass, momentum, and energy) important in impact problems, as well as shock and dynamic material behavior equations across a two- or three-dimensional mesh to trace material displacement with time. The relevant equations solved numerically are highly coupled and nonlinear. Hydrocodes have been around since the 1950s. They got their name because HVI produces local pressures in the target and projectile that greatly exceed the material strength of these materials, the material behaves as if it has no strength; i.e., like a fluid, or hydrodynamic behavior. Away from the impact point, material strength becomes more important. Numerical simulations represent a means to analyze impact phenomena in velocity ranges or projectile shapes/impact orientations not easily obtained in launch facilities, and their reliability and accuracy strongly depend on the knowledge about materials behavior in the hypervelocity regime.

As a consequence, complete understanding of the impact phenomena at reduced velocity becomes essential to extend experimental results and computation philosophy to impacts occurring at higher velocity. Laboratory tests must be used to establish the

Equations of State of the materials involved in hypervelocity collisions, which provide a relationship between pressure, density, and internal energy of the material.

A number of hydrocodes are widely used within the hypervelocity analysis community, including for instance:

- AUTODYN, Century Dynamics Ltd.
- CTH, Sandia National Laboratories
- EPIC, Alliant Techsystems
- EXOS, University of Texas, hybrid particle-finite element formulation
- LS-DYNA, Lawrence Livermore National Laboratory
- MAGI, Air Force Research Laboratory
- PAMSHOCK, Engineering Systems International
- SOPHIA, Ernst-Mach-Institute
- SPHINX, Los Alamos National Laboratory

2.6 MMOD Environment Models

NASA standard meteoroid and debris environment models are used in MMOD risk assessments to determine the cumulative flux of particles with a diameter that exceeds the ballistic limits. The environment models indicate that there are many more smaller particles than larger particles. Thus, raising the shielding performance in terms of the meteoroid/orbital debris particle sizes the shielding can “stop” decreases the flux of penetrating particles and improves spacecraft reliability. Figure 2-7 shows the flux of orbital debris and meteoroids in an ISS orbit (400 km altitude, 51.6 deg inclination).

2.6.1 Micro-Meteoroid Environment Model

Meteoroids are natural particles, in orbit about the sun, which have quite high impact velocities relative to spacecraft in orbit about Earth. Meteoroid velocities range from 11 km/s to 72 km/s, with an average for Earth orbiting spacecraft of 19 km/s. The majority of meteoroids impacting a spacecraft are thought to originate from comets, with relatively low particle densities ranging from 2 g/cm³ (for particles 1 microgram and less) to 0.5 g/cm³ (particle mass 0.01 g and greater). This is contrasted with the meteorites that survive atmospheric entry and are found on Earth’s surface which are higher density and thought to originate mainly from asteroids. The previous meteoroid environment model used for shielding design [1, 4] has recently been updated to the Meteoroid Environment Model [2].

2.6.2 Orbital Debris Environment Model

Orbital debris includes nonfunctional and pieces of spacecraft that are in orbit about Earth. Orbital debris impact velocities are lower than meteoroids, generally impacting spacecraft in LEO at relative speeds of from less than 1 km/s to just over 15 km/s, with an average velocity of about 9 km/s for a 400 km altitude. The debris environment threat is composed of metallic fragments, paint, aluminum-oxide, and other

components of spacecraft and solid rocket motor exhaust. Typically, for debris risk assessments, orbital debris particle density is assumed to be 2.8 g/cm^3 corresponding to aluminum metal. Because the orbital debris environment is tied to human activities in space, it is much more dynamic than the meteoroid environment, and the orbital debris environment definitions are subject to periodic updates and revisions as more data is collected on the amount and evolution of orbital debris in Earth orbit. The current debris environment model for purposes of shielding design is Orbital Debris Engineering Model 2000 (ORDEM2000) described in NASA TP-2002-210780 [2].

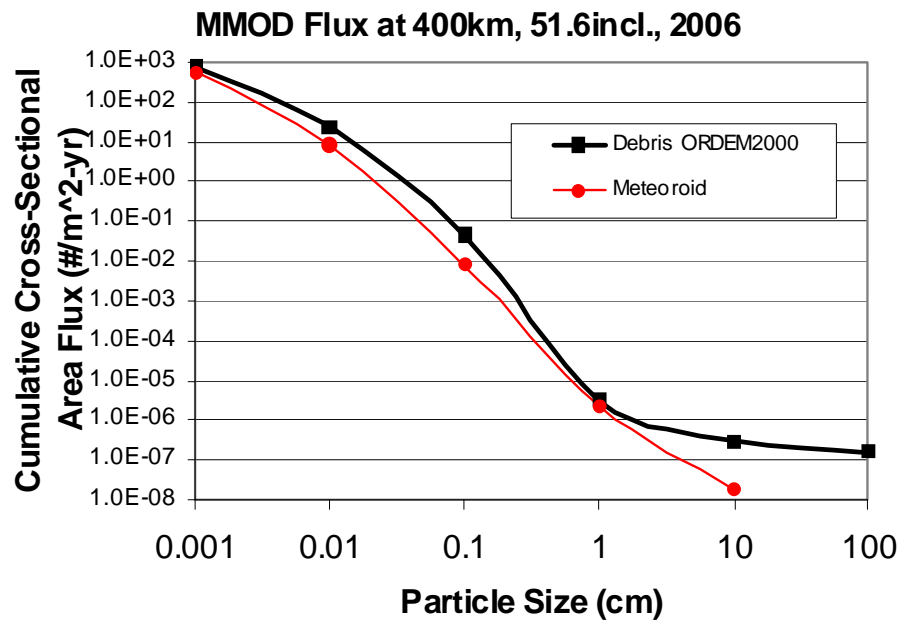


Figure 2-7. Flux of meteoroids and orbital debris in LEO (in 2006).

2.6.3 Lunar Secondary Ejecta Environment Model

Lunar secondary ejecta are particles of the moon that are ejected during meteoroid impacts on the lunar surface and follow ballistic trajectories to rain back on the surrounding surface. Due to high impact velocity, each primary meteoroid impactor can excavate 100 times its own mass in secondary ejecta particles. These fall back to the surface at 10s to 100s of meters per second, and represent a low-velocity impact hazard to the lunar lander, extravehicular activity (EVA) crew, and surface systems. A description of the lunar secondary environment is included in a Constellation Program document: Design Specification for Natural Environments [17].

2.7 MMOD Risk Assessment Tools: *Bumper* Code

The *Bumper* code has been used by NASA and contractors to perform MMOD risk assessments since the early 1990s. Over that period of time, it has undergone extensive revisions and updates. NASA has applied *Bumper* to risk assessments for Space

Station, Shuttle, Mir, Extravehicular Mobility Units (i.e., “spacesuits”), and other satellites and spacecraft. Significant effort has been expended to validate *Bumper* and “benchmark” it to other MMOD risk assessment codes used by some ISS International Partners. Figure 2-1 illustrates where *Bumper* fits in the risk assessment process. The BLEs and MMOD environment models are embedded into the code. An FEM that describes the spacecraft geometry is created in and input into *Bumper*. *Bumper* calculates the number of failures by determining the number of MMOD particles that exceed the ballistic limits for each element of the FEM, and calculates the total number of failures by summing the individual elements. *Bumper* results are used to determine the “risk drivers”; that is, what areas on the spacecraft control the risk. Emphasis is placed on lowering the risk for the drivers to efficiently reduce overall spacecraft MMOD risk.

2.8 Spacecraft Operating Parameters

Spacecraft operating parameters, such as mission duration, spacecraft orientation (attitude), orbital altitude, and damage detection/repair can have a major influence on MMOD risk. The year of the flight and orbital inclination have less of an effect. Additional details on how these factors effect MMOD risk are given in following paragraphs.

2.8.1 Duration

The number of failures from MMOD is directly proportional to mission duration, all other factors held constant (that is, no changes in the MMOD environment, attitude, etc.). If mission duration increases by 2 times, the average number of failures goes up by a factor of 2 for both meteoroids and orbital debris.

2.8.2 Spacecraft Orientation

MMOD impacts are directional. An example illustrating the effect of MMOD impact directionality is the Long Duration Exposure Facility, which had 20 times more craters observed on the forward face compared to the aft, and 200 times more craters on the forward than the Earth-facing side. Both meteoroids and orbital debris are directional. Table 2-2 shows the number of impacts from both meteoroids and orbital debris on each surface of a cube with fixed orientation in LEO. In addition to the larger number of impacts occurring on forward and port/starboard sides of the spacecraft, these impacts occur at higher relative velocity and at less oblique impact angle than for impacts on aft or nadir surfaces of the spacecraft. Greater MMOD risk on the front and sides of the spacecraft is a consequence of the combination of higher impact fluxes, higher relative velocity and less oblique impact angle. The directionality of MMOD makes it advantageous to adjust flight attitude to reduce MMOD risk by pointing the most vulnerable areas of the spacecraft in aft or nadir directions. For instance, the Space Shuttle risk for damage that exceeds LOV failure criteria is shown in figure 2-8. This figure illustrates certain vehicle attitudes (such as belly forward attitudes) result in nearly 10 times more MMOD risk than low-risk attitudes (tail forward and belly to Earth or space).

Table 2-2. Annual Number of MMOD Impacts on a Cube in 400 km Altitude, 51.6 deg Inclination Orbit, Year 2002, Orbital Density = 2.8 g/cm³, Meteoroid Density = 1.0 g/cm³.
Environment Models: ORDEM2000 [3] and SSP30425B [4]

Surface of Cube	Number of MMOD particles ≥ 0.1 mm diameter		Number of MMOD particles ≥ 1.0 cm diameter	
	Orbital Debris	Meteoroids	Orbital Debris	Meteoroids
Forward (front)	5.16	8.31	1.32E-6	5.23E-7
Starboard	7.79	3.64	7.70E-7	2.29E-7
Port	7.90	3.64	7.73E-7	2.29E-7
Aft (back)	0.46	0.92	1.72E-8	5.77E-8
Space (zenith)	0	5.16	0	3.25E-7
Earth (nadir)	0	0.53	0	3.33E-8
Total	21.3	22.2	2.88E-6	1.40E-6

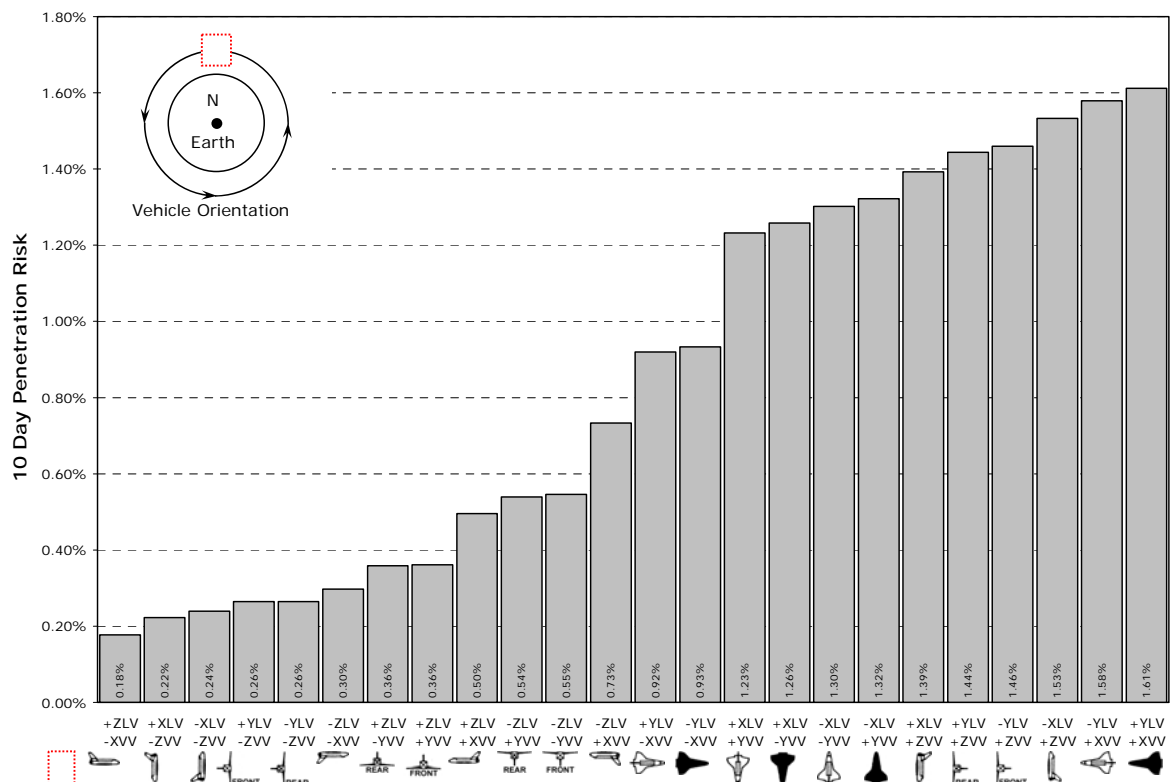


Figure 2-8. Space Shuttle MMOD risk of critical damage (LOV) as function of flight orientation (10-day duration, 400 km altitude, 51.6 deg inclination, year 2008). Flight direction to left with Earth direction toward bottom of page.

2.8.3 Orbital Altitude

As indicated in Table 2-3, the operational altitude of the spacecraft in Earth orbit influences orbital debris flux (and risk from orbital debris impact) to much greater extent than micro-meteoroids. Micro-meteoroid flux does not change much with altitude in LEO.

Table 2-3. Effect of Operational Altitude on Orbital Debris and Micro-Meteoroid Flux of 3 mm and Larger MMOD Particles on a Randomly Tumbling Object, in 51.6 deg Inclination Orbit, Year 2010, Environment Models: ORDEM2000 [3] and SSP30425B [4]

Altitude (km)	Orbital debris flux (#/m ² -year)	Ratio of Orbital debris flux to flux at 400 km altitude	Micro-meteoroid flux (#/m ² -year)	Ratio of micro-meteoroid flux to flux at 400 km altitude
300	3.40E-05	0.34	2.69E-5	0.97
400	9.92E-05	1.00	2.79E-5	1.00
500	2.05E-04	2.07	2.86E-5	1.03
800	6.16E-04	6.22	3.00E-5	1.08
1000	6.97E-04	7.03	3.07E-5	1.10
1500	3.02E-04	3.04	3.16E-5	1.13

2.8.4 Year of Mission

The orbital debris environment varies with time because of the dynamic nature of orbital debris sources and sinks. The current debris environment definition [3] includes a yearly change in the orbital debris environment flux (Table 2-4). Over time, orbital debris is generated from breakups and spacecraft degradation, the quantity of which varies over the years (i.e., debris source term varies with time). The primary sink for orbital debris is atmospheric drag, which eventually causes orbital debris fragments to reenter, thus cleaning the orbital debris environment. Atmospheric drag is related to atmospheric density, which increases with higher solar activity and decreases during lower solar activity. Because of this, orbital debris in LEO will increase and decrease generally in opposite direction to the solar cycle, with a 1- to 2-year delay. That is, orbital debris will tend to increase as solar activity decreases (because less debris is removed by atmospheric drag) and vice versa when solar activity increases. Only the orbital debris flux changes with time on a yearly basis (Table 2-4). The meteoroid environment varies on a daily basis with the presence/absence of various short-term showers, but it is relatively constant from year to year.

Table 2-4. Yearly change in orbital debris flux of 3 mm and larger particles on a randomly tumbling object in 51.6 deg. inclination orbit, altitude 400 km, ORDEM2000 [3].

Year	Orbital debris flux (#/m ² -year)	Ratio of Orbital debris flux to flux in year 2008	Year	Orbital debris flux (#/m ² -year)	Ratio of Orbital debris flux to flux in year 2008
2002	6.25E-05	0.64	2013	9.98E-05	1.03
2003	7.04E-05	0.72	2014	9.19E-05	0.94
2004	7.60E-05	0.78	2015	8.85E-05	0.91
2005	7.28E-05	0.75	2016	9.91E-05	1.02
2006	8.90E-05	0.91	2017	1.24E-04	1.27
2007	9.52E-05	0.98	2018	1.19E-04	1.22
2008	9.74E-05	1.00	2019	1.23E-04	1.26
2009	9.87E-05	1.01	2020	1.22E-04	1.25
2010	9.92E-05	1.02	2021	1.19E-04	1.23
2011	1.14E-04	1.17	2022	1.18E-04	1.21
2012	1.07E-04	1.10	2023	1.22E-04	1.26

2.8.5 Orbit Inclination

The inclination of the spacecraft orbit about Earth has an influence on orbital debris impact flux as shown in Table 2-5. The orbital debris flux is highly coupled to risk from orbital debris. As long as risk is relatively small (<10%), the debris flux is directly proportional to risk from orbital debris.

Table 2-5. Effect of orbit inclination on orbital debris flux of 3 mm and larger particles on a randomly tumbling object in 400 km altitude orbit, year 2010, ORDEM2000 [3] debris model.

Inclination (deg)	Orbital debris flux (#/m ² -year)	Ratio of Orbital debris flux to flux in 51.6 deg. inclination orbit
0	9.13E-05	0.92
10	9.13E-05	0.92
20	9.38E-05	0.95
28.5	9.75E-05	0.98
48	9.76E-05	0.98
51.6	9.92E-05	1.00
66	1.08E-04	1.09
90	1.35E-04	1.36
98	1.49E-04	1.50

2.9 Spacecraft Operational Methods to Reduce MMOD Risk

A number of operational methodologies are used during a mission to reduce MMOD risk including collision warning and avoidance, closing hatches, and damage detection and location.

2.9.1 Collision Warning and Debris Avoidance

One means used to reduce MMOD risk is to simply avoid impact in the first place. The Space Shuttle, ISS, and other high-value space assets are routinely advised of potential collisions with ground-trackable orbital debris. If the predicted collision risk is deemed high enough, a collision avoidance maneuver will be performed. Generally, orbital debris of 5 cm to 10 cm in diameter can be tracked ground-based radar systems. Only relatively large orbital debris, objects are tracked and collision probabilities determined. Smaller orbital debris and meteoroid particles are not tracked because they are either below the detection threshold of the ground-based sensors for smaller debris, or are too fast and not in Earth orbit for meteoroids. The collision risk is calculated many hours in advance of a potential collision based on the orbital elements of the debris object and potential target. More details can be found elsewhere [5, 6].

2.9.2 Hatch Protocol

For crewed spacecraft, failure of protective shielding allows debris to penetrate through the pressure shell and into the crew cabin volume. Penetrations endanger crew survivability from several standpoints. First, if the hole and cracks in the pressure shell exceed the critical crack length, crack growth will not arrest and can lead to module unzip. Second, the pressure loss may be so fast that the crew members are unable to isolate the leak or evacuate successfully. Third, the internal fragments and other effects of a penetration (heat, light, blast/overpressure) can cause crew injury or loss, fail internal pressurized tanks resulting in additional secondary fragment release, or fail internal critical equipment/hardware necessary for vehicle/crew survival (Guidance, Navigation and Control, Environmental Control and Life Support System, etc.). The possibility exists with crewed spacecraft to seal off unoccupied modules using hatches between modules. Then, if penetration occurs to an unoccupied module, there is a far lower chance that crew injury or loss would result. Modules that are not occupied and are not along a main path of crew operations or evacuation are candidates for closing hatches to mitigate MMOD risk. Primarily, such modules provide auxiliary functions such as storage of supplies or waste. Risk reduction by closing hatches is a function of the MMOD risk associated with the module and the fraction of time that the hatches are closed.

2.9.3 Damage Detection and Mitigation

Another means to reduce MMOD risk is to detect and locate MMOD damage that is critical using either sensors or inspection via cameras, and mitigating the damage via operations. For instance, impact damage detection/location systems on spacecraft can be used to:

- (1) Detect and locate critical damage to TPS materials on spacecraft used for reentry of crew and/or cargo. Detection methods include sensors and

inspection using cameras. Mitigation of any detected critical damage can be accomplished by not using the spacecraft until repairs of the damage are performed, or a replacement spacecraft is launched.

- (2) Detect and locate leaks or damage in the pressure shell of crew modules via pressure drop and damage detection sensors. Mitigation can be accomplished by sealing the leak with patches or closing hatches to isolate the leaking module.

Table 2-6 summarizes the MMOD impact detection and location systems used for mitigating MMOD risk on the NASA Space Shuttle and ISS. By virtue of its large internal volume, the crews of ISS have time to locate and isolate leaks if they were to occur by closing hatches. Hole repair kits are manifested and crews trained to repair a leak in a module if it occurs. Crew escape vehicles are docked to ISS in the event of a major event requiring evacuation.

Table 2-6. MMOD Damage Detection and Location Systems Used on the Space Shuttle and ISS

Spacecraft	Damage Detection System
Space Shuttle	Orbiter Boom Sensor System (OBSS)
Space Shuttle	Wing Leading Edge Impact Detection System (WLEIDS)
ISS	Hand-held leak detection system
ISS	Acoustic emission leak detection system

2.10 MMOD Protection Requirements

Vehicles from the early years of space exploration have used the probabilistic approach to develop and implement MMOD protection. MMOD protection requirements are generally expressed in terms of a minimum acceptable reliability level or success criteria; i.e., a probability of NOT being struck by a MMOD particle that will completely penetrate through the spacecraft shielding or cause damage that endangers crew or spacecraft survivability or operability (Table 2-7). Spacecraft MMOD protection is designed to prevent a majority of the MMOD particles that can impact the spacecraft during its lifetime from causing serious damage that would endanger crew survivability and/or continued operation of the spacecraft. Due to spacecraft size and mass constraints, it is not possible with current shielding technology to completely eliminate the risk from MMOD impact. Shielding is an important component of the overall strategy used to reduce the risk from meteoroid/orbital debris impact. The strategy to meet requirements also can include other operational means, such as collision warning and avoidance to reduce the risk from orbital debris impact as well as damage detection and mitigation.

Table 2-7 provides a listing of historical MMOD protection design requirements. Generally, each program defines critical penetrations as those that would endanger the survivability of the vehicle and/or crew, although requirements for mission success and functionality have been defined as well.

Table 2-7. MMOD Protection Requirements for Various Spacecraft

Spacecraft	Environments Considered	Required PNP
Apollo Command and Service Module	Meteoroids	0.995 per 8.3-day mission
Apollo Lunar Lander Module	Meteoroids	0.995 per mission
Skylab Module	Meteoroids	0.995 per 8-month mission
Spacelab Module	Meteoroids	0.999 for 7-day mission
Space Shuttle Orbiter vehicle	Meteoroids and Orbital Debris	0.995 per mission (for damage resulting in LOCV) ¹
Hubble Space Telescope	Meteoroids and Orbital Debris	0.95 for 2 years
International Space Station	Meteoroids and Orbital Debris	0.98 to 0.998 per critical element over 10 years

2.10.1 Requirements Influence on MMOD Protection Capability

The ISS has MMOD protection requirements consistent with past programs, although it carries by far the most capable MMOD shields ever flown. This is because the ISS is larger and exposed longer than other space vehicles. It operates at higher altitudes, in general, than other spacecraft and its operations extend into the future. These factors increase the expected number of MMOD impacts. To meet comparable protection requirements, ISS shielding must be more effective. For instance, most ISS critical hardware exposed to the MMOD flux in the velocity vector (front) or port/starboard (sides) directions will be protected by shields effective at stopping 1 cm to 1.3 cm diameter aluminum debris particle at typical impact velocity and angle (9 km/s, 45 deg impact angle). In comparison, shielding on Mir space station was, in general, able to stop 0.3 cm particles [7], the Space Shuttle Orbiter is capable of stopping 0.1 cm to 0.5 cm particles [8], and Apollo/Skylab were able to stop 0.15 cm to 0.2 cm particles under similar impact conditions.

¹ Original Shuttle design requirements for meteoroid protection alone (not including orbital debris) were 0.95 PNP for 500 missions; however, this requirement was not met.

2.11 Iteration of Analysis Process to Meet MMOD Protection Requirements

The assessed PNP is compared to requirements for MMOD protection to determine if protection design is sufficient. The shielding design effort is successful when the assessed PNP is greater than the required PNP for a spacecraft design and operations that are at final pre-flight level (well past Critical Design Review). As illustrated in figure 2-1, iteration of the risk assessment and risk reduction process is always necessary to update analysis assumptions on the design and operations of the spacecraft, and to meet protection requirements and optimize the design; i.e., meet the requirements with less weight, lower volume (less standoff), less cost, etc. Several techniques are described in this section and applied iteratively to optimize the design and operations to meet MMOD requirements. This process relies on MMOD analysts working closely with project engineering and operations personnel to determine the most practical means to meet MMOD requirements.

2.11.1 Find MMOD Risk Drivers

Perform detailed assessment of penetration risks for the overall vehicle to determine the zones that control the risks (i.e., areas with the highest MMOD risk). Selectively improve the protection capability in the areas identified as risk drivers. Several methods are used to clearly illustrate risk drivers, including bar charts of MMOD risk by region, tables of MMOD risk for each region of the FEM geometry model (include the fraction of total risk and risk/area by region), and color contour plots of MMOD risk on the spacecraft FEM. Constant updates of the color contour plots are especially useful as the design and operations (attitude timeline) change, to keep current on where MMOD risks are concentrated.

2.11.2 Re-Examine Analysis Assumptions for Risk Drivers

After risk drivers are identified, ensure the bases of the risk assessment are justified for regions of the spacecraft that drive MMOD risk. Items to consider include: (a) verify all incidental shadowing from hardware and structures near the risk drivers been incorporated in the analysis; (b) check the reasonableness of the BLEs and predicted particle size at the failure threshold of each risk driver; (c) confirm with engineering that the failure criteria for the risk drivers are justified; and (d) perform HVI tests on the materials representative of risk drivers, compare to predictions from the BLEs, and update BLEs accordingly with the new test data.

2.11.3 Incorporate Directional Shielding

Reduce shielding weight by optimizing shielding weight distribution to account for the directional MMOD distribution. Shielding on each critical item is tailored for the environment and its location on station. Because MMOD impact rate is highest on forward and side surfaces, more capable shielding (heavier or with greater standoff) is applied to these surfaces and less on the Earth-facing surface. Shielding should also be reduced in areas where shadowing from neighboring structure reduce impacts. If shielding is optimized, the ratio of normalized risk/normalized area should be equal for all surfaces of the spacecraft. The goal of this effort, therefore, is to equalize the ratio of

risk to area for the various vehicle zones. The risk/area ratio for each zone is assessed and shielding optimized by repeated *Bumper* code runs.

2.11.4 Reduce MMOD Risk by Maximizing Shadowing

Take advantage of shielding/shadowing from neighboring items. Locate external critical equipment to trailing or Earth-facing surfaces to reduce MMOD impact rates, or put them in areas highly shadowed by other hardware.

2.11.5 Reduce MMOD Risk by Changing Spacecraft Orientation

Pick lowest impact risk spacecraft orientations by minimizing frontal/side areas (gravity gradient orientations are generally high risk for MMOD) and by orienting the most vulnerable surfaces into aft or nadir directions. Figure 2-9 shows that the best orientation to minimize MMOD impact for a relatively short cylinder (1.5 m long, 1 m diameter) is with cylindrical length axis oriented perpendicular to the orbital plane. A vertical (gravity-gradient) orientation (with length axis parallel to Earth radial) has a 30% higher MMOD penetration risk. An orientation with length axis parallel to velocity vector is in the middle. Selecting the best flight attitude by pointing the most vulnerable surfaces aft or toward Earth is standard procedure for the Space Shuttle. Other spacecraft can take a similar approach.

FEM (Color contour: Red = high penetration risk, Blue = low penetration risk)			
Number of MMOD Penetrations	9.31E-5	8.22E-5	1.06E-4
PNP	0.99991	0.99992	0.99989
N Ratio	1.13	1.0	1.29

Figure 2-9. Spacecraft orientation can reduce MMOD risk. Bases of calculation: 1-m-diameter x 1.5-m-long cylinder, year 2010, duration 1 year, 0.13 cm Al 6061T6 bumper, 10 cm standoff, 0.32 cm Al 2219T87 rear wall, debris ORDEM2000, meteoroids SSP30425B, 400 km altitude.

2.11.6 Improve Shielding Performance

Shielding performance can be improved without adding significant mass by increasing the spacing between bumper and shielding rear wall (i.e., improving the capability to stop larger size MMOD particles which will lower MMOD failure risk), or using higher performance alloys and materials for the rear wall. For example, Figure 2-10 illustrates the effect of greater standoff distance on reducing MMOD weight.

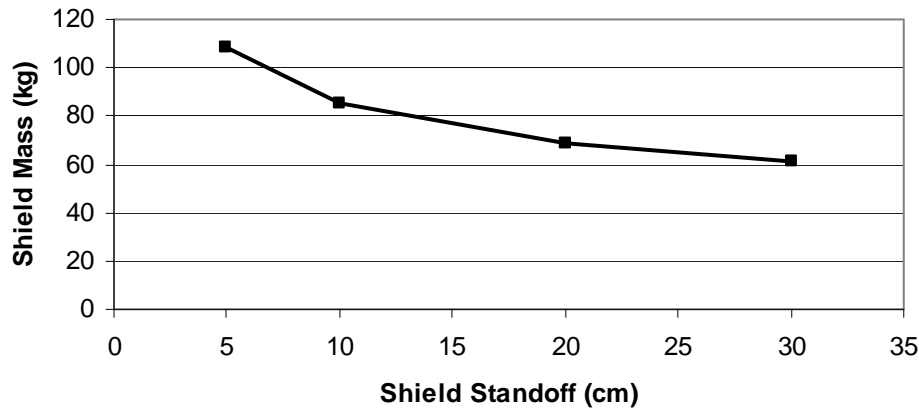


Figure 2-10. MMOD shielding mass as a function of standoff distance. Bases of calculation: constant PNP, Whipple shield with 0.127 cm Al 6061T6 bumper and Al 2219T87 rear wall (rear wall thickness varies to maintain same PNP as standoff is increased), 1-m-diameter x 1.5-m-long cylinder, assumed 30% of bumper mass for standoff substructure mass (shield mass = bumper + rear wall + standoff structure mass).

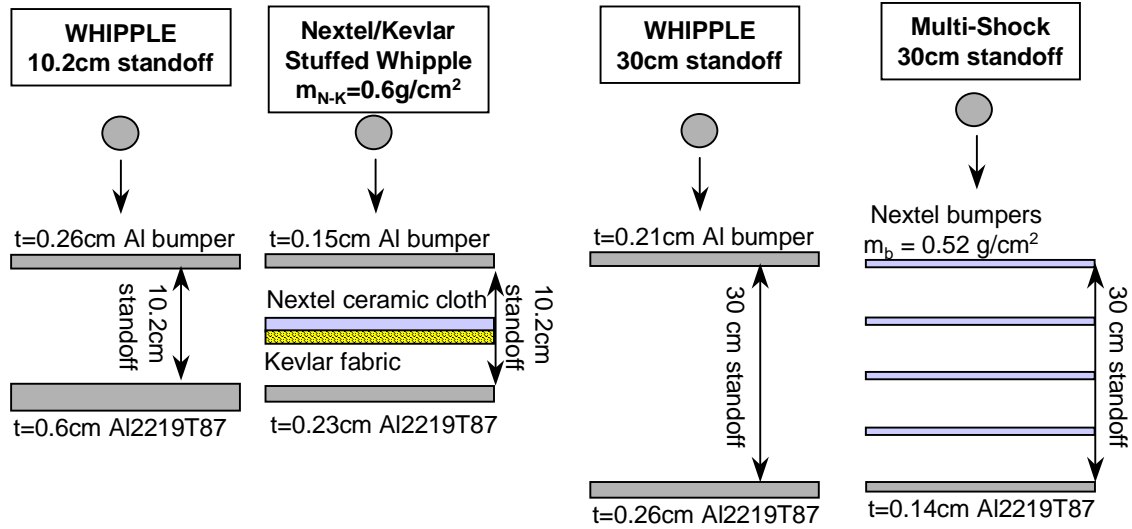
2.11.7 Implement Advanced Shielding

Incorporating more efficient, multi-bumper shielding concepts can provide significant mass savings. Typically, 50% or more mass savings are possible using 3- or 4-wall shields (2 or 3 bumpers and a rear wall) compared to 2 walls (single bumper and rear wall). To illustrate the issue, consider the shielding required to stop a 1-cm-diameter aluminum projectiles at 7 km/s, 0° impact angle (normal to the shield). Four shield concepts to meet the requirement are given in figure 2-11: a conventional aluminum Whipple shield with a 10.2 cm standoff; a Nextel/Kevlar stuffed Whipple shield with the same standoff; a Whipple shield with a 30 cm standoff; and a Nextel multi-shock shield concept. The stuffed Whipple shield incorporates a blanket between the outer aluminum bumper and inner pressure wall that combines two materials: Nextel™ ceramic fabric and Kevlar™ high strength fabric². The shielding mass estimates are made assuming the shielding encloses a cylinder, with 4.2 m inside diameter by 8.5 m long. Stuffed Whipple and Multi-Shock shields are described in more detail in Section 4. But it is clear, for this example, that there are significant mass savings by using advanced shielding concepts (i.e., up to 50% reduction).

Also, it is possible to trade weight for protection capability (i.e., capability and shield PNP are related), so it can be shown that lower weight and more effective protection in terms of higher PNP are possible using Nextel/Kevlar stuffed Whipple and Multi-Shock shields compared to conventional Whipple shields.

² Nextel is a flexible, ceramic fabric product manufactured by 3M Corporation. Nextel contains alumina, boron oxide and silica. Kevlar is a product of the E.I. duPont Co.

Projectile in all cases: 1cm diameter aluminum, 1.5g, 7km/s, normal impact



	Areal Density (kg/m ²)			
	Whipple S=10 cm	Stuffed Whipple S=10 cm	Whipple S=30 cm	Multi-Shock S=30 cm
Bumper:	7.0	10.6	5.6	5.2
Rear wall:	17.2	6.6	7.5	3.8
Total:	24.2	17.3	13.1	9.0
	Surface Area (m ²)			
Bumper:	152	152	175	175
Rear wall:	141	141	141	141
	Mass (kg) including support mass assumed at 30% bumper			
Bumper:	1060	1620	980	910
Support:	320	490	300	270
Rear wall:	2420	940	1060	540
Total:	3800	3050	2340	1720

Figure 2-11. Shielding comparison.

2.11.8 Incorporate Toughened Multi-Layer Insulation Thermal Blanket

Toughening materials, such as ceramic fabric and high-strength fabric, have been included within the multi-layer insulation (MLI) thermal blanket that is commonly used to provide passive thermal control of spacecraft hardware [15, 16]. These additional materials provide improved MMOD shielding. Additional information is provided in Section 6.

2.11.9 Inert Stored Energy Equipment

After use, stored energy equipment should be made inert if possible. For instance, use multiple storage tanks in series instead of parallel, then reduce or fully depressurize storage tanks after emptied. The risk of catastrophic rupture is eliminated when stress levels in the pressure wall are made negligible by depressurizing to a small value. A corollary idea for pressure vessels is to use them in series and deplete first the pressure vessels in the locations that are most exposed to MMOD impact (those in the forward or side positions), followed by less exposed positions. This could require design and operational modifications to implement for propellant tanks and other fluid storage tanks. Another example is to keep spare control moment gyros, flywheels, or other momentum storage devices in an inactive state until required.

2.11.10 Reduce Hazards if Shield Penetration Occurs

Design and operational options are available to reduce hazards if a penetration occurs. For instance, some hatches to unoccupied modules can be kept closed to prevent a depressurization of an entire station if a penetration occurred to the module. A perforation into an unoccupied module with hatch closed would not result in loss of crew from the fragments/shrapnel, light flash, acoustic overpressure, or depressurization. Vent lines between modules could be left open to allow for some air circulation and to keep pressures equalized to facilitate hatch opening during normal operations.

2.11.11 Critical Damage Detection, Repair, and Replacement

Inspection and repair of impact damage to critical areas of reentry vehicles (such as the crew return vehicle attached to ISS) can be used as a supplement to MMOD shielding for maintaining flight worthiness. Some impact damage to TPS on Earth return vehicles is not a hazard while on orbit (and may, therefore, be undetected) but could become hazardous later during reentry aerodynamic heating phases. Properly placed instrumentation with correct sensitivity to detect critical TPS damage can help support the inspection/detection process.

2.12 MMOD Risk Reduction Opportunities During Spacecraft Operations

The effort to evaluate and reduce MMOD risk continues during operational phases of the spacecraft in following areas:

- Evaluate effect on MMOD risk from changes to vehicle design or operations.
- Assess methods to reduce MMOD risk.
- Inspect returned hardware and on-orbit photographs for MMOD damage.
- Trend MMOD impact data, provide data to MMOD environment groups, and evaluate changes in the MMOD environment.
- Provide Flight Projects with data on “near-misses,” which are MMOD damages that could be considered critical/catastrophic if impact occurred on other parts of the vehicle.

3 Applications

This section discusses selected application examples of the MMOD protection improvement process described in Section 2 for Space Shuttle, ISS, and Exploration vehicles.

3.1 Changing Shuttle Orientation while Docked to ISS

MMOD impact risks to the Space Shuttle Orbiter vehicle are primarily to the WLE and NC, which are relatively thin and vulnerable to MMOD impact damage. A MMOD risk contour plot illustrates the high impact risk especially to underside regions of the WLE and NC (figure 3-1). To reduce MMOD risks to the Shuttle, the orientation of the vehicle was changed during a majority the ISS docked phase of the Shuttle mission. The change in orientation – essentially flying the ISS “backward” – provided incidental shielding to the Shuttle as well as directing MMOD-sensitive areas away from the ambient MMOD particle flux. The change orients the bottom of the Shuttle in the wake direction of the ISS, which reduces MMOD impacts to the most vulnerable surfaces of the vehicle, improving crew safety and mission success. In all ISS missions prior to Space Transportation System (STS)-114, the belly of the vehicle faced into the ram “velocity” direction of ISS motion and highest MMOD impact flux. Figure 3-2 shows the Shuttle-ISS docked orientation change with respect to the ISS velocity direction.

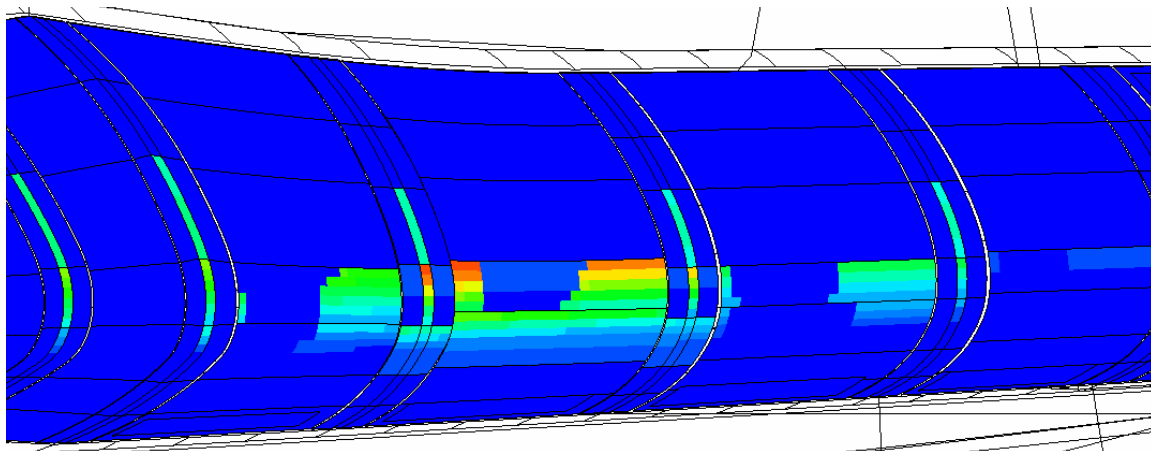


Figure 3-1. MMOD risk contour for the port wing of the Space Shuttle vehicle (underside/belly of vehicle toward bottom of page) – red areas correspond to high risk of MMOD impact damage exceeding failure criteria, blue areas correspond to low risk.

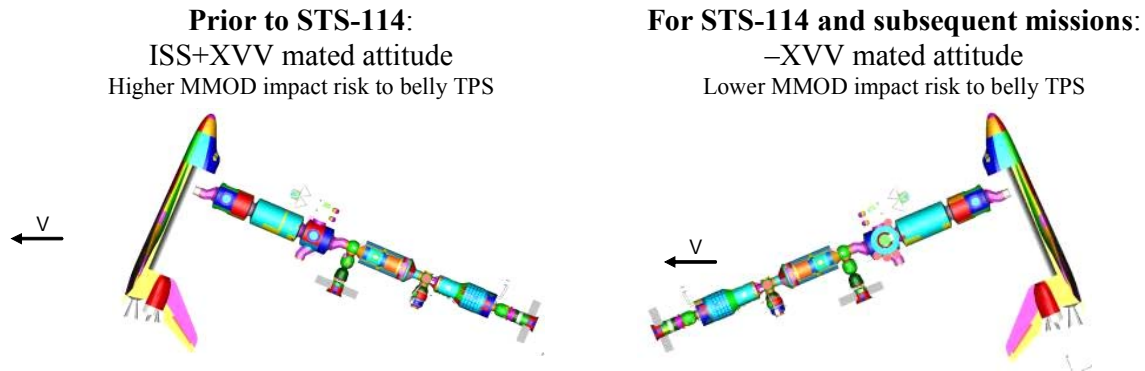


Figure 3-2. Shuttle-ISS mated flight orientation changed to –XVV (right image) to reduce MMOD risks by factor of 5.

3.2 Late Inspection of Space Shuttle WLE and NC for MMOD Damage

The WLE and NC of the Space Shuttle vehicle represent the majority of the MMOD risk to the vehicle, even given the change in flight orientation described in Section 3.1. To further reduce MMOD risks for LOV and crew, a late inspection is performed of these high-risk areas to confirm that no damage exceeds the limits of allowable damage for safe return (i.e., the WLE and NC failure criteria). The inspection is usually performed just after undock from the ISS, using the OBSS. This system has been in use since STS-114 (July 2005). An early inspection is performed of the WLE, NC, and other parts of the vehicle to detect any potential critical damage to the TPS of the vehicle caused by launch debris. The purpose of the late inspection is to detect any critical damage received from MMOD impacts. The OBSS is a 15-m-long boom terminating in an instrumentation package that can be grappled by the Remote Manipulator System of the Space Shuttle spacecraft. The OBSS has two instrumentation packages (figure 3-3). Sensor package 1 consists of a Laser Dynamic Range Imager and an Intensified Television Camera. Sensor package 2 contains a Laser Camera System and a digital camera. The sensors can resolve damage at a resolution of a few millimeters, and can scan at a rate of about 6 cm per second. If flight engineers find potential damage to the areas scanned, more detailed or focused scans can be performed. If critical damage is detected with the OBSS, the crew may attempt a repair via an EVA. If the damage is not repairable, the crew will dock with the ISS and await a rescue mission (see further details in Section 3.3). Late inspection of the WLE and NC, with mitigation if critical damage is found, reduces risks for LOCV by factor of 2.

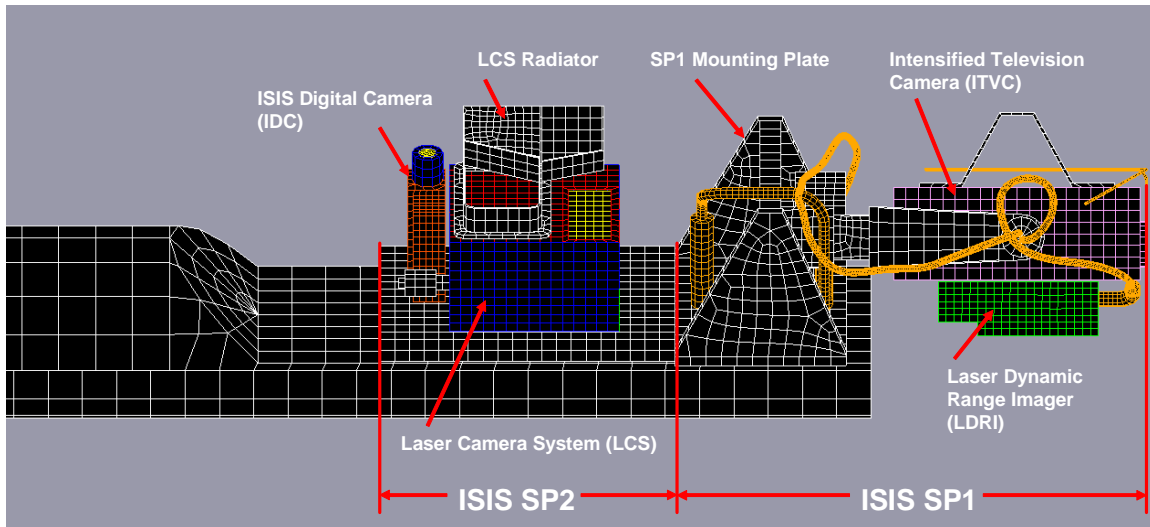


Figure 3-3. OBSS.

3.3 Shuttle Impact Sensors and On-Orbit Repair

The Space Shuttle Orbiter vehicle was equipped after the loss of *Columbia* with a WLE impact detection system (WLEIDS). The WLEIDS consists of 132 single-axis accelerometers mounted along the length of the Orbiter's leading edge wing spars. During launch, the accelerometers collect data at a rate of 20 kHz and store the data for subsequent downlink to Mission Control. Within 6 to 8 hours of launch, summary files containing the data collected by each accelerometer are downlinked for analysis to find potential signatures of ascent damage. This analysis is completed within 24 to 48 hours of launch so that the results can be used to schedule focused inspection using the OBSS sensors. The WLEIDS is also used to detect MMOD impacts to the WLE, but its use is limited to periods of time that are considered high MMOD risk during the mission, due to limited battery life of the WLEIDS accelerometers. The MMOD impact data are used to guide late mission inspection decisions.

The WLE and NC of the Shuttle vehicle consist of RCC panels and T-seals. The Shuttle Program has manifested two kits for on-orbit RCC repair. The repair must prevent plasma flow through the damaged RCC. One kit is designed to repair small cracks and coating losses on the exterior of the RCC panel. The crack repair technique uses a sealant material known as NOAX – or non-oxide adhesive experimental sealant – containing a pre-ceramic polymer impregnated with carbon and silicon carbide powder. It is applied by an astronaut using a space-adapted caulking gun applicator and putty knife. The second kit is designed for repair of 13- to 100-mm-diameter holes in RCC panels. This kit is referred to as a plug repair and consists of a carbon-silicon carbide patch coated with sealant. It is mechanically attached to the RCC panel with a T-bar attachment similar to a toggle bolt. If the damage site is less than 13 mm, the astronauts will use a special bit to drill out the hole.

If a repair is not feasible, the crew of a critically damaged Shuttle will invoke Contingency Shuttle Crew Support, also known as safe haven. The Contingency Shuttle Crew Support scenario calls for the crew of the damaged vehicle to remain on board the ISS until a rescue mission can be staged. The viability of this option is tied to resources on the ISS and the time required to prepare a rescue vehicle for launch.

4 Equations for Designing MMOD Shields

This section provides BLEs characterizing the performance of MMOD shields including monolithic single-wall and multi-wall shields.

Monolithic shield equations are provided for aluminum, titanium, stainless steel, carbon fiber reinforced plastic (CFRP) composites, fused-silica glass, and polycarbonate (Hyzod³). Also, the ballistic performance of MLI thermal blanket covered aluminum and CFRP is also provided. The equations include penetration and damage equations that predict damage depth and size as a function of impact conditions and target parameters, as well as performance equations that relate MMOD particle size that is on the failure threshold of the shield as a function of impact and target parameters.

Multi-wall shields include Whipple (dual-wall), Nextel/Kevlar stuffed Whipple (triple-wall), and multi-shock (multiple-wall) shields given in figure 4-1. Whipple shields have an outer “bumper” and inner “rear wall” with a “standoff” or gap between the two. Stuffed Whipple (SW) shields have a blanket of Nextel ceramic cloth and Kevlar ballistic protection fabric between the bumper and rear wall. Multi-shock (MS) shields have multiple bumpers (three to four, typically) followed by a rear wall. BLEs provided for these shields are of two general types:

1. Design equations used to size the shielding elements for a particular threat particle size and impact conditions.
2. Performance equations used to define the particle size on the ballistic limit of a particular shield as a function of impact conditions (impact velocity, particle density, impact angle, and particle shape).

Design equations are particularly useful when initially determining shield parameters to meet a particular design requirement. More detailed analyses using the performance equations and *Bumper* code are conducted to iterate the design and verify requirements have been met. HVI tests to confirm and update the BLEs for particular shield configurations on the spacecraft should be performed during shielding development.

³ Hyzod™ is a high-strength polycarbonate product from Sheffield Plastics, Inc.

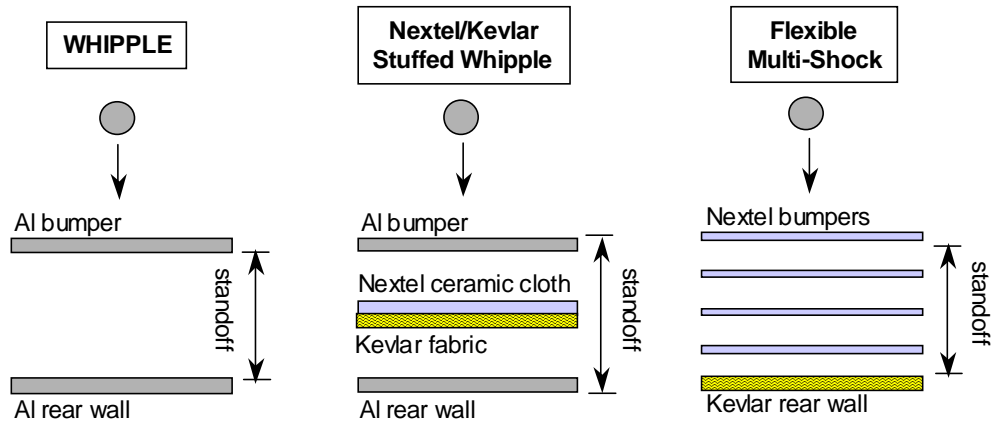


Figure 4-1. MMOD shield types.

4.1 Single-Wall Shielding

The following sections provide BLEs for single-wall shields made from monolithic plates of aluminum alloy, titanium, stainless steel, carbon composite, and fiberglass composite. The effect on protection performance from adding MLI thermal blankets to the exterior of the shielding is also described.

4.1.1 Aluminum Monolithic Shields

The Cour-Palais single-wall penetration equation [18, 19] considers HVI into a semi-infinite plate, which leaves a crater. Semi-infinite targets are thick enough that there is no noticeable change on the back surface of the target behind the impact crater (i.e., the back surface remains flat and free of cracks after the impact). Penetration depth into a semi-infinite target, P_∞ , depends on projectile-to-target density ratio, ρ_p/ρ_t , as follows:

For $\rho_p/\rho_t < 1.5$,

$$P_\infty = 5.24 d^{(19/18)} BHN^{-0.25} \left(\frac{\rho_p}{\rho_t} \right)^{0.5} \left(\frac{V \cos \theta}{C} \right)^{2/3} \quad (4-1)$$

For $\rho_p/\rho_t \geq 1.5$,

$$P_\infty = 5.24 d^{(19/18)} BHN^{-0.25} \left(\frac{\rho_p}{\rho_t} \right)^{2/3} \left(\frac{V \cos \theta}{C_t} \right)^{2/3} \quad (4-2)$$

Where

BHN = Brinell hardness of the target

C_t = speed of sound in the target (km/s)

d = projectile diameter (cm)

P_{∞} = penetration depth in semi-infinite target (cm)

ρ_p = projectile density (g/cm^3)

ρ_t = target density (g/cm^3)

θ = impact angle from target normal (deg); $\theta = 0^\circ$ impact normal to target

V = projectile velocity (km/s)

For aluminum-on-aluminum impacts at speeds in excess of 5 km/s, the crater is nearly hemispherical. As the thickness of the plate is decreased, the plate undergoes internal fracturing near the rear surface (incipient spall) and development of attached spall, detachment of spalled material from the rear surface, and finally perforation when the entry crater and spallation area overlap. Figure 4-2 illustrates the cratering process. Note that as target thickness decreases, the crater elongates as spall develops on the rear side of the target; i.e., penetration depth increases as the target becomes thinner, even though there is no change in impact conditions.

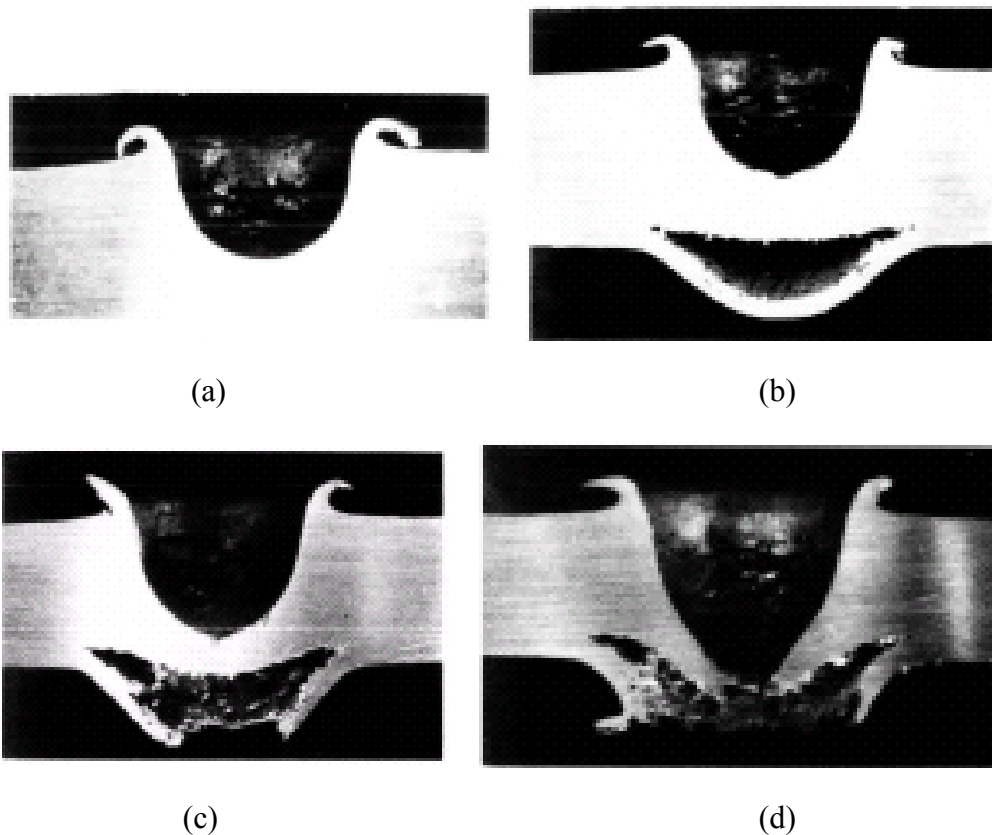


Figure 4-2. HVI damage modes in aluminum: (a) craters in semi-infinite targets; (b) attached spall; (c) detached spall; and (d) complete penetration or perforation of the target. Impact damage from soda-lime glass projectiles into Al 1100 targets at 5.9 km/s; target thickness to projectile diameter ratio are: (a) $t/d = 10$, (b) $t/d = 4$, (c) $t/d = 3.4$, (d) $t/d = 3$ [26].

Equation 4-3 gives the required shielding thickness to prevent attached (incipient) spall on the back of the aluminum plate. Equations 4-4 and 4-5 provide the shielding thickness to prevent detached spall and complete perforation of the aluminum plate, respectively.

$$\text{To prevent incipient spall:} \quad t \geq 3 P_{\infty} \quad (4-3)$$

$$\text{To prevent detached spall:} \quad t \geq 2.2 P_{\infty} \quad (4-4)$$

$$\text{To prevent perforation:} \quad t \geq 1.8 P_{\infty} \quad (4-5)$$

For a specific shielding configuration, the particle size on the threshold of either perforation, detached spall, or incipient spall is determined using:

$$d_c = \left[\frac{t \text{ BHN}^{0.25} (\rho_t / \rho_p)^{0.5}}{k 5.24 (V \cos \theta / C_t)^{2/3}} \right]^{18/19} \quad (4-6)$$

Where

BHN = Brinell hardness of the target

C_t = speed of sound in the target (km/s)

d_c = critical projectile diameter on threshold of given damage mode (cm)

k = damage parameter, either 1.8, 2.2, or 3.0 for perforation, detached spall or incipient attached spall, respectively

ρ_p = projectile density (g/cm^3)

ρ_t = target density (g/cm^3)

t = target thickness (cm)

θ = impact angle from target normal (deg); $\theta = 0^\circ$ impact normal to target

V = projectile velocity (km/s)

Table 4-1 provides an overview of the range in impact conditions that the aluminum BLEs have been validated by HVI test.

Table 4-1. Application Comments for Aluminum Single Plate BLE

Validated for		Applied to	Comments
Materials	Aluminum	Aluminum alloys	
Impact angles	0° to $>85^\circ$	Normal, oblique	Equation appears to slightly over-predict penetration depth for impact angles over 45° [20]
Impact velocities	< 8 km/s	All	

4.1.2 Titanium Monolithic Shield

Equations for predicting penetration into a single-layer titanium alloy shield have been developed [22]. The following equation relates penetration depth into a semi-infinite thickness of titanium with projectile and target parameters:

$$P_{\infty Ti} = 5.24 d BHN^{-0.25} \left(\frac{\rho_p}{\rho_t} \right)^{0.5} \left(\frac{V \cos \theta}{C_t} \right)^{2/3} \quad (4-7)$$

This equation is used to calculate the minimum diameter of a spherical particle that produces a given amount of damage to the impacted titanium wall as follows:

$$d = t_{Ti} K 5.24^{-1} BHN^{0.25} \left(\frac{\rho_p}{\rho_t} \right)^{-0.5} \left(\frac{V \cos \theta}{C_t} \right)^{-2/3} \quad (4-8)$$

The minimum thickness of a titanium wall to prevent a given amount of damage is:

$$t_{Ti} = 5.24 K^{-1} BHN^{-0.25} (\rho_t)^{-0.5} (C_t)^{-2/3} \left[\frac{12}{\pi} (\rho_p)^{0.5} E \right]^{1/3} \quad (4-9)$$

Where

BHN = Brinell hardness of the target

C_t = speed of sound in the target (km/s)

d = projectile diameter (cm)

E = projectile normal component kinetic energy (J) = $\pi/12 d^3 \rho_p (V \cos \theta)^2$

K = damage parameter for titanium alloy, either 1.8, 2.4 or 3.0 for perforation, detached spall, or incipient attached spall, respectively

$P_{\infty Ti}$ = penetration depth in semi-infinite titanium target (cm)

ρ_p = projectile density (g/cm³)

ρ_t = target density (g/cm³)

t_{Ti} = titanium thickness (cm)

θ = impact angle from target normal (deg); $\theta = 0^\circ$ impact normal to target

V = projectile velocity (km/s)

Typical physical properties of titanium alloys are given in the following table. The following figure plots impact data on titanium Ti-15-3-3-3 alloy compared to the predictions using the above BLEs. Pass/fail criterion for these tests was based on presence of detached spall (pass if no detached spall present).

Table 4-2. Titanium Alloy Physical Properties

Material	Form	Density (g/cm ³)	Brinell Hardness	Speed of Sound (km/s)
Ti-15V-3Cr-3Al-3Sn	Sheet	4.73	257	4.26
Ti-15V-3Cr-3Al-3Sn	Bar	4.65	390	4.62

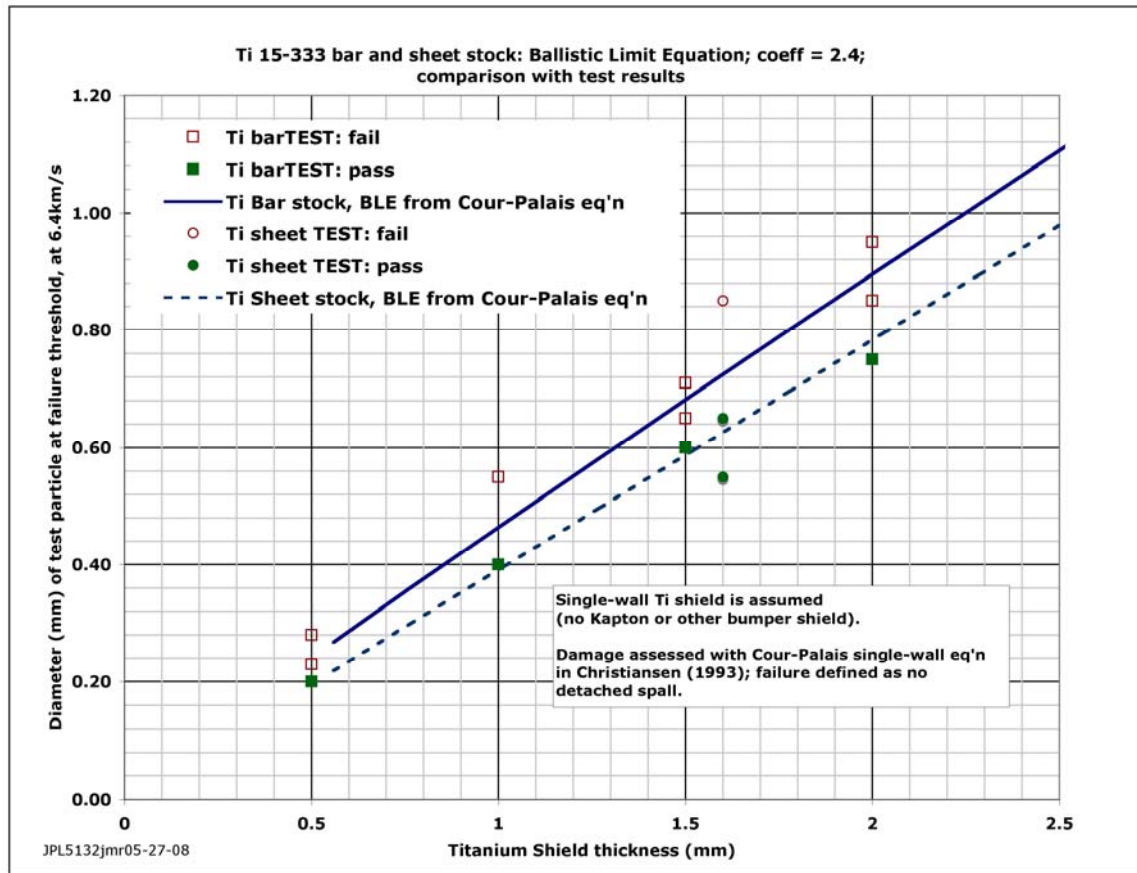


Figure 4-3. Ballistic limits for titanium 15-3-3-3 sheet and bar stock.

4.1.3 Stainless Steel Monolithic Shield

The following set of penetration equations were developed based on cratering experiments into CRES 15-5PH stainless steel [24, 25].

$$P_{Steel} = 0.434 d^{(19/18)} \left(\frac{\rho_p}{\rho_t} \right)^{0.5} (V \cos \theta)^{2/3} \quad (4-10)$$

To prevent perforation of the stainless steel, it is assumed the thickness of the steel is given by the following equation. Additional impact data is necessary to determine the coefficient used in this equation.

$$t_{Steel} \geq 1.8 P_{Steel} \quad (4-11)$$

The diameter of the impacting particle that is at the perforation limit of a stainless steel plate of thickness, t_{Steel} , is:

$$d = 1.57 (t_{Steel})^{(18/19)} \left(\frac{\rho_p}{\rho_t} \right)^{-0.474} (V \cos \theta)^{-0.632} \quad (4-12)$$

Where

d = projectile diameter (cm)

P_{Steel} = penetration depth in semi-infinite steel target (cm)

ρ_p = projectile density (g/cm^3)

ρ_t = target density (g/cm^3)

t_{Steel} = thickness of steel target (cm)

θ = impact angle from target normal (deg); $\theta = 0^\circ$ impact normal to target

V = projectile velocity (km/s)

4.1.4 Carbon-Fiber Reinforced Plastic Single-Wall Shields

Crater formation and shock transmission in a non-isotropic material such as CFRP is considerably different to that seen in metals. For semi-infinite CFRP, a modification of the aluminum (Al) cratering equation is given in equations 4-13 through 4-15, which includes an empirically derived single material parameter (K_{CFRP}) to describe the effect of material properties [21]. Additionally, a term is included to account for the effect of MLI on top of the CFRP plate.

Expected penetration depth into a semi-infinite CFRP plate as a function of impact parameters is given by the following:

$$P_\infty = K_{CFRP} d \rho_p^{0.5} (V \cos \theta)^{2/3} - K_2 \frac{m_{MLI}}{\rho_t} \quad (4-13)$$

Typical values for the density of graphite-composites, ρ_t , are 1.5-1.6 g/cm³.

The equations below describe the required CFRP shielding thickness to prevent either detached spall or complete perforation:

$$\text{To prevent detached spallation:} \quad t \geq 3.0 P_{\infty} \quad (4-14)$$

$$\text{To prevent perforation:} \quad t \geq 1.8 P_{\infty} \quad (4-15)$$

For a specific CFRP shielding configuration, the ballistic limit particle size on threshold of a given damage mode can be determined using:

$$d_c = \left[\frac{t + K2(m_{MLI} / \rho_t)}{k K_{CFRP} (\rho_p)^{0.5} (V \cos \theta)^{2/3}} \right] \quad (4-16)$$

Where

d_c = critical projectile diameter on threshold of given damage mode (cm)
 k = damage parameter, either 1.8 or 3.0 for perforation and detached spall, respectively

K_{CFRP} = material parameter for CFRP = 0.52

$K2$ = ballistic performance factor for MLI compared to CFRP = 4.5

m_{MLI} = areal density of MLI thermal blanket (g/cm²)

$P_{\infty Ti}$ = penetration depth in semi-infinite titanium target (cm)

ρ_p = projectile density (g/cm³)

ρ_t = CFRP target density (g/cm³)

t = CFRP thickness (cm)

θ = impact angle from target normal (deg); $\theta = 0^\circ$ impact normal to target

V = projectile velocity (km/s)

Table 4-3 provides an overview of the range in impact conditions that the aluminum BLEs have been validated by HVI test.

Table 4-3. Application Comments for CFRP BLEs

	Validated for	Applied to	Comments
Materials	CFRP	CFRP	The dependence of ballistic limit on fiber/epoxy type, fiber volume content, weave type, lay-up, etc. are included in the parameter K_{CFRP} which has been validated for a 3.8 mm thick quasi-isotropic laminate. For different configurations, this parameter may require empirical adjustment.
Impact angle	Normal (0°)	Normal, oblique	
Impact velocities	5.8-6.6 km/s	All	

4.1.5 Fiberglass Composite Single-Wall Shields

A penetration equation has been derived for a mixture of e-glass fibers and epoxy resin with density, ρ_t , of 1.8 g/cm³, from test data provided in [23]:

$$P_{FG} = 0.434 d \left(\frac{\rho_p}{\rho_t} \right)^{0.5} (V \cos \theta)^{2/3} \quad (4-17)$$

To prevent perforation of the fiberglass plate, the thickness of the fiberglass is given by the following equation.

$$t_{FG} \geq 1.8 P_{FG} \quad (4-18)$$

The diameter of the impacting particle that will be at the perforation of a fiberglass plate of thickness, t_{FG} , is:

$$d = 1.28 t_{FG} \left(\frac{\rho_p}{\rho_t} \right)^{-0.5} (V \cos \theta)^{(-2/3)} \quad (4-19)$$

Where

d = projectile diameter (cm)

P_{FG} = penetration depth in semi-infinite fiberglass target (cm)

ρ_p = projectile density (g/cm³)

ρ_t = target density (g/cm³)

t_{FG} = thickness of fiberglass target (cm)

θ = impact angle from target normal (deg); $\theta = 0^\circ$ impact normal to target

V = projectile velocity (km/s)

4.1.6 Effect of MLI on Ballistic Limits

MLI thermal blankets added to the top of a single-wall shield can have a significant effect on the ballistic performance of the shield. For the case of an MLI blanket that is directly over the single wall, without a gap between the MLI and the single wall, the following equation can be used to find the diameter of the impacting particle that is a the perforation limit of the plate under the MLI (i.e., failure criteria = perforation of plate under the MLI):

$$d_c = 2.2 m_{MLI} \rho_p^{-0.47} (V \cos \theta)^{-0.63} + d_{c_without MLI} \quad (4-20)$$

Where

d_c = critical projectile diameter at threshold of shield failure (cm)

$d_{c_without MLI}$ = critical projectile diameter at shield failure without MLI (cm)

m_{MLI} = areal density of the MLI blanket (g/cm^2)

ρ_p = projectile density (g/cm^3)

θ = impact angle from target normal (deg); $\theta = 0^\circ$ impact normal to target

V = projectile velocity (km/s)

4.2 Dual-Wall Whipple Shield

The Whipple shield consists of a single bumper followed at a distance by the rear wall. Generally, an MLI thermal blanket is placed on the exterior of the bumper, or in the space between the bumper and rear wall. For ISS crew modules, the rear wall serves as a pressure shell that contains atmospheric pressure and is, therefore, under hoop and longitudinal stress. This stress is a relatively low fraction of the yield strength of the material (<25% for most ISS modules), and the presence of stress does not influence the protection limits of the shield (for perforation and/or detached spall). The gap between the outer bumper and rear wall is under vacuum (even for ISS crew modules). The function of the first wall, the “bumper,” is to break up an impacting MMOD particle into a cloud of material that expands while moving across the gap, resulting in the impactor energy and momentum being distributed over a wide area of the rear wall. This approach is more mass-effective than a single-wall shield at defeating a hypervelocity MMOD particle. However, a disadvantage is the additional volume needed for the Whipple shield compared to a single-wall shield. The thickness and material properties of the bumper and rear wall are important in breaking up and eventually defeating the projectile, as summarized in the following section on the physics of a Whipple shield impact. A much more extensive discussion of the physics underlying HVI into spacecraft shielding can be found elsewhere [27-31].

4.2.1 Impact Physics

A key factor governing the performance of spaced shields is the state of the debris cloud, generated after HVI, that is projected behind the bumper toward the rear wall. The debris cloud contains a mixture of solid, liquid, and/or vaporized materials from the bumper and projectile depending on the impact pressures generated in the projectile and bumper at impact, and the thermal and mechanical properties of the materials involved. Solid fragments in the debris cloud are generally more penetrating when they contact the rear wall than liquid or vapor. The higher the impact pressure, the fewer solid fragments and greater melt/vapor contained in the debris cloud [32]. Impact pressure increases as projectile velocity increases, impact obliquity angle decreases (i.e., becomes more normal), and the density of projectile and target increase.

The shock waves that move through the projectile and first bumper after impact are complex. The initial compressive shock wave compresses the bumper and target materials to high density and temperature. Compressive waves are reflected as a tensile or rarefaction wave at free surfaces from the back of the bumper and sides of the projectile. If the stress near the free surface exceeds the tensile strength of the material, spall planes will occur and material is ejected from the free surfaces. The rarefaction wave moves at faster speeds through high-density compressed material. As this material is released from high pressure and density by the rarefaction wave, internal energy is raised and temperatures can exceed melting or vaporization temperatures. If the bumper is too thin, the rarefaction wave will overtake the compressive wave moving through the projectile, degrading it and preventing a portion of the projectile from being adequately shocked to induce melting or vaporization, resulting in solid projectile fragments. However, if the bumper is too thick relative to the projectile, release of solid bumper fragments is possible.

Figure 4-4 illustrates a typical ballistic limit curve for a Whipple shield, for normal impact by an aluminum sphere, and assuming the Whipple shield is made from an aluminum alloy. This curve shows the critical aluminum projectile diameter on the threshold of shield failure. Failure is defined as either perforation or detached spall from the rear wall of the shield. The Whipple shield ballistic limit is compared to a monolithic, single aluminum plate of the same mass as the combined Whipple shield bumper and rear wall. Three different penetration regimes are defined for a Whipple shield, depending on normal component velocity of the impactor, which determines the resulting impact pressure and state of the debris cloud: (1) deforming projectile regime; (2) projectile fragmentation/melt regime; and (3) projectile melt/vaporization regime.

In the deforming projectile regime, below normal component impact velocities (V_n) of 3km/s, the impact shock pressures are so low that the projectile deforms but remains essentially intact after bumper impact. Some spall may occur in the projectile, but the projectile and bumper fragments in the debris cloud are characteristically solid in this velocity range. A deformed but substantially intact projectile then impacts the shield's rear wall at a substantial fraction of the initial impact speed ($>80\%$ for bumper thickness to projectile diameter ratio of 0.2). Because of this, Whipple shield performance generally suffers if impacted by projectiles near a normal component

velocity of 3km/s. In deforming projectile regime, the projectile becomes more damaging as speed increases. Target material strength, hardness and thickness are important parameters influencing penetration resistance in this regime.

In the projectile fragmentation/melt regime, between normal component impact velocities of 3 km/s and 7 km/s, the projectile is exposed to intense enough stress waves and heating that it fragments. Projectile fragmentation extent increases as velocity increases, and the effectiveness of the shield is predicted to increase with velocity in the projectile fragmentation regime. Above about V_n of 5.5 km/s, the projectile begins to melt [27, 29]. Thus, the debris cloud in the fragmentation/melt regime is composed of both solid and melted particles and droplets, with the proportion of melt increasing with velocity. As the debris cloud expands across the space between bumper and rear wall, the rear wall is exposed to distributed point loads from multiple small (relative to the initial projectile size) solid fragments and melt particles. Properties that influence penetration resistance in this regime include: bumper strength, density, equation-of-state, thickness, and thermodynamic properties (melt temperature, latent heat of fusion, etc.); bumper standoff distance from the rear wall; and rear wall strength and thickness.

In the projectile melt/vaporization regime, above V_n of 7 km/s, it is assumed that fragmentation of the projectile has essentially reached its limit, and increases in projectile velocity lead to higher loading of the rear wall from a debris cloud that consists mostly of molten materials. The important shielding variables that influence protection performance in this regime include bumper density, thickness, and equation-of-state; standoff distance, as well as rear wall thickness and strength. Above V_n of 10 km/s for aluminum-on-aluminum impacts, the temperature of some of the projectile material upon release from shock compressed state equals/exceeds the vaporization temperature for aluminum, and vaporization is complete above V_n of 24 km/s based on one-dimensional calculations [29]. The debris cloud in this regime is expected to contain increasing amounts of vaporized projectile/bumper material above 10 km/s (for aluminum-on-aluminum impacts). However, there is also a possibility the debris cloud in this regime can contain solid materials, either from the projectile and/or bumper, depending on bumper thickness to projectile diameter ratio. Table 4-4 provides a summary of CALE hydrocode calculations on the fraction of projectile in either solid or liquid states as a function of impact velocity, and bumper thickness to projectile diameter ratio (t/d). CALE is a two-dimensional arbitrary Lagrangian Eulerian material dynamics computer model. The results from the CALE calculations indicate for impacts at and above 8 km/s, there is a significant fraction of projectile material that does not reach complete melt state. This is in disagreement with theory based on one-dimensional models, that aluminum projectiles should be completely melted above 7 to 8 km/s [29]. Primarily the explanation for this is that two- and three-dimensional effects include free-surface reflections not present in one-dimensional calculations, that act to degrade compressive shock waves in the projectile, increasing the likelihood of solid fragments in the debris cloud. Additionally, impact from non-spherical projectiles, depending on shape, can result in lower fraction of the projectile exposed to pressures that result in complete disruption and melting/vaporization. The debris cloud state influences how shield performance is extrapolated into velocities beyond test data. If the debris cloud consists mainly of molten and vaporized materials, the debris cloud produces an impulsive load to the rear wall,

which implies the rear wall thickness scales with impactor momentum [27]. However, if the debris cloud contains solid fragments, cratering results from the point loads in the debris cloud, and rear wall thickness will scale with impactor kinetic energy.

For impact speeds less than 7 km/s, impact data exists to establish the performance limits of spacecraft shielding and materials. Above 7 km/s, there is very limited experimental data. Therefore, a conservative approach has been taken to Whipple shield BLEs above 7 km/s, to extrapolate to higher velocities with constant kinetic energy, due to the greater possibility of some solid material in the debris cloud with a single bumper. For double- and multiple-bumper systems, which are more effective at breaking up and thermally processing projectiles into a debris cloud consisting of molten materials, an assumption that shield rear wall thickness scales with constant momentum is used [10, 33].

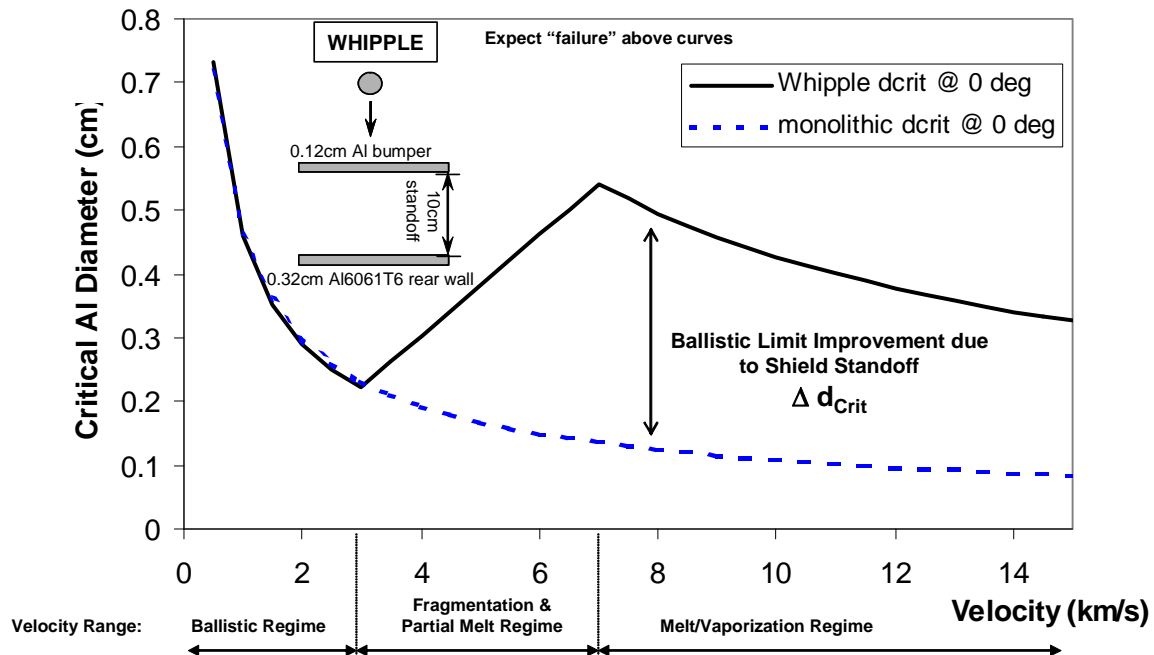


Figure 4-4. Ballistic limits for equal mass monolithic and Whipple shields. Monolithic target is 0.44 cm thick Al 6061-T6. Whipple shield consists of 0.12 cm thick Al 6061T6 bumper followed at 10 cm by 0.32 cm thick Al 6061T6 rear wall.

Table 4-4. CALE Hydrocode Results for Projectile Solid/Liquid Fraction in the Debris Cloud as a Function of Velocity (V) and Bumper Thickness to Projectile Diameter Ratio (t/d)

Fraction of Projectile in debris cloud that is melted					
t/d	V=6 km/s	V=8 km/s	V=10 km/s	V=12 km/s	V=14 km/s
0.05	0.05	0.15	0.31	0.42	0.55
0.1	0.05	0.28	0.55	0.75	0.89
0.2	0.06	0.29	0.75	0.97	0.99
0.3	0.06	0.31	0.77		
0.5	0.06	0.32	0.82		
0.8	0.06		0.95		

4.2.2 Whipple Shield Design Equations

The following equations were provided in earlier work [34], and represent equations that can be used for preliminary design of MMOD protection using Whipple shields. Additional analyses supported by tests will be necessary to show preliminary shield designs meet or exceed MMOD protection requirements. Bumper and rear wall thickness to defeat a given threat particle are determined by the following equations (assuming $V_n \geq 7$ km/s).

$$t_b = c_b m_p / \rho_b = c_b d \rho_p / \rho_b \quad (4-21)$$

Where

c_b = coefficient 0.25 when $S/d < 30$, and $c_b = 0.2$ when $S/d \geq 30$

d = projectile diameter (cm)

m_p = projectile areal density (g/cm^2)

ρ_p = projectile density (g/cm^3)

ρ_b = bumper density (g/cm^3)

S = overall spacing between outer bumper and rear wall (cm)

t_b = bumper thickness (cm)

$$t_w = c_w d^{0.5} (\rho_p \rho_b)^{1/6} (M_p)^{1/3} V_n / S^{0.5} (70/\sigma)^{0.5} \quad (4-22)$$

Where

c_w = coefficient $0.16 \text{ cm}^2\text{-sec}/(\text{g}^{2/3} \text{ km})$

d = projectile diameter (cm)

M_p = projectile mass (g)

ρ_p = projectile density (g/cm^3)

ρ_b = bumper density (g/cm^3)

S = overall spacing between outer bumper and rear wall (cm)

σ = rear wall yield stress (ksi)
 t_w = rear wall thickness (cm)
 V = projectile velocity (km/s)
 V_n = normal component of projectile velocity (km/sec)

4.2.3 Whipple Shield Performance Equations

The following equations [34] define the protection capability limits for a Whipple shield in terms of a critical particle size (d_c) that causes failure (complete penetration or detached spall of the rear wall). These equations assume that the bumper thickness is adequate to disrupt the projectile at high velocities; i.e., that equation 4-20 is satisfied (for $V_n = 7$ km/s). If the bumper is too thin, then the following equations overestimate the performance of the shield. If the bumper is too thick, then the extra bumper mass is not effective; i.e., shield performance will not suffer, but the extra bumper mass will not improve shielding performance (unless the bumper becomes very thick; i.e., the thickness is greater than the diameter of the projectile at the shield's ballistic limit).

At higher velocities, the debris cloud impacting the rear wall will contain various amounts of solid, liquid, and vapor components of the projectile depending on impact conditions (projectile size, impact speed, obliquity, projectile density, shape, and bumper thickness). The critical particle size for $V_n \geq 7$ km/s is given by

$$d_c = 3.918 t_w^{2/3} \rho_p^{-1/3} \rho_b^{-1/9} (V \cos \theta)^{-2/3} S^{1/3} (\sigma / 70)^{1/3} \quad (4-23)$$

Where

d_c = critical projectile diameter at shield failure threshold (cm)
 ρ_p = projectile density (g/cm³)
 σ = rear wall yield stress (ksi)
 S = standoff distance from back of bumper to front of rear wall (cm)
 t_w = rear wall thickness (cm)
 θ = impact angle from target normal (deg); note impact at $\theta = 0$ deg is normal to the target.
 V = projectile velocity (km/s)
 V_n = normal component of projectile velocity (km/sec) = $V \cos \theta$

At low velocities, below 3 km/s, impact shock pressures are low and the projectile remains essentially intact after impact on the bumper. The shield's rear wall is then impacted by a deformed or slightly fragmented projectile. The critical particle size for $V_n \leq 3$ km/s is given by

$$d_c = \left[\left(t_w (\sigma / 40)^{0.5} + t_b \right) / \left(0.6 (\cos^{5/3} \theta) \rho_p^{0.5} V^{2/3} \right) \right]^{(18/19)} \quad (4-24)$$

Where

d_c = critical projectile diameter at shield failure threshold (cm)

ρ_p = projectile density (g/cm³)
 σ = rear wall yield stress (ksi)
 t_b = bumper thickness (cm)
 t_w = rear wall thickness (cm)
 θ = impact angle from target normal (deg); note impact at $\theta = 0$ deg is normal to the target.
 V = projectile velocity (km/s)
 V_n = normal component of projectile velocity (km/sec) = $V \cos\theta$

The projectile is more damaging as velocity increases in the low-velocity regime, resulting in the critical particle size decreasing as velocity increases. At velocities above $V_n=3$ km/s, projectile fragmentation during the collision with the bumper becomes significant. Above 5.5 km/s, the projectile will begin to melt for aluminum on aluminum impacts [29]. A fragmenting or partially molten projectile is less damaging to the rear wall than a substantially intact projectile, thus critical particle size increases in the intermediate velocity range: $3 \text{ km/s} < V_n \leq 7 \text{ km/s}$:

$$d_c = \left[\left(t_w (\sigma/40)^{0.5} + t_b \right) / \left(1.248 \rho_p^{0.5} \cos\theta \right) \right]^{(18/19)} \times [1.75 - (V_n/4)] + \left[1.071 t_w^{2/3} \rho_p^{-1/3} \rho_b^{-1/9} S^{1/3} (\sigma/70)^{1/3} \right] \times (V_n/4 - 0.75) \quad (4-25)$$

Where

d_c = critical projectile diameter at shield failure threshold (cm)
 ρ_b = bumper density (g/cm³)
 ρ_p = projectile density (g/cm³)
 σ = rear wall yield stress (ksi)
 S = standoff distance from back of bumper to front of rear wall (cm)
 t_b = bumper thickness (cm)
 t_w = rear wall thickness (cm)
 θ = impact angle from target normal (deg); note impact at $\theta = 0$ deg is normal to the target.
 V = projectile velocity (km/s)
 V_n = normal component of projectile velocity (km/sec) = $V \cos\theta$

For highly oblique impacts ($\theta \geq 65^\circ$), bumper fragments contribute the majority of damage to the rear wall. Thus, the critical particle size for impact angles over 65° should be set to the critical particle size for 65° (to prevent over-prediction of the critical projectile diameter) as given by

$$d_c^{\theta > 65} = d_c^{\theta = 65} \quad (4-26)$$

4.2.4 Whipple Shield Performance Equations as Function of Bumper Thickness

Sometimes it is not practical to design Whipple shielding with bumper thickness satisfying equation 4-20. In these cases, the following BLEs can be used to predict shield performance [35]. These equations were based on a modified version of Johnson Space Center (JSC) standard Whipple shield equations [34]. For $V_n \geq 7$ km/s, the critical particle size at failure threshold of the shield's rear wall is given by

$$d_c = 3.918 F_2^{-2/3} t_w^{2/3} \rho_p^{-1/3} \rho_b^{-1/9} (V \cos \theta)^{-2/3} S^{1/3} (\sigma / 70)^{1/3} \quad (4-27)$$

F_2 is given by

$$F_2 = 1; \quad \text{when } (t_b/d_c)_{V_n=7 \text{ km/s}} \geq (t_b/d)_{crit} \quad (4-28)$$

$$F_2 = r_{S/D} - 10 \frac{t_b}{d_c} (r_{S/D} - 1) + 25 \left(\frac{t_b}{d_c} \right)^2 (r_{S/D} - 1); \quad \text{when } (t_b/d_c)_{V_n=7 \text{ km/s}} < (t_b/d)_{crit} \quad (4-29)$$

The term, $r_{S/D}$, is the ratio between the required rear wall thickness when no bumper is present, t_w when $t_b=0$, and the rear wall thickness when the bumper is properly sized by equation 4-20. Note that F_2 and $r_{S/D}$ are found once for a given shield configuration at $V_n = 7$ km/s, and values for d_c and F_2 will need to be found iteratively using equations 4-26 and 4-28.

$$(r_{S/D}) = \left(\frac{t_w \text{ when } (t_b = 0)}{t_w \text{ when } (t_b/d_c) = (t_b/d)_{crit}} \right) \quad (4-30)$$

As given in equation 4-20, $(t_b/d)_{crit}$ values are as follows.

$$(t_b/d)_{crit} = 0.2 \left(\frac{\rho_p}{\rho_b} \right) \quad \text{when } S/d \geq 30 \quad (4-31)$$

$$(t_b/d)_{crit} = 0.25 \left(\frac{\rho_p}{\rho_b} \right) \quad \text{when } S/d < 30 \quad (4-32)$$

Where

d_c = critical projectile diameter at shield failure threshold (cm)

F_2 = coefficient that corrects for low t_b/d ratios, and depends on d_c

ρ_b = bumper density (g/cm^3)

ρ_p = projectile density (g/cm^3)

σ = rear wall yield stress (ksi)

$r_{S/D}$ = ratio of rear wall thickness without bumper to rear wall thickness with bumper (equation 4-29)

S = standoff distance from back of bumper to front of rear wall (cm)

t_w = rear wall thickness (cm)
 θ = impact angle from target normal (deg); note impact at $\theta = 0$ deg is normal to the target.
 V = projectile velocity (km/s)
 V_n = normal component of projectile velocity (km/sec) = $V \cos\theta$

The low-velocity equation in [35] is based on earlier work given in [36]:

For $V_n \leq V_{\text{low-lim}}$,

$$d_c = \left(\frac{(t_w / k + t_b)}{0.796 K_\infty \rho_p^{0.518} V_n^{2/3}} \right)^{(18/19)} \quad (4-33)$$

The low-velocity to intermediate transition velocity, $V_{\text{low-lim}}$, is defined by [37] for aluminum projectile on aluminum targets as:

$$V_{\text{low-lim}} = 1.853 + 0.397 \left(\frac{t_b}{d_c} \right)^{-0.565} \quad (4-34)$$

Where

d_c = critical projectile diameter at shield failure threshold (cm)
 k = constant based on rear wall failure criterion = 0.18 for perforation of rear wall, 0.22 for detached spall, and 0.3 for incipient attached spall of rear wall
 K_∞ = material constant = 0.42 for aluminum alloys, and 0.25 for steel alloys
 ρ_p = projectile density (g/cm³)
 t_b = bumper thickness (cm)
 t_w = rear wall thickness (cm)
 θ = impact angle from target normal (deg); note impact at $\theta = 0$ deg is normal to the target.
 V = projectile velocity (km/s)
 V_n = normal component of projectile velocity (km/sec) = $V \cos\theta$

For normal component velocities between the low-velocity limit and 7 km/s, a linear interpolation is used as in equation 4-24.

4.2.5 Effect of MLI on Whipple Shield Performance Equations

The location of the MLI thermal blanket relative to the bumper and rear wall effect influences the ballistic performance of Whipple shields. MLI closer to the rear wall is more effective in increasing ballistic performance.

Equations for assessing the increase in the critical particle size for Whipple shields with MLI are given by [10]:

$$\text{for } V_n \geq V_{Hi-Lim}; \quad d_c \text{ with MLI} = d_c \text{ without MLI} + \Delta_{MLI} \quad (4-35)$$

$$\Delta_{MLI} = k_{MLI} m_{MLI} (S_{MLI} / S)^{0.5} \quad (4-36)$$

Where

d_c = critical projectile diameter at shield failure threshold (cm)

Δ_{MLI} = change in critical particle size in high-velocity regime due to MLI (cm)

k_{MLI} = MLI constant = 1.4 cm³/g

m_{MLI} = MLI areal density (g/cm²)

S = standoff distance from back of bumper to front of rear wall (cm)

S_{MLI} = gap distance from back of bumper to front of MLI (cm)

θ = impact angle from target normal (deg); note impact at $\theta = 0$ deg is normal to the target.

V = projectile velocity (km/s)

V_{Hi-Lim} = intermediate to high transition velocity = 7 km/s

V_n = normal component of projectile velocity (km/s) = $V \cos \theta$

Also, when MLI is present, the low-velocity to intermediate-velocity transition occurs earlier; i.e.,

$V_{Lo-Lim} = 2$ km/s with MLI

$V_{Lo-Lim} = 3$ km/s without MLI

4.2.6 Performance Equations for ISS Whipple Shields

The approach taken to satisfy safety requirements for human-occupied spacecraft includes performing a final impact tests on flight-realistic hardware, after which updates are made to BLEs as necessary to match available impact data. These BLEs are used to update MMOD risk assessments.

Updated BLEs resulting from impact tests on ISS Whipple shields including MLI thermal blankets and flight realistic materials are given by the following equations. These equations are valid for specific shields, as defined in Table 4-5. For these equations, the failure criteria is no penetration or detached spall from the rear wall.

High-Velocity: when $V \geq V_H/(\cos \theta)^{x_h}$,

$$d_c = K_H \rho_p^{-1/3} (V \cos \theta)^{-2/3} \quad (4-37)$$

Intermediate-Velocity: when $V_L/(\cos \theta)^{x_l} < V < V_H/(\cos \theta)^{x_h}$,

$$d_c = \frac{K_{hi} \rho_p^{-1/3} (\cos \theta)^{(-2/3 + 2.xh/3)}}{\left[\frac{V - V_L (\cos \theta)^{-xl}}{V_H (\cos \theta)^{-xh} - V_L (\cos \theta)^{-xl}} \right]} + K_{li} \rho_p^{-0.5} (\cos \theta)^{(-4/3 + el + 2.xl/3)} \frac{\left[\frac{V_H (\cos \theta)^{-xh} - V}{V_H (\cos \theta)^{-xh} - V_L (\cos \theta)^{-xl}} \right]}{\left[\frac{V_H (\cos \theta)^{-xh} - V}{V_H (\cos \theta)^{-xh} - V_L (\cos \theta)^{-xl}} \right]} \quad (4-38)$$

Low-Velocity: when $V \leq V_L/(\cos \theta)^{xl}$,

$$d_c = K_L (\cos \theta)^{(-4/3 + el)} \rho_p^{-1/2} V^{-2/3} \quad (4-39)$$

There is an impact angle constraint for oblique impacts above 65° ; i.e.,

$$d_c (\theta > 65^\circ) = d_c (\theta = 65^\circ) \quad (4-40)$$

Where

d_c = critical projectile diameter at shield failure threshold (cm)

ρ_p = projectile density (g/cm^3)

K_H = high-velocity coefficient ($\text{g}^{1/3} \text{ km}^{2/3} \text{ s}^{-2/3}$)

K_{hi} = high intermediate velocity coefficient ($\text{g}^{1/3}$)

K_L = low-velocity coefficient ($\text{g}^{1/2} \text{ cm}^{-1/2} \text{ km}^{2/3} \text{ s}^{-2/3}$)

K_{li} = low intermediate velocity coefficient ($\text{g}^{1/2} \text{ cm}^{-1/2}$)

m_{MLI} = MLI areal density (g/cm^2)

S = standoff distance from back of bumper to front of rear wall (cm)

S_{MLI} = gap distance from back of bumper to front of MLI (cm)

θ = impact angle from target normal (deg); note impact at $\theta = 0$ deg is normal to the target.

V = projectile velocity (km/s)

V_H = intermediate to high transition velocity (km/s)

V_L = low to intermediate transition velocity (km/s)

V_n = normal component of projectile velocity (km/s) = $V \cos \theta$

el = exponent

xl = low-velocity exponent

xh = high-velocity exponent

ISS Whipple shields are used in areas of the cylinder and ECs of the US Laboratory (USL) and Node modules, as well as the Service Module (SM) large and small diameter cylinder sections. For the USL and Nodes, Whipple shields provide protection where MMOD impact rates are expected to be lowest, whereas Nextel/Kevlar stuffed Whipple shields are used where MMOD impact rates are higher. Table 4-5 provides ISS Whipple shield parameters and coefficients for the updated BLEs.

Table 4-5. BLE Coefficients and Shield Parameters for ISS Whipple Shields

	USL Cylinder	USL EC	Node Forward Cylinder	Node Aft Cylinder	Node EC #1	Node EC #2	SM Small Diameter Cylinder	SM Large Diameter Cylinder
Mat'l t_b	Al6061T6	Al6061T6	Al6061T6	Al6061T6	Al6061T6	Al6061T6	AMG-6	AMG-6
Mat'l t_w	Al2219T87	Al2219T87	Al2219T87	Al2219T87	Al2219T87	Al2219T87	AMG-6	AMG-6
t_b (cm)	0.20	0.20	0.13	0.13	0.13	0.20	0.10	0.10
S (cm)	10.7	22.2	10.7	10.9	22.2	22.1	5.0	5.0
S_{MLI} (cm)	3.8	3.8	3.8	3.8	3.8	3.8	4.5	4.5
t_w (cm)	0.48	0.48	0.64	0.41	0.58	0.58	0.16	0.16
m_{MLI} (g/cm ²)	0.054	0.054	0.054	0.054	0.054	0.054	0.06	0.06
K_H	4.643	5.910	4.085	3.643	4.980	6.329	0.553	0.710
K_{hi}	1.269	1.615	1.116	0.977	1.361	1.730	0.151	0.194
K_{li}	0.892	0.891	0.685	0.524	0.679	0.736	0.074	0.093
K_L	1.168	1.168	1.262	0.687	1.078	1.169	0.154	0.194
V_H (km/s)	7.0	7.0	7.0	7.2	7.0	7.0	7.0	7.0
V_L (km/s)	1.5	1.5	2.5	1.5	2.0	2.0	3.0	3.0
xh	1.0	1.0	1.0	1.0	1.0	1.0	1.0	1.0
xl	1.9	1.9	1.9	1.5	1.0	1.0	1.0	1.0
el	<60°; -1/3 ≥60°; -2/3	-0.5	<60°; -1 ≥60°; -2/3	<60°; -1/3 ≥60°; -2/3	<60°; -1/6 ≥60°; -2/3	-0.5	-1/3	-1/3

4.2.7 Performance Equations for ISS Node Whipple Shields

The Whipple shields on ISS Node 2 and 3 (Node 2/3) modules are slightly different from the Whipple shields on Node 1. Node 2/3 standoff distance is greater than in Node 1, and the MLI thermal blanket is mounted directly behind the Node 2/3 bumper (figure 4-5). The reason for these differences is partly that the Node 2/3 modules were manufactured by European Space Agency (ESA)/Alenia, while NASA/Boeing was responsible for Node 1 production. Impact tests were performed on realistic samples of the Node 2/3 Whipple shields including MLI (0.05 g/cm²), and BLEs were updated based on the results, using previous ESA/Alenia Whipple equations as the starting point for the update [38]. For these equations, failure is defined as a perforation (complete penetration, through-hole, or through-crack) of the rear wall (pressure shell) or detached spall from the back of the rear wall. This failure mode would lead to air leak and internal fragments, which endangers crew survivability. It can be noted that “detached spall” without a perforation of the rear wall is not a common type of failure. It is much more likely to completely penetrate the rear wall than to have detached spall without penetration.

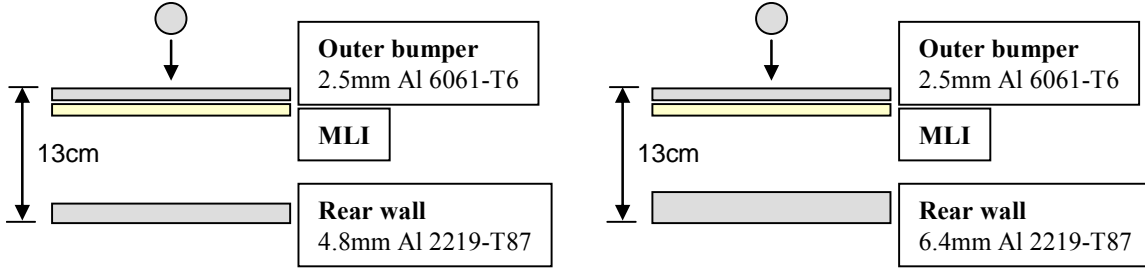


Figure 4-5. ISS Node Whipple shields.

The following equations were modified from the previous BLEs used by Alenia in Node 2/3 risk assessments [39], to fit results from HVI tests. The modified equations increase the predicted ballistic limits at the low and intermediate velocities to fit the test data for low-obliquity impacts, but decreased at high velocities to fit the test data.

Low-velocity, $V \leq V_L (\cos\theta)^x$:

$$d_c = \left[\frac{t_w / K_{3s} (\sigma / 40)^{0.5} + t_b}{K_L (\cos \theta)^{\exp L} \rho_p^{0.5} V^{2/3}} \right]^{18/19} \quad (4-41)$$

Where

d_c = critical projectile diameter at shield failure threshold (cm)

ρ_p = projectile density (g/cm³)

K_{3s} = low-velocity constant

K_L = low-velocity coefficient

t_b = bumper thickness (cm)

t_w = rear wall thickness (cm)

θ = impact angle from target normal (deg); note impact at $\theta = 0$ deg is normal to the target.

σ = rear wall yield stress (ksi)

V = projectile velocity (km/s)

V_L = low to intermediate transition velocity (km/s)

$\exp L$ = low-velocity angle exponent

x = low-velocity exponent

High-velocity, $V \geq V_H (\cos\theta)^y$:

$$d_c = K_H K_{3d}^{-2/3} t_w^{2/3} \rho_p^{-1/3} \rho_b^{-1/9} (\sigma / 70)^{1/3} V^{-2/3} (\cos \theta)^{\exp H} S^{1/3} \quad (4-42)$$

Where

d_c = critical projectile diameter at shield failure threshold (cm)

ρ_b = bumper density (g/cm³)
 ρ_p = projectile density (g/cm³)
 K_{3d} = high-velocity constant
 K_H = high-velocity coefficient
 t_w = rear wall thickness (cm)
 θ = impact angle from target normal (deg); note impact at $\theta = 0$ deg is normal to the target.
 S = standoff distance from back of bumper to front of rear wall (cm)
 σ = rear wall yield stress (ksi)
 V = projectile velocity (km/s)
 V_H = intermediate to high transition velocity (km/s)
 $\exp H$ = high-velocity angle exponent
 y = high-velocity exponent

Intermediate-velocity, $V_L (\cos\theta)^x < V < V_H (\cos\theta)^y$:

$$\begin{aligned}
 d_c = & \left[\frac{(t_w / K_{3s})(\sigma / 40)^{0.5} + t_b}{K_{Li} (\cos\theta)^{(\exp L + 2x/3)} \rho_p^{0.5}} \right]^{(18/19)} \times \left[\frac{V_H \cos^y \theta - V}{V_H \cos^y \theta - V_L \cos^x \theta} \right] \\
 & + \left[K_{Hi} K_{3d}^{-2/3} t_w^{2/3} \rho_p^{-1/3} \rho_b^{-1/9} (\cos\theta)^{(\exp H - 2y/3)} S^{1/3} (\sigma / 70)^{1/3} \right] \times \left[\frac{V - V_L \cos^x \theta}{V_H \cos^y \theta - V_L \cos^x \theta} \right] \\
 & (4-43)
 \end{aligned}$$

Where

d_c = critical projectile diameter at shield failure threshold (cm)
 ρ_b = bumper density (g/cm³)
 ρ_p = projectile density (g/cm³)
 K_{3d} = high-velocity constant
 K_{3s} = low-velocity constant
 K_H = high-velocity coefficient
 K_{Hi} = high-intermediate velocity coefficient
 K_L = low-velocity coefficient
 K_{Li} = low-intermediate velocity coefficient
 t_b = bumper thickness (cm)
 t_w = rear wall thickness (cm)
 θ = impact angle from target normal (deg); note impact at $\theta = 0$ deg is normal to the target.
 S = standoff distance from back of bumper to front of rear wall (cm)
 σ = rear wall yield stress (ksi)
 V = projectile velocity (km/s)
 V_H = intermediate to high transition velocity (km/s)
 V_L = low to intermediate transition velocity (km/s)

expH = high-velocity angle exponent
expL = low-velocity angle exponent
x = low-velocity exponent
y = high-velocity exponent

There is a cutoff angle for oblique impacts above 65° ; i.e.,

$$\text{for } \theta > 65^\circ, \quad d_c = d_c(\theta = 65^\circ) \quad (4-44)$$

Table 4-6. Parameters for Node 2/3 Whipple Shield BLEs

Parameter	Value when $\theta < 60^\circ$	Value when $\theta \geq 60^\circ$
V_L	3.3	2.4
x	-1/3	-2/3
expL	1/3	0.8
K_L	0.5	0.5
K_{3s}	0.7	0.7
K_{Li}	1.108	0.896
V_H	6.8	6.8
y	-0.8	-0.8
expH	-2/3	-2/3
K_H	1.1	1.1
K_{3d}	0.16	0.16
K_{Hi}	0.306	0.306

Figure 4-6 shows predicted ballistic limits from the Node 2/3 Whipple equations using the following shield conditions, as well as impact data compared to the predictions [38].

t_b = 0.16 cm Al 6061-T6 bumper thickness

t_w = 0.48 cm Al 2219-T87 rear wall thickness

σ = 57 ksi rear wall yield strength (note, 1 ksi = 1000 psi = 6.895 MPa),

ρ_p = 2.796 g/cm³ projectile density,

ρ_b = 2.713 g/cm³ bumper density,

S = 12.217 cm shield standoff distance between bumper and rearwall

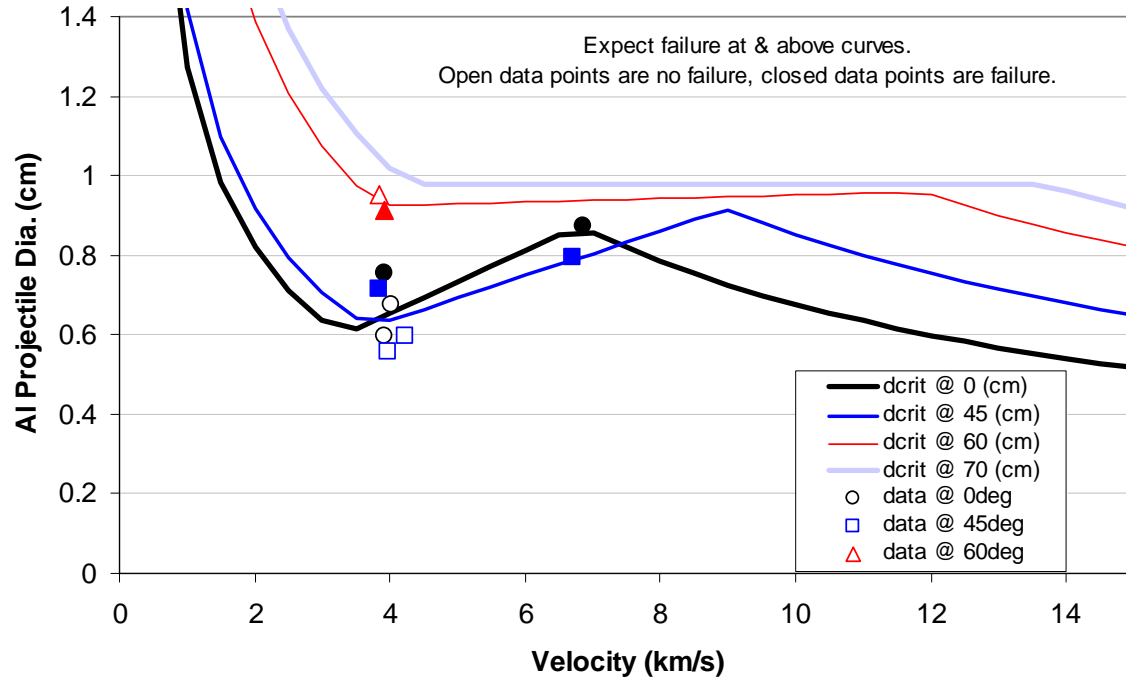


Figure 4-6. Predicted ballistic limits for Whipple shield using Node 2/3 BLEs with 0.16-cm-thick bumper, 12 cm standoff, and 0.48-cm-thick rear wall.

Figure 4-7 shows predicted ballistic limits from the Node 2/3 Whipple equations using the following shield conditions, as well as impact data compared to the predictions [38].

$t_b = 0.25$ cm Al 6061-T6 bumper thickness

$t_w = 0.64$ cm Al 2219-T87 rear wall thickness

$\sigma = 57$ ksi rear wall yield strength (note, 1 ksi = 1000 psi = 6.895 MPa),

$\rho_p = 2.796$ g/cm³ projectile density,

$\rho_b = 2.713$ g/cm³ bumper density,

$S = 12.07$ cm shield standoff distance between bumper and rear wall

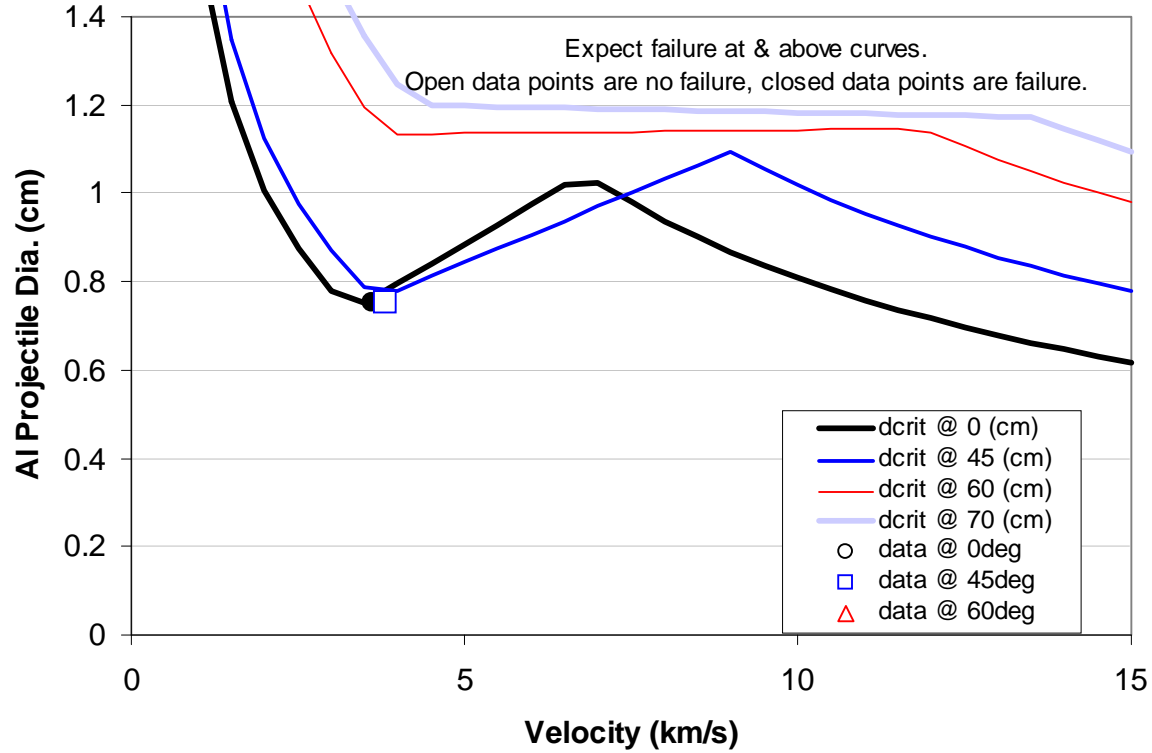


Figure 4-7. Predicted ballistic limits using Node 2/3 BLEs for a Whipple shield with 0.25 cm bumper thickness, 12 cm standoff, and 0.64 cm rear wall thickness.

4.3 Triple-Wall: Nextel/Kevlar Stuffed Whipple Shield

The stuffed Whipple shield includes Nextel ceramic fabric and Kevlar high-strength fabric as “stuffing” between an outer aluminum bumper and shield rear wall (or inner pressure shell) as given in figure 4-8. This shield provides better MMOD protection than conventional two- or three-wall all-aluminum shielding [40, 44]. Semi-empirical design and performance equations follow for Nextel/Kevlar stuffed Whipple shields [10].

4.3.1 Stuffed Whipple Shield Design Equations

The outer bumper thickness is given by

$$t_b = c_b d \rho_p / \rho_b \quad (4-45)$$

The areal density of the Nextel and Kevlar intermediate layer is given by

$$m_{\text{Nextel-Kevlar}} = c_{N-K} d \rho_p \quad (4-46)$$

The Nextel/Kevlar stuffing should be placed halfway between the outer bumper and inner rear wall. Nextel areal density is 75% and Kevlar 25% of the total intermediate

blanket mass per unit area. Suitable results are obtained from Nextel⁴ style AF62 and style AF10 ceramic cloths (areal densities are 0.1 g/cm² for AF62 and 0.027 g/cm² for AF10) although many other Nextel styles, or other ceramic fabrics (such as Astroquartz), or glass cloth fabrics (e- or s-glass fabrics) can be substituted without loss of performance. Kevlar fabric in a ballistic protection weave style (typically plain weave) provides the best protection for the high-strength layer. HVI tests indicate Kevlar KM2, style 705 (0.023 g/cm² areal density) provide best results, although Kevlar 29 style FDI-120 or 710 (0.032 g/cm² areal density) also provide good performance. Other high-strength fabrics such as Spectra have also demonstrated good performance in impact tests [10, 34].

The rear wall thickness is given by

$$t_w = c_w \left[\frac{c_o d \rho_p}{(t_b \rho_p + m_{\text{Nextel-Kevlar}})} \right]^{1.1} M_p^{1/3} V_n (\cos^{0.5} \theta) \rho_w^{-1} S^{-2} (\sigma/40)^{-0.5} \quad (4-47)$$

Where

c_o = coefficient = 0.38

c_b = coefficient = 0.15

c_{N-K} = coefficient = 0.23

c_w = coefficient = 8.84 s/km

d = projectile diameter (cm)

$m_{\text{Nextel-Kevlar}}$ = Nextel and Kevlar areal density (g/cm²)

M_p = projectile mass (g)

ρ_b = outer bumper density (g/cm³)

ρ_p = projectile density (g/cm³)

ρ_w = rear wall density (g/cm³)

S = overall spacing (gap distance) between outer bumper and rear wall (cm)

σ = rear wall yield stress (ksi)

t_b = outer bumper thickness (cm)

t_w = rear wall thickness (cm)

θ = impact angle from target normal (deg); note impact at $\theta = 0$ deg is normal to the target

V = projectile velocity (km/s)

V_n = normal component of projectile velocity (km/s) = $V \cos \theta$

⁴ NextelTM is a product of the 3M Corporation. AstroquartzTM is a product of J.P. Stevens Company. KevlarTM is a product of the DuPont Company. Kevlar KM2 style 705 is a Hexcel Schwebel Company fabric style. Kevlar FDI-120 is a fabric style available from Fabric Development Incorporated.

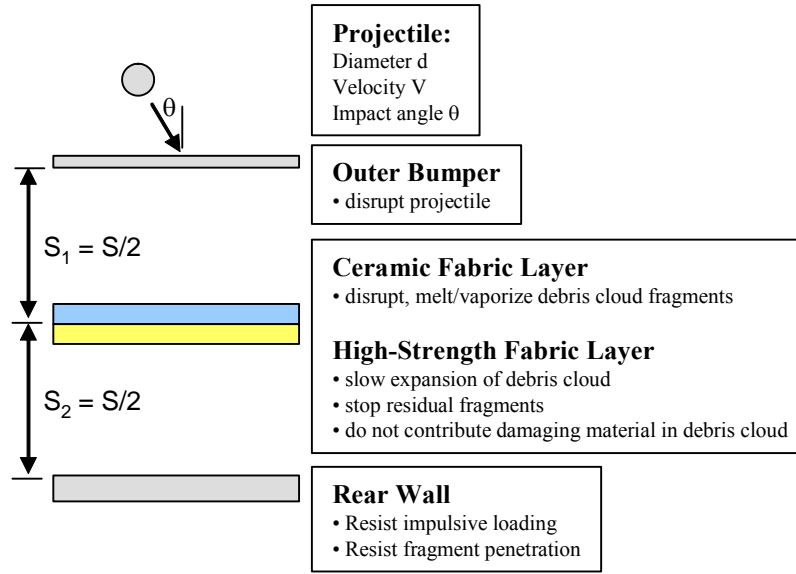


Figure 4-8. Stuffed Whipple shield cross-sectional diagram.

4.3.2 Stuffed Whipple Shield Performance Equations

The following equations predict critical particle size on the failure threshold of stuffed Whipple shields as a function of impact and target parameters [10].

The equations are divided into three penetration regimes, with coefficients and exponents derived from test data. The high-velocity extrapolation beyond the test database is based upon impact momentum scaling. Experimental evidence through 7.5 km/s impact speeds indicates the rear wall is bulged or deflected across a relatively wide area, and results from exposure to blast loading by a debris cloud that contains finely divided particles, liquid, and gas. There are few, if any, craters on the rear wall due to larger solid fragment impact. Previous work indicates that momentum scaling is appropriate for distributed blast loading of the rear wall, whereas kinetic energy scaling is more appropriate when the damage mechanism is cratering from point loads. There is no impact cutoff angle for these equations, as the intermediate blanket protects the rear wall from bumper debris in highly oblique impacts.

High-velocity, $V \geq 6.5 (\cos\theta)^{-0.75}$:

$$d_c = K_{H-SW} (t_w \rho_w)^{1/3} \rho_p^{-1/3} (\sigma/40)^{1/6} V^{-1/3} (\cos\theta)^{-0.5} S^{2/3} \quad (4-48)$$

Where

d_c = critical projectile diameter at shield failure threshold (cm)

$K_{H-SW} = 0.6 (\text{km}^{1/3} \text{s}^{-1/3})$ when $m_{\text{Nextel-Kevlar}} = 0.25m_{\text{shield}}$ to $0.35m_{\text{shield}}$

$K_{H-SW} = 0.45 (\text{km}^{1/3} \text{s}^{-1/3})$ when $m_{\text{Nextel-Kevlar}} = 0.1m_{\text{shield}}$ to $0.15m_{\text{shield}}$

$m_{\text{Nextel-Kevlar}}$ = Nextel and Kevlar areal density (g/cm^2)
 m_{shield} = overall shield areal density (g/cm^2)
 $m_{\text{shield}} = m_{\text{bumper}} + m_{\text{Nextel-Kevlar}} + m_{\text{rear-wall}}$
 ρ_p = projectile density (g/cm^3)
 ρ_w = rear wall density (g/cm^3)
 S = overall spacing (gap distance) between outer bumper and rear wall (cm)
 σ = rear wall yield stress (ksi)
 t_w = rear wall thickness (cm)
 θ = impact angle from target normal (deg); note impact at $\theta = 0$ deg is normal to the target
 V = projectile velocity (km/s)
 V_n = normal component of projectile velocity (km/s) = $V \cos\theta$

Low-velocity, $V \leq 2.6 (\cos\theta)^{-0.5}$:

$$d_c = K_{L-SW} V^{-2/3} (\cos\theta)^{-4/3} \rho_p^{-0.5} \left[t_w (\sigma/40)^{0.5} + C_L m_{b-total} \right] \quad (4-49)$$

Where

C_L = low velocity coefficient = $0.37 (\text{cm}^3/\text{g})$
 d_c = critical projectile diameter at shield failure threshold (cm)
 $K_{L-SW} = 2.35 (\text{g}^{0.5} \text{km}^{2/3} \text{cm}^{-3/2} \text{s}^{-2/3})$
 $m_{b-total}$ = total bumper areal density and is the sum of the areal densities of the outer bumper, Nextel, Kevlar and MLI (g/cm^2):
 $m_{b-total} = m_b + m_{\text{Nextel}} + m_{\text{Kevlar}} + m_{\text{MLI}}$
 ρ_p = projectile density (g/cm^3)
 σ = rear wall yield stress (ksi)
 t_w = rear wall thickness (cm)
 θ = impact angle from target normal (deg); note impact at $\theta = 0$ deg is normal to the target
 V = projectile velocity (km/s)
 V_n = normal component of projectile velocity (km/s) = $V \cos\theta$

Intermediate-velocity, $2.6 (\cos\theta)^{-0.5} < V < 6.5 (\cos\theta)^{-0.75}$:

$$d_c = \left[\frac{K_{Li-SW} \left[t_w (\sigma/40)^{0.5} + C_L m_{b-Total} \right]}{(\cos\theta) \rho_p^{0.5}} \right] \times \left[\frac{6.5 \cos^{-0.75} \theta - V}{6.5 \cos^{-0.75} \theta - 2.6 \cos^{-0.5} \theta} \right] + \left[K_{Hi-SW} (t_w \rho_w)^{1/3} \rho_p^{-1/3} (\cos\theta)^{-0.25} S^{2/3} (\sigma/40)^{1/6} \right] \times \left[\frac{V - 2.6 \cos^{-0.5} \theta}{6.5 \cos^{-0.75} \theta - 2.6 \cos^{-0.5} \theta} \right] \quad (4-50)$$

Where

C_L = low velocity coefficient = 0.37 (cm³/g)

d_c = critical projectile diameter at shield failure threshold (cm)

ρ_b = bumper density (g/cm³)

ρ_p = projectile density (g/cm³)

ρ_w = rear wall density (g/cm³)

$K_{Hi-SW} = 0.321$ when $m_{Nextel-Kevlar} = 0.25m_{shield}$ to $0.35m_{shield}$

$K_{Hi-SW} = 0.241$ when $m_{Nextel-Kevlar} = 0.1m_{shield}$ to $0.15m_{shield}$

$K_{Li-SW} = 1.243$ (g^{0.5} cm^{-3/2})

$m_{b-total}$ = total bumper areal density and is the sum of the areal densities of the outer bumper, Nextel, Kevlar and MLI (g/cm²):

$m_{b-total} = m_b + m_{Nextel} + m_{Kevlar} + m_{MLI}$

S = overall spacing (gap distance) between outer bumper and rear wall (cm)

σ = rear wall yield stress (ksi)

t_w = rear wall thickness (cm)

θ = impact angle from target normal (deg); note impact at $\theta = 0$ deg is normal to the target

V = projectile velocity (km/s)

V_n = normal component of projectile velocity (km/s) = $V \cos\theta$

Table 4-7 provides impact test data on a variety of stuffed Whipple designs (see Table 4-8 for definition of the shields). Note: Tests were performed on all-aluminum, three-wall shields of the same mass per unit area as a Nextel/Kevlar stuffed Whipple shield. Most tests were conducted on two-stage light-gas guns, with velocities of 7.5 km/s and less. Some tests were conducted at impact speeds of over 11 km/s with an ISCL at SwRI [40, 41]. Other tests were performed at 10 km/s with a thin-plate HVL at Sandia National Laboratories (SNL) [41]. The data clearly shows that Nextel/Kevlar intermediate bumpers provide protection advantages over an equivalent mass aluminum intermediate layer. Figure 4-9 provides ballistic limit curves and impact data for a specific stuffed Whipple shield design, namely one with an overall standoff of 10.7 cm, containing a 0.2 cm Al 6061-T6 bumper followed by a Nextel/Kevlar blanket consisting of six Nextel AF62 layers and six Kevlar 710 layers, and a 0.48 cm Al 2219-T87 rear wall.

Table 4-7. Stuffed Whipple and All-Aluminum Shield Impact Data [10]

Type	Shield AD (g/cm ²)	Spacing (cm)	Test No.	Proj. Dia. (cm)	Proj. Mass (g)	Velocity (km/s)	Impact angle (deg)	Rear Wall Damage
Nextel/Kevlar Stuffed Whipple Ballistic Limit Data								
SW-2	2.16	11.4	MSFC 1455	1.27	3.00	5.82	0	Perf: 1.6 cm
SW-3	1.78	7.6	SNL-HVL-6	0.73	0.56	10.10	45	No Perf
SW-4	2.67	11.4	JSC B654	1.00	1.46	6.84	0	No Perf, v.slight dish
SW-Lab	2.78	11.4	ARC2139	1.19	2.49	7.03	0	No Perf, bulge
SW-Lab	2.78	11.4	ARC2141	1.27	3.01	7.03	0	No Perf, 1.7 cm bulge
SW-Lab	2.78	11.4	JSC B890	0.95	1.27	2.94	0	No Perf, bump
SW-Lab	2.78	11.4	JSC B875	1.00	1.47	4.87	0	No Perf, no bulge
SW-Lab	2.78	11.4	ARC2140	1.19	2.49	7.07	45	No Perf, slight bulge
SW-Lab	2.78	11.4	ARC2127	1.59	5.87	5.2	60	No Perf, small craters
SW-cupola	2.21	17.78	JSC 20274	1.27	3.00	6.68	0	No Perf, deep bulge
SW-cupola	2.21	17.78	JSC 20310	1.27	3.00	6.82	45	No Perf, bulge
SW-ATV	1.37	12.7	JSC 20254	0.71	0.53	7.0	0	No Perf, slight bulge
Comparison tests between Nextel/Kevlar and all-Aluminum shields								
SW-1	1.75	7.6	JSC B305	0.95	1.26	6.70	45	No Perf, bulge 7 mm
All-Al-1	1.82	7.6	JSC B562	0.71	0.52	6.42	45	Perf: 4mm, cracks
All-Al-1	1.82	7.6	JSC B560	0.71	0.52	6.94	45	Perf, 15 mm cracks
All-Al-1	1.82	7.6	JSC B563	0.67	0.44	6.96	45	No Perf, bulge, BL
SW-2	2.16	11.4	JSC B536	1.00	1.46	6.85	15	No Perf, slight dish
SW-2	2.16	11.4	JSC B537	1.00	1.46	4.86	15	No Perf, crater
All-Al-2	2.66	11.4	JSC B535	0.95	1.26	6.64	15	Perf, 32 mm crack
SW-1	1.75	7.6	JSC B549	1.00	1.46	6.60	60	No Perf, bulge 6 mm
All-Al-3	1.73	7.6	JSC B520	0.75	0.62	6.99	60	Perf, 6x5 mm
SW-3	1.78	7.6	SwRI-ISCL-5993-10	0.85	0.87	11.18	0	No Perf, bulge, BL
All-Al-3	1.73	7.6	SwRI-ISCL-5993-12	0.84	0.84	11.03	0	Perf: 4.3 cm petalled hole
SW-3	1.78	7.6	SwRI-ISCL-5993-14	1.01	1.46	11.42	45	No Perf, bulge
All-Al-3	1.73	7.6	SwRI-ISCL-5993-13	0.92	1.11	11.32	45	Perf, large petalled hole
SW-3	1.78	7.6	SNL-HVL-5	0.74	0.56	10.0	0	No Perf
All-Al-3	1.78	7.6	SN-HVL-3	0.81	0.75	10.2	0	Perforated

Table 4-8. Shield Parameters for Stuffed Whipple and All-Aluminum Impact Tests

Type	Shield overall areal density (g/cm ²)	Spacing (cm)	Bumper thickness, t _b (cm)*	Inter-mediate areal density (g/cm ²)	Intermediate bumper description	Rear wall thickness, t _w (cm)	Rear wall material
<i>Nextel/Kevlar Stuffed Whipple Shields</i>							
SW-1	1.75	7.6	0.1	0.56	Mesh, 4 Nextel AF62, 4 Kevlar 710	0.32	Al 2219T87
SW-2	2.16	11.4	0.16	0.82	Mesh, 6 Nextel AF62, 6 Kevlar 710	0.48	Al 2219T87
SW-3	1.78	7.6	0.13	0.53	4 Nextel AF62, 4 Kevlar 710	0.32	Al 2219T87
SW-4	2.67	11.4	0.19	0.79	6 Nextel AF62, 6 Kevlar 710	0.48	Al 2219T87
SW-Lab	2.78	11.4	0.2	0.85	MLI, 6 Nextel AF62, 6 Kevlar 710	0.48	Al 2219T87
SW-cupola	2.21	17.8	0.2	0.97	3 Nextel AF62, 1.27 mm Al 6061T6, 14 Kevlar KM2 705	0.25	Al 6061T6
SW-ATV	1.37	12.7	0.13	0.12	2 Nextel AF10, 3 Kevlar KM2 705	0.32	Al 2219T87
<i>All-Aluminum Shields</i>							
All-Al-1	1.82	7.6	0.13	0.56	0.2 cm Al 2024T3	0.32	Al 2219T87
All-Al-2	2.66	11.4	0.19	0.91	0.32 cm Al 2219T87	0.48	Al 2219T87
All-Al-3	1.73	7.6	0.1	0.54	0.2 cm Al 6061T6	0.32	Al 2219T87

* Note, all bumpers are Al 6061-T6 alloy

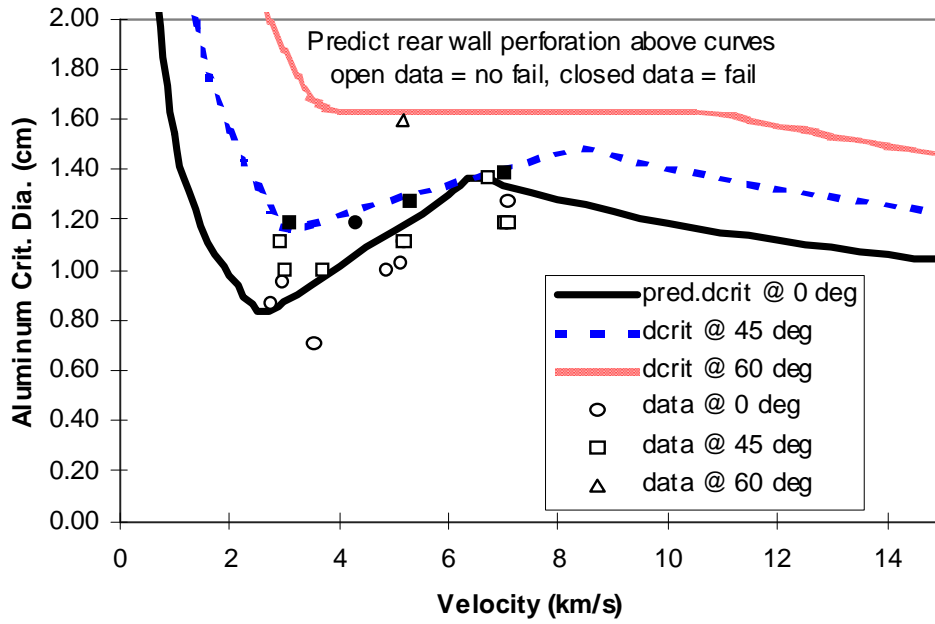


Figure 4-9. Stuffed Whipple ballistic limits. 0.2 cm Al 6061T6 bumper, 6 Nextel AF62 + 6 Kevlar 710 intermediate bumper, 10.7 cm overall standoff, 0.48 cm Al 2219T87 rear wall.

4.4 All-Aluminum Triple-Wall Shield

The all-aluminum triple-wall shield consists of two separate bumpers followed by a rear wall. The following equations are referred to as “ESA triple-wall” equations and are adapted from the NASA Whipple equations (Eq. 4-23 through 4-25) with ESA coefficients [48, p. 3-10]. The failure criteria are perforation or detached spall from the rear wall. The general form of the equation is given below. Note: this equation is applied to both high- and low-velocity regimes, with parameters defined in Tables 4-9 and 4-10.

$$d_c = \left[\frac{t_w + K_2 \cdot t_b^\mu \cdot \rho_b^{g2}}{K_1 \cdot \rho_p^\beta \cdot V^\gamma \cdot (\cos \theta)^\xi \cdot \rho_w^\kappa \cdot S^\delta \cdot \rho_b^{\nu 1}} \right]^{1/\lambda} \quad (4-51)$$

For impact velocities in the transition region; i.e., when impact velocity is between V_L and V_H , linear interpolation is used to calculate the ballistic limit, as follows:

$$d_c = d_{c, V_n = V_L} \cdot \left(\frac{V_H - V_n}{V_H - V_L} \right) + d_{c, V_n = V_H} \cdot \left(\frac{V_n - V_L}{V_H - V_L} \right) \quad (4-52)$$

Table 4-9. Triple-Wall Damage Equation Terms

Symbol	Unit	Description
t_w	cm	Thickness of rear wall
t_b	cm	Combined thickness of all bumpers
K_1, K_2	-	Equation specific characteristic factors
d_c	cm	Critical projectile diameter at shield failure threshold
ρ_p, ρ_b, ρ_w	g/cm ³	Density of projectile, bumper, rear wall
V	km/s	Impact velocity
V_n	km/s	Normal component impact velocity = $V \cos \theta$
V_L	km/s	Lower-velocity limit = 3 km/s
V_H	km/s	High-velocity limit = 7 km/s
θ	deg	Impact angle with respect to surface normal
S	cm	Space between outer bumper and rear wall
σ_w	ksi	Rear wall yield stress

Table 4-10. Parameter Values for the Triple-Wall BLE

Velocity Regime (km/s)	K_1	K_2	λ	β	γ	κ	δ, ξ	ν_1, ν_2, μ
$V_n < 3$	$0.312 (40/\sigma_w)^{0.5}$	$1.667 K_1$	1.056	0.5	2/3	0	0, 5/3	0, 0, 1
$V_n > 7$	$0.107 (70/\sigma_w)^{0.5}$	0	1.5	0.5	1	0	-0.5, 1	0.167, 0, 0

4.5 Multi-Shock Shields

MS shields are defined as a combination of four ceramic fabric bumpers followed by either an aluminum or Kevlar rear wall (figure 4-10). Ceramic bumpers produce higher shock pressures in the projectile than aluminum, which translates into better projectile breakup [10, 42, 43]. Fabric ceramic bumpers are more damage tolerant than monolithic (solid) ceramic layers which tend to disintegrate upon impact. Fabrics do not generate much (or any) secondary ejecta compared to conventional aluminum materials, and therefore greatly reduce any contribution to the orbital debris environment population when impacted. Thus, fabrics are more suitable for spacecraft shielding applications than solid bumpers.

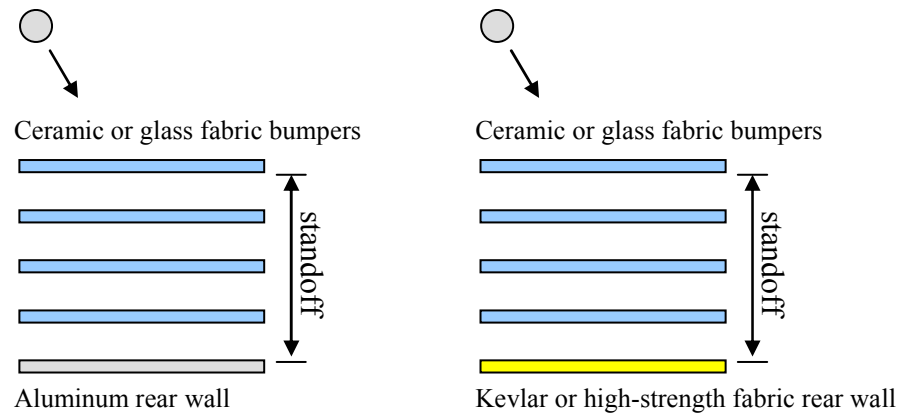


Figure 4-10. MS shield configurations.

Table 4-9 shows that MS shields are more effective than Whipple shields at protecting from HVIs. Multiple bumpers are more successful at MMOD protection because they provide greater breakup of hypervelocity projectiles than equivalent weight single bumpers. Multiple bumper shield systems are more efficient than single bumpers at converting projectile kinetic energy to internal energy within the projectile, which causes increased melting and vaporization of the projectile, thereby decreasing the size and number of solid particles impacting the rear wall. Multiple layer shields also decrease the expansion speed of the debris cloud, which decreases loading of the rear wall. These attributes contribute to the effectiveness of MS shields.

A ceramic fabric used in the MS shield is Nextel, although other ceramic fabrics or glass-fiber fabrics can be used with little to no adverse effect on shielding performance. The important parameter to control is the overall mass per unit area of the bumpers, in relation to the projectile mass per unit area that the shield is designed to stop, typically at the average impact velocity and angle conditions experienced on-orbit, or for a standard test condition of 7 km/s at impact angle of 0° (or normal to the shield).

Table 4-11. Comparison of Whipple, MS and Mesh Double-Bumper Shield Impact Data *Table provides the shield mass per unit area that resulted in no perforation or detached spall of rear wall (i.e., no failure) for the given projectile diameter and mass. All impact tests occurred at 6-7 km/s for Al 2017-T4 spherical projectiles of given diameter at the indicated impact angle.*

Overall Shield Spacing (cm)	Impact Angle (deg)	Whipple Shield	Multi-Shock Shield	Mesh Double-Bumper Shield
Shield Areal Density (g/cm ²) and [test number]				
0.32 cm (0.045 g) aluminum projectile				
5	0°	1.12 [JSC-A1464]	0.53 [JSC-A624]	0.41 [JSC-A963]
10	0°	0.60 [JSC-A235]	0.29 [JSC-A1231]	0.25 [JSC-A1285]
10	45°	1.50 [JSC-A1195]	0.31 [JSC-A1317]	0.36 [JSC-A1069]
0.64 cm (0.37 g) aluminum projectile				
10	0°	2.07 [JSC-B128]	1.10 [JSC-B112]	0.94 [JSC-B77]
20	0°	0.96 [JSC-B31]	0.63 [JSC-B70]	0.64 [JSC-B27]
0.95 cm (1.3 g) aluminum projectile				
30	0°	1.35 [ARC-1895]	1.02 [UDRI 4-1293]	1.08 [UDRI 4-1172]

4.5.1 Multi-Shock Shield Design Equations

The following equations are used to size MS shield elements for impacts with velocity greater than $6.4 \cos^{-0.25} \theta$ km/s and $S/d > 15$. In these equations, the combined areal density of all four bumpers is given by m_b , and the overall spacing from outermost bumper to the rear wall is given by S . The combined areal density for all bumpers is approximately equal to the areal density of the single bumper in a Whipple shield designed for the same impact conditions. The rear wall of the MS shield is significantly less than for the Whipple shield. Major weight savings can be obtained by reducing the rear wall thickness for stopping a given threat particle, especially when sufficient spacing is available ($S \geq 30d$). The areal density of all four bumpers in the MS shield is given by:

$$m_b = 0.185 \ d \ \rho_p \quad (4-53)$$

The thickness of an aluminum rear wall is determined by the following equation, where $k = 41.6$ s/km and normalized rear wall yield strength, $\sigma' = \sigma/40$ (unitless).

$$t_w = k \ M \ V_n \ \rho_w^{-1} \ S^{-2} \ \sigma'^{-0.5} \quad (4-54)$$

The mass per unit area of a Kevlar rear wall is determined by the following equation, where $K = 29$ s/km. Good shield performance is obtained using Kevlar KM2 (style 705 or 706), or Kevlar 29 (style 710 or FDI-120).⁵

$$m_w = K M V_n S^{-2} \quad (4-55)$$

Where

- d = projectile diameter (cm)
- k = coefficient = 41.6 (s/km)
- K = coefficient = 29 (s/km)
- m_b = bumper areal density (g/cm²)
- M = projectile mass (g)
- ρ_p = projectile density (g/cm³)
- ρ_w = rear wall density (g/cm³)
- S = overall spacing (gap distance) between outer bumper and rear wall (cm)
- σ = rear wall yield stress (ksi)
- σ' = normalized rear wall yield stress = $\sigma/40$ (unitless)
- t_w = rear wall thickness (cm)
- θ = impact angle from target normal (deg); note impact at $\theta = 0$ deg is normal to the target
- V = projectile velocity (km/s)
- V_n = normal component of projectile velocity (km/s) = $V \cos\theta$

4.5.2 Performance Equations for MS Shields with Aluminum Rear Wall

The following equations provide the impacting particle size at the failure threshold of an MS Shield with an aluminum rear wall. Failure is defined as a perforation or detached spall of the rear wall. It should be noted that rear wall perforation is the primary failure mode. Detached spall of the rear wall has not been observed in impact tests on MS shields.

High-velocity, $V \geq 6.4 (\cos\theta)^{-0.25}$:

$$d_c = K_{H-MS} (t_w \rho_w)^{1/3} \rho_p^{-1/3} (\sigma / 40)^{1/6} V^{-1/3} (\cos \theta)^{-1/3} S^{2/3} \quad (4-56)$$

Where

- d_c = critical projectile diameter at shield failure threshold (cm)
- $K_{H-MS} = 0.358 (\text{km}^{1/3} \text{s}^{-1/3})$

⁵ Kevlar™ is a product of the DuPont Company. Kevlar KM2 style 705 is a Hexcel Schwebel Company fabric style. Kevlar FDI-120 is a fabric style available from Fabric Development Incorporated.

ρ_p = projectile density (g/cm³)
 ρ_w = rear wall density (g/cm³)
 S = overall spacing (gap distance) between outer bumper and rear wall (cm)
 σ = rear wall 0.2% offset tensile yield stress (ksi) (note 1ksi=1000 lb_f/in² = 6.895 MPa)
 t_w = rear wall thickness (cm)
 θ = impact angle from target normal (deg); note impact at $\theta = 0$ deg is normal to the target
 V = projectile velocity (km/s)
 V_n = normal component of projectile velocity (km/s) = $V \cos\theta$

Low-velocity, $V \leq 2.4 (\cos\theta)^{-0.5}$:

$$d_c = K_{L-MS} V^{-2/3} (\cos\theta)^{-4/3} \rho_p^{-0.5} \left[t_w (\sigma / 40)^{0.5} + C_L m_b \right] \quad (4-57)$$

Where

C_L = low velocity coefficient = 0.37 (cm³/g)
 d_c = critical projectile diameter at shield failure threshold (cm)
 $K_{L-MS} = 2.0 (g^{0.5} km^{2/3} cm^{-3/2} s^{-2/3})$
 m_b = total bumper areal density and is the sum of the areal densities of all four bumpers (g/cm²)
 ρ_p = projectile density (g/cm³)
 σ = rear wall yield stress (ksi)
 t_w = rear wall thickness (cm)
 θ = impact angle from target normal (deg); note impact at $\theta = 0$ deg is normal to the target
 V = projectile velocity (km/s)
 V_n = normal component of projectile velocity (km/s) = $V \cos\theta$

Intermediate-velocity, $2.4 (\cos\theta)^{-0.5} < V < 6.4 (\cos\theta)^{-0.25}$:

$$d_c = \left[\frac{K_{Li-MS} \left[t_w (\sigma / 40)^{0.5} + C_L m_b \right]}{(\cos\theta) \rho_p^{0.5}} \right] \times \left[\frac{6.4 \cos^{-0.25} \theta - V}{6.4 \cos^{-0.25} \theta - 2.4 \cos^{-0.5} \theta} \right] + \left[K_{Hi-MS} (t_w \rho_w)^{1/3} \rho_p^{-1/3} (\cos\theta)^{-0.25} S^{2/3} (\sigma / 40)^{1/6} \right] \times \left[\frac{V - 2.4 \cos^{-0.5} \theta}{6.4 \cos^{-0.25} \theta - 2.4 \cos^{-0.5} \theta} \right] \quad (4-58)$$

Where

C_L = low velocity coefficient = 0.37 (cm³/g)

d_c = critical projectile diameter at shield failure threshold (cm)
 ρ_b = bumper density (g/cm³)
 ρ_p = projectile density (g/cm³)
 ρ_w = rear wall density (g/cm³)
 $K_{Hi-MS} = 0.193$
 $K_{Li-MS} = 1.12 \text{ (g}^{0.5} \text{ cm}^{-3/2} \text{)}$
 m_b = total bumper areal density and is the sum of the areal densities of all four bumpers (g/cm²)
 S = overall spacing (gap distance) between outer bumper and rear wall (cm)
 σ = rear wall yield stress (ksi)
 t_w = rear wall thickness (cm)
 θ = impact angle from target normal (deg); note impact at $\theta = 0$ deg is normal to the target
 V = projectile velocity (km/s)
 V_n = normal component of projectile velocity (km/s) = $V \cos\theta$

No limits are necessary on oblique impacts because the ceramic bumpers do not produce damaging fragments. Ceramic fabric debris from the bumpers consist of short fibers up to a few millimeters long which are ejected in a normal direction toward subsequent bumpers and rear wall, but are not very damaging and do not penetrate lower-level shield layers. Figure 4-11 provides the expected performance of an MS shield using the above equations with an aluminum rear wall, 0.31 g/cm² total areal density, and 10 cm overall standoff.

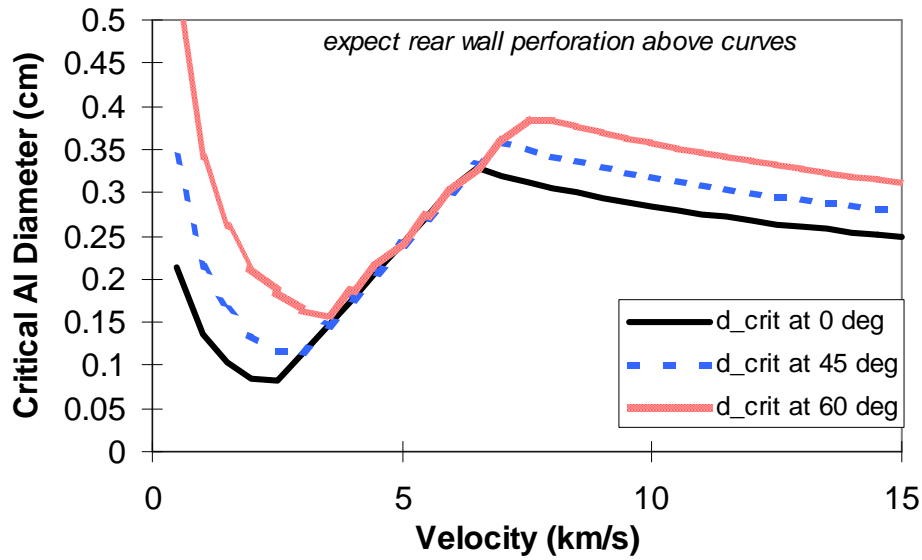


Figure 4-11. MS shield ballistic limit curves. MS consists of four Nextel AF26 bumpers (0.043 g/cm² each), 0.051 cm Al 2024T3 rear wall, 2.54 cm gap between bumpers, 10.2 cm overall spacing.

4.5.3 Performance Equations for MS Shields with Kevlar Rear Wall

The following equations provide the impacting particle size at the failure threshold of an MS Shield with a Kevlar rear wall. Failure is defined as a perforation of the rear wall. Kevlar KM2 (style 705 or 706) or Kevlar 29 style 710 can be used as rear wall materials.

High-velocity, $V \geq 6.4 (\cos\theta)^{-0.25}$:

$$d_c = K_{H-MS} m_w^{1/3} \rho_p^{-1/3} V^{-1/3} (\cos \theta)^{-1/3} S^{2/3} \quad (4-59)$$

Where

d_c = critical projectile diameter at shield failure threshold (cm)

$K_{H-MS} = 0.41 (\text{km}^{1/3} \text{s}^{-1/3})$

m_w = areal density of rear wall (g/cm²)

ρ_p = projectile density (g/cm³)

S = overall spacing (gap distance) between outer bumper and rear wall (cm)

θ = impact angle from target normal (deg); note impact at $\theta = 0$ deg is normal to the target

V = projectile velocity (km/s)

V_n = normal component of projectile velocity (km/s) = $V \cos\theta$

Low-velocity, $V \leq 2.4 (\cos\theta)^{-0.5}$:

$$d_c = K_{L-MS} V^{-2/3} (\cos \theta)^{-4/3} \rho_p^{-0.5} [C_w m_w + C_L m_b] \quad (4-60)$$

Where

C_L = low velocity coefficient = 0.37 (cm³/g)

C_W = rear wall coefficient = 0.5 (cm³/g)

d_c = critical projectile diameter at shield failure threshold (cm)

$K_{L-MS} = 2.7 (g^{0.5} km^{2/3} cm^{-3/2} s^{-2/3})$

m_b = total bumper areal density and is the sum of the areal densities of all four bumpers (g/cm²)

m_w = rear wall areal density (g/cm²)

ρ_p = projectile density (g/cm³)

θ = impact angle from target normal (deg); note impact at $\theta = 0$ deg is normal to the target

V = projectile velocity (km/s)

V_n = normal component of projectile velocity (km/s) = $V \cos \theta$

Intermediate-velocity, $2.4 (\cos \theta)^{-0.5} < V < 6.4 (\cos \theta)^{-0.25}$:

$$d_c = \left[\frac{K_{Li-MS} [C_w m_w + C_L m_b]}{(\cos \theta) \rho_p^{0.5}} \right] \times \left[\frac{6.4 \cos^{-0.25} \theta - V}{6.4 \cos^{-0.25} \theta - 2.4 \cos^{-0.5} \theta} \right] + \left[K_{Hi-MS} m_w^{1/3} \rho_p^{-1/3} (\cos \theta)^{-0.25} S^{2/3} \right] \times \left[\frac{V - 2.4 \cos^{-0.5} \theta}{6.4 \cos^{-0.25} \theta - 2.4 \cos^{-0.5} \theta} \right] \quad (4-61)$$

Where

C_L = low velocity coefficient = 0.37 (cm³/g)

C_W = rear wall coefficient = 0.5 (cm³/g)

d_c = critical projectile diameter at shield failure threshold (cm)

ρ_b = bumper density (g/cm³)

ρ_p = projectile density (g/cm³)

ρ_w = rear wall density (g/cm³)

$K_{Hi-MS} = 0.221$

$K_{Li-MS} = 1.506 (g^{0.5} cm^{-3/2})$

m_b = total bumper areal density and is the sum of the areal densities of all four bumpers (g/cm²)

m_w = rear wall areal density (g/cm²)

S = overall spacing (gap distance) between outer bumper and rear wall (cm)

θ = impact angle from target normal (deg); note impact at $\theta = 0$ deg is normal to the target

V = projectile velocity (km/s)

V_n = normal component of projectile velocity (km/s) = $V \cos\theta$

4.6 Hybrid MS Shield

Hybrid MS shields are defined as a combination of multiple ceramic fabric and aluminum layers; specifically, two separate layers of ceramic fabric followed by two separate aluminum layers. Hybrid MS shields are considered for applications where the protection capability of Whipple shields is improved in a relatively uncomplicated way by adding two Nextel ceramic fabric layers over an aluminum two-sheet Whipple shield (figure 4-12). The two outer Nextel bumpers and the aluminum bumper are all equally spaced from each other. The spacing between the aluminum bumper and aluminum rear wall is twice the inter-bumper spacing. Both Nextel bumpers together contain approximately the same areal density as the aluminum bumper, while the rear wall is approximately twice the areal density of the aluminum bumper. HVI testing to derive the hybrid MS shield BLEs below focused on two types of shields:

- (1) A 20 cm overall standoff (1.05 g/cm²) hybrid shield with two Nextel BF54 bumpers (0.108 g/cm² each), a 0.1 cm Al 6061-T6 bumper, and a 0.18 cm Al 6061-T6 rear wall.
- (2) A 7.6 cm overall standoff (0.42 g/cm²) hybrid shield with two Nextel AF26 bumpers (0.043 g/cm² each), a 0.041 cm Al 6061-T6 bumper, and a 0.081 cm Al 6061-T6 rear wall. This shield was a 40% scale model of the shield described in item 1 above.

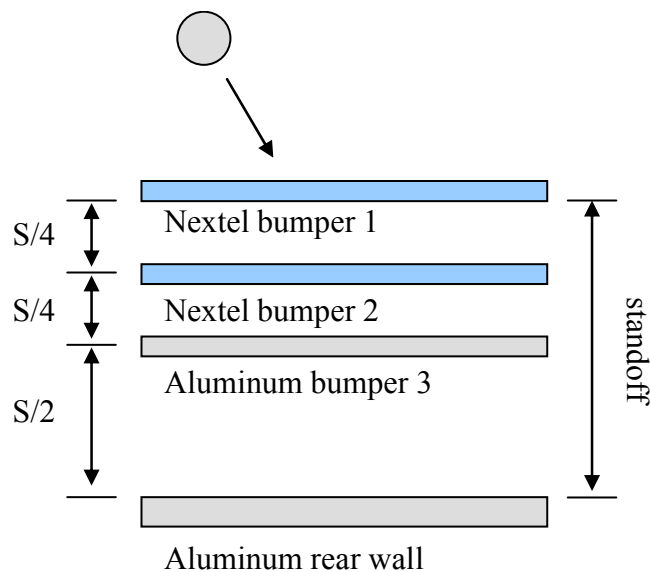


Figure 4-12. Hybrid Nextel/Aluminum MS shield.

BLEs for the hybrid shield are given below based on analysis of about 50 HVI tests conducted by NASA on hybrid shields.

High-velocity, $V \geq 6.5 (\cos\theta)^{-2/3}$:

$$d_c = 2.15 m_w^{2/3} \rho_p^{-1/3} V^{-2/3} (\cos \theta)^{-2/3} S^{1/3} (\sigma / 40)^{1/3} \quad (4-62)$$

Where

d_c = critical projectile diameter at shield failure threshold (cm)

m_w = areal density of rear wall (g/cm^2) = $t_w \rho_w$

ρ_p = projectile density (g/cm^3)

ρ_w = rear wall density (g/cm^3)

S = overall spacing (gap distance) between outer bumper and rear wall (cm)

σ = rear wall yield stress (ksi)

t_w = rear wall thickness (cm)

θ = impact angle from target normal (deg); note impact at $\theta = 0$ deg is normal to the target

V = projectile velocity (km/s)

V_n = normal component of projectile velocity (km/s) = $V \cos\theta$

Low-velocity, $V \leq 2.7 (\cos\theta)^{-0.5}$:

$$d_c = 2 V^{-2/3} (\cos \theta)^{-x} \rho_p^{-0.5} \left[t_w (\sigma / 40)^{0.5} + C_L m_b \right] \quad (4-63)$$

Where

C_L = low velocity coefficient = $0.37 (\text{cm}^3/\text{g})$

d_c = critical projectile diameter at shield failure threshold (cm)

m_b = total bumper areal density and is the sum of the areal densities of all three bumpers (g/cm^2)

ρ_p = projectile density (g/cm^3)

θ = impact angle from target normal (deg); note impact at $\theta = 0$ deg is normal to the target

V = projectile velocity (km/s)

V_n = normal component of projectile velocity (km/s) = $V \cos\theta$

$x = 7/3$ when $\theta \leq 45^\circ$, $x = 2$ when $\theta > 45^\circ$

Intermediate-velocity, $2.7 (\cos\theta)^{-0.5} < V < 6.5 (\cos\theta)^{-(2/3)}$:

$$d_c = \left[\frac{1.031 [t_w (\sigma / 40)^{0.5} + C_L m_b]}{(\cos\theta)^{x-1/3} \rho_p^{0.5}} \right] \times \left[\frac{6.5 \cos^{-(2/3)} \theta - V}{6.5 \cos^{-(2/3)} \theta - 2.7 \cos^{-0.5} \theta} \right] + \left[0.617 m_w^{2/3} \rho_p^{-1/3} (\cos\theta)^{-(2/9)} S^{1/3} (\sigma / 40)^{1/3} \right] \times \left[\frac{V - 2.7 \cos^{-0.5} \theta}{6.5 \cos^{-(2/3)} \theta - 2.7 \cos^{-0.5} \theta} \right] \quad (4-64)$$

Where

C_L = low velocity coefficient = 0.37 (cm³/g)

d_c = critical projectile diameter at shield failure threshold (cm)

m_b = total bumper areal density and is the sum of the areal densities of all three bumpers (g/cm²)

m_w = areal density of rear wall (g/cm²) = $t_w \rho_w$

ρ_p = projectile density (g/cm³)

ρ_w = rear wall density (g/cm³)

ρ_p = projectile density (g/cm³)

S = overall spacing (gap distance) between outer bumper and rear wall (cm)

σ = rear wall yield stress (ksi)

t_w = rear wall thickness (cm)

θ = impact angle from target normal (deg); note impact at $\theta = 0$ deg is normal to the target

V = projectile velocity (km/s)

V_n = normal component of projectile velocity (km/s) = $V \cos\theta$

$x = 7/3$ when $\theta \leq 45^\circ$, $x = 2$ when $\theta > 45^\circ$

For oblique impact angles over 75° , use the critical diameter calculated at 75° ; that is, for $\theta > 75^\circ$: $d_c = d_c (\theta=75^\circ)$.

4.7 Mesh Double-Bumper Shield

The mesh double-bumper (MDB) shield comprises four components (figure 4-13): (1) a mesh bumper; (2) a continuous bumper; (3) a high-strength fabric intermediate layer; and (4) a rear wall. The mesh provides an efficient method to breakup projectiles. It can be placed a short distance in front of the continuous bumper as shown in figure 4-13, or directly on or under the continuous bumper. Due to the overlap of the wires, it provides the same breakup capability as a thicker continuous bumper. HVI tests demonstrated that the spread angle of the debris cloud after impact on a wire mesh is greater than an equivalent areal density solid aluminum bumper [45, 46]. Bumper fragments from mesh bumpers are smaller and less damaging to the rear wall due to the small wire diameter.

The multiple shocks created by the mesh and continuous bumper increases disruption as well as the thermal state of the projectile, compared to a Whipple shield. This is evident from experimental results, where far more melt was present on the rear wall from mesh double-bumper tests compared to conventional Whipple or three-metallic plate shield tests, and was also evident in computational studies [33, 45]. From analytical studies [10], the Kevlar or Spectra high-strength fabrics used in the intermediate layer slow and defeat fragments in the debris cloud, and reduce the expansion speed of the debris cloud. These high-strength, low-density materials work well lower down in the shield, near the rear wall. However, these materials are not effective as an outer bumper because they have poor projectile breakup characteristics, particularly when exposed to impact by glass, aluminum, and higher-density projectiles.

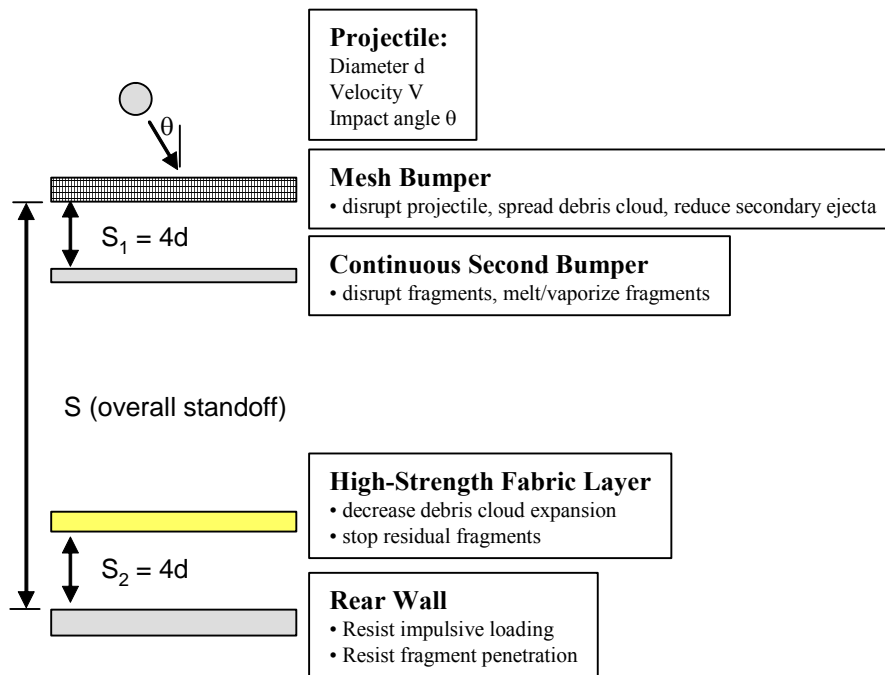


Figure 4-13. MDB shield.

4.7.1 MDB Shield Design Equations

The following equations are used to size the thickness and mass per unit area of the MDB shield elements given in figure 4-13. These equations are applied when the impact velocity component ($V \cos^{1/3} \theta$) is greater than 6.4 km/s. Generally, the particle diameter, d (cm), which the shield is designed to stop at average impact conditions is used to size the shields.

The mesh areal density is given by:

$$m_{\text{mesh}} = 0.04 d \rho_p \quad (4-65)$$

The mesh has wires in a square pattern with a wire diameter to projectile diameter ratio of from 0.07 to 0.10. As an example, the mesh used in some of the screening tests using a 0.32-cm-diameter aluminum projectile [46] consisted of 0.3-mm-diameter aluminum 5056 wires in a square pattern, 0.051 g/cm² areal density, with 30 by 30 wires every 2.5 cm by 2.5 cm, and a 0.56 mm gap between wires. Aluminum and steel mesh bumpers have been used with good success. Steel mesh is used to improve the capability of ISS module shields, such as on the FGB module “Zarya” [47].

The first to second bumper spacing is four times the projectile diameter: $S_1 = 4d$. The continuous aluminum bumper is sized by the following equation.

$$m_{\text{Al_bumper}} = 0.093 d \rho_p \quad (4-66)$$

A high-strength fabric intermediate layer, for example Kevlar KM2 or Spectra fabric, is mounted a distance $S_2 = 4d$ in front of the rear wall. For the Kevlar or Spectra intermediate bumper, the areal density is determined using the following equation.

$$m_{\text{Kevlar}} = 0.064 d \rho_p \quad (4-67)$$

If Nextel cloth is used for the intermediate layer, the areal density is:

$$m_{\text{Nextel}} = 0.095 d \rho_p \quad (4-68)$$

The rear wall areal density to prevent perforation and detached spall is determined by:

$$m_w = C_w M V_n S^{-3/2} \sigma'^{-0.5} \quad (4-69)$$

Where

C_w = coefficient = 9 (cm^{-1/2} km⁻¹ s)

d = projectile diameter (cm)

$m_{\text{Al_bumper}}$ = continuous aluminum bumper areal density (g/cm²)

m_{Kevlar} = Kevlar areal density (g/cm²)

m_{mesh} = mesh areal density (g/cm²)

m_{Nextel} = Nextel areal density (g/cm^2)
 m_w = rear wall areal density (g/cm^2)
 M = projectile mass (g)
 ρ_p = projectile density (g/cm^3)
 S = overall spacing (gap distance) between outer bumper and rear wall (cm)
 σ = rear wall yield stress (ksi)
 σ' = normalized rear wall yield stress = $\sigma/40$ (unitless)
 θ = impact angle from target normal (deg); note impact at $\theta = 0$ deg is normal to the target
 V = projectile velocity (km/s)
 V_n = normal component of projectile velocity (km/s) = $V \cos\theta$

4.7.2 MDB Shield Performance Equations

The following equations provide the impacting particle size at the failure threshold of a MDB shield. Failure is defined as a perforation or detached spall of the rear wall.

High-velocity, $V \geq 6.4 (\cos\theta)^{-1/3}$:

$$d_c = 0.6 (t_w \rho_w)^{1/3} \rho_p^{-1/3} (\sigma / 40)^{1/6} V^{-1/3} (\cos \theta)^{-1/3} S^{1/2} \quad (4-70)$$

Where

d_c = critical projectile diameter at shield failure threshold (cm)
 ρ_p = projectile density (g/cm^3)
 ρ_w = rear wall density (g/cm^3)
 S = overall spacing (gap distance) between outer bumper and rear wall (cm)
 σ = rear wall 0.2% offset tensile yield stress (ksi) (note 1ksi=1000 lb_f/in² = 6.895 MPa)
 t_w = rear wall thickness (cm)
 θ = impact angle from target normal (deg); note impact at $\theta = 0$ deg is normal to the target
 V = projectile velocity (km/s)
 V_n = normal component of projectile velocity (km/s) = $V \cos\theta$

Low-velocity, $V \leq 2.8 (\cos\theta)^{-0.5}$:

$$d_c = 2.2 V^{-2/3} (\cos \theta)^{-5/3} \rho_p^{-0.5} \left[t_w (\sigma / 40)^{0.5} + C_L (m_b + m_k) \right] \quad (4-71)$$

Where

C_L = low velocity coefficient = 0.37 (cm³/g)
 d_c = critical projectile diameter at shield failure threshold (cm)
 m_b = total bumper areal density and is the sum of the areal densities the mesh and continuous aluminum bumper = $m_1 + m_2$ (g/cm²)
 m_K = intermediate bumper (Kevlar or Spectra) areal density (g/cm²)
 ρ_p = projectile density (g/cm³)
 σ = rear wall yield stress (ksi)
 t_w = rear wall thickness (cm)
 θ = impact angle from target normal (deg); note impact at $\theta = 0$ deg is normal to the target
 V = projectile velocity (km/s)
 V_n = normal component of projectile velocity (km/s) = $V \cos\theta$

Intermediate-velocity, $2.8 (\cos\theta)^{-0.5} < V < 6.4 (\cos\theta)^{-1/3}$:

$$\begin{aligned}
 d_c = & \left[\frac{1.11 \left[t_w (\sigma / 40)^{0.5} + C_L (m_b + m_K) \right]}{(\cos \theta)^{4/3} \rho_p^{0.5}} \right] \times \left[\frac{6.4 \cos^{-1/3} \theta - V}{6.4 \cos^{-1/3} \theta - 2.8 \cos^{-0.5} \theta} \right] \\
 & + \left[0.323 (t_w \rho_w)^{1/3} \rho_p^{-1/3} (\cos \theta)^{-2/9} S^{1/2} (\sigma / 40)^{1/6} \right] \times \left[\frac{V - 2.8 \cos^{-0.5} \theta}{6.4 \cos^{-1/3} \theta - 2.8 \cos^{-0.5} \theta} \right] \quad (4-72)
 \end{aligned}$$

Where

C_L = low velocity coefficient = 0.37 (cm³/g)
 d_c = critical projectile diameter at shield failure threshold (cm)
 ρ_p = projectile density (g/cm³)
 ρ_w = rear wall density (g/cm³)
 m_b = total bumper areal density and is the sum of the areal densities the mesh and continuous aluminum bumper = $m_1 + m_2$ (g/cm²)
 m_K = intermediate bumper (Kevlar or Spectra) areal density (g/cm²)
 S = overall spacing (gap distance) between outer bumper and rear wall (cm)
 σ = rear wall yield stress (ksi)
 t_w = rear wall thickness (cm)
 θ = impact angle from target normal (deg); note impact at $\theta = 0$ deg is normal to the target
 V = projectile velocity (km/s)
 V_n = normal component of projectile velocity (km/s) = $V \cos\theta$

No limits are necessary on oblique impacts because the Kevlar/Spectra intermediate blanket provides protection to the rear wall from damaging bumper fragments.

5 Equations for Predicting Protection Limits of Thermal Protection System Materials

A number of spacecraft are capable of returning crew and/or cargo to Earth, including the Space Shuttle Orbiter vehicle, the planned Orion Crew Exploration Vehicle, several return vehicles designed for use on Space Station, and science-related experiment return capsules. Various types of TPS materials cover these spacecraft to protect them during return to Earth and the heating associated with atmospheric entry. Penetration and BLEs are required to predict the expected damage from hypervelocity MMOD particles and quantify associated risk. This section provides penetration equations for high-temperature TPS materials including ceramic tiles, RCC, and ablators. Results from HVI tests were used in the derivation of these equations, details of which are reported elsewhere [49-52].

5.1 TPS Failure Criteria

MMOD risk assessments for reentry vehicles rely on TPS failure criteria defined by technical assessments of TPS allowable damage extent. These assessments generally include: (a) evaluation of thermal conditions within the damaged TPS and underlying substructure; (b) determination of whether TPS damage will grow during reentry; and (c) evaluation of whether the substructure, internal components, and the overall vehicle will survive the elevated temperatures and thermal/structural loading during reentry. Depending on the local heating environment and type of TPS, superficial TPS damage could lead to LOV during reentry (i.e., damage that only penetrates part way through the TPS). Greater levels of TPS damage are generally allowed where heating is lower during reentry.

TPS damage detection and repair can improve reentry survivability. If critical TPS damage is found and mitigated prior to reentry, then the failure criteria for LOV generally shifts from TPS damage to substructure penetration or internal component damage (i.e., the new failure criteria can become damage to internal components that is an immediate hazard for survivability on-orbit, or to damage that cannot be mitigated via repair).

There is a need, therefore, for BLEs that predict MMOD damage extent to TPS, to TPS/substructure, and to internal components behind the TPS/substructure. These BLEs define projectile size at the threshold of the maximum allowable damage to the TPS.

5.2 Low-Density Ceramic Tile Penetration Equations

Penetration equations are reported below for low-density tiles: (1) LI-900 and LI-2200 tile (without Toughened Unipiece Fibrous Insulation [TUF] coating); and (2) TUF coated Alumina Enhanced Thermal Barrier (AETB-8) tile. These equations are valid for impact damage that extends down to, but not past the bondline between the tile and strain isolation pad (SIP).

5.2.1 LI-900 and LI-2200 Tile Penetration Equations

Penetration data from tests on two typical ceramic tiles used on Shuttle were regressed to develop a penetration equation into the tile (Equation 4-1): standard low-

density (LI-900) and high-density (LI-2200) tiles [49, 50]. The nominal bulk density of LI-900 material is 0.14 g/cm³ whereas LI-2200 nominal density is 0.35 g/cm³. The tiles are composed of compacted 1.5-micron-diameter, 99.6% pure, silica fibers fused with colloidal silica during a high-temperature sintering process. LI-2200 contains an additional 2% by weight dispersed silicon-carbide particles. The tiles have a borosilicate glass coating on top and sides, 0.2 mm to 0.38 mm thick with a 2.4 g/cm³ density.

The tiles were bonded to an aluminum substrate. The penetration equations are not valid for tiles without a backing, which would be subject to spall on the backside of the tile. HVI tests were conducted on LI-900 and LI-2200 tiles bonded with RTV adhesive to a 0.4-cm-thick (0.18 g/cm²) Nomex felt SIP, which is itself bonded with RTV adhesive to an aluminum plate or aluminum honeycomb panel that simulates the vehicle substrate. At the bondline with the SIP, the tiles have been densified by application of a ceramic slurry to the bottom which fills voids between fibers and provides a strengthened bonding surface for the SIP. The densification adds approximately 0.15 g/cm² and provides a 0.5-mm-thick layer that is hard and strong. The density gradually decreases toward the interior of the tile with most of the densified material remaining within 2.5 mm from the bonding surface.

An equation relating penetration depth in the tile to projectile parameters is as follows:

$$P = 1.27 d \left(\rho_p / \rho_t \right)^{0.5} (V \cos \theta)^{2/3} \quad [R^2 = 0.98] \quad (5-1)$$

Rearranging this equation:

$$d_c = 0.79 P_c \left(\rho_p / \rho_t \right)^{-0.5} (V \cos \theta)^{-2/3} \quad (5-2)$$

Where

d = projectile diameter (cm)

d_c = critical projectile diameter at threshold of critical penetration depth (cm)

P = penetration depth into tile (cm)

P_c = critical penetration depth at failure threshold (cm)

ρ_p = projectile density (g/cm³)

ρ_t = target density (g/cm³)

θ = impact angle from target normal (deg); note impact at θ = 0 deg is normal to the target

V = projectile velocity (km/s)

V_n = normal component of projectile velocity (km/s) = V cos θ

Other equations are given below for entry hole diameter in the tile (D_h), surface coating spall diameter (D_s), and maximum cavity diameter (D_c).

$$D_h = 2.4 d V^{2/3} (1 + 0.45 \sin \theta)^{2/3} \quad (5-3)$$

$$D_s = 2.98 d V^{2/3} (0.78 + \sin \theta)^{2/3} \quad (5-4)$$

$$D_c = 1.85 d \rho_p^{1/3} V^{2/3} (1 + 0.25 \sin \theta)^{2/3} \quad (5-5)$$

Where

d = projectile diameter (cm)

D_h = Entry hole diameter for crater in tile, excluding any coating spall present (cm). Note, for elliptical holes, D_h is the equivalent circular hole diameter with equivalent area as the elliptical entry hole, $D_h = (D_{\max} * D_{\min})^{0.5}$

D_s = Diameter of surface coating spall; i.e., the area where the borosilicate glass coating is removed (cm)

D_c = Maximum diameter of crater (cm)

ρ_p = projectile density (g/cm^3)

θ = impact angle from target normal (deg); note impact at $\theta = 0$ deg is normal to the target

V = projectile velocity (km/s)

5.2.2 TUF-coated AETB-8 Tile Penetration Equations

AETB-8 tiles with TUF coating were developed at the NASA Ames Research Center as an improvement to the LI-900 tile. The TUF coating is similar to the densification at the bondline, adding mass and strength at the surface of the tile. This results in a tile that is more durable and exhibits less surface damage when impacted compared to LI-900. A borosilicate glass coating covers the AETB-8/TUF tile, but this coating does not spall around the impact point as it often does with LI-900. The AETB tiles demonstrate higher strength, added durability, and similar maximum operational temperature as LI-900. The following penetration equation is valid for an AETB-8 tile bonded to SIP and substructure. The AETB-8 tiles have a nominal density of 8 lb/ft^3 (0.13 g/cm^3), but the TUF coating and densification at the bondline nearly double the overall density of the tile for typical tile thickness (i.e., to 0.24 g/cm^3 for a 3.2 cm thick tile).

An equation relating penetration depth in the AETB-8 tile to projectile parameters is as follows:

$$P = 1.177 d \left(\rho_p / \rho_t \right)^{0.5} (V \cos \theta)^{2/3} \quad (5-6)$$

Rearranging this equation:

$$d_c = 0.85 P_c \left(\rho_p / \rho_t \right)^{-0.5} (V \cos \theta)^{-2/3} \quad (5-7)$$

Where

d = projectile diameter (cm)

d_c = critical projectile diameter at threshold of critical penetration depth (cm)

P = penetration depth into tile (cm)

P_c = critical penetration depth at failure threshold (cm)

ρ_p = projectile density (g/cm³)

ρ_t = target density (g/cm³) = 0.24 g/cm³ for TUF1 coated AETB-8

θ = impact angle from target normal (deg); note impact at θ = 0 deg is normal to the target

V = projectile velocity (km/s)

5.3 Tile and Aluminum Substructure Penetration Equations

General BLEs were developed to predict the critical particle diameter resulting in threshold perforation of a TPS tile and substructure. The targets consist of typically LI-900 or LI-2200 tile bonded to SIP and to aluminum substructures. Both aluminum plate and aluminum honeycomb substructures are considered. Failure is defined as any hole or through-crack in the substructure, whether aluminum plate or in the second facesheet of the honeycomb panel, represented by TPS-5 damage mode and higher in figure 5-1. Additional details on the HVI data and techniques used to derive the equations are given in reference [49].

High-velocity, V_n ≥ 7 km/s:

$$d_c = 3 \left(t_T + 0.5 t_{HC} \right)^{1/3} t_{w+SIP}^{2/3} \rho_p^{-1/3} (\sigma / 70)^{1/3} (V \cos \theta)^{-2/3} \quad (5-8)$$

Where

d_c = critical projectile diameter at failure threshold of the tile and substrate (cm)

ρ_p = projectile density (g/cm³)

σ = substructure 0.2% offset tensile yield stress (ksi) (note 1ksi=1000 lb_f/in² = 6.895 MPa)

t_T = tile thickness (cm)

t_{HC} = overall honeycomb panel thickness (cm)
 t_w = substructure wall thickness (cm) = either the aluminum plate thickness or the sum of both honeycomb facesheet thickness for honeycomb panel substrates
 t_{w+SIP} = combined substructure wall and equivalent SIP thickness (cm)
 θ = impact angle from target normal (deg); note impact at $\theta = 0$ deg is normal to the target
 V = projectile velocity (km/s)
 V_n = normal component of projectile velocity (km/s) = $V \cos\theta$

Low-velocity, $V_n \leq 2.5$ km/s:

$$d_c = 1.82 V^{-2/3} (\cos \theta)^{-5/3} \rho_p^{-0.5} \left[t_w (\sigma / 70)^{0.5} + t_T (\rho_T / \rho_{Al})^{0.5} \right] \quad (5-9)$$

Where

d_c = critical projectile diameter at failure threshold of the tile and substrate (cm)

ρ_p = projectile density (g/cm³)

ρ_T = tile density (g/cm³)

ρ_{Al} = aluminum density (g/cm³) = 2.8 g/cm³

σ = substructure wall 0.2% offset tensile yield stress (ksi) (note 1ksi=1000 lb_f/in² = 6.895 MPa)

t_T = tile thickness (cm)

t_{HC} = overall honeycomb panel thickness (cm)

t_w = substructure wall thickness (cm) = either the aluminum plate thickness or the sum of both honeycomb facesheet thickness for honeycomb panel substrates

t_{w+SIP} = combined substructure wall and equivalent SIP thickness (cm)

θ = impact angle from target normal (deg); note impact at $\theta = 0$ deg is normal to the target

V = projectile velocity (km/s)

V_n = normal component of projectile velocity (km/s) = $V \cos\theta$

Intermediate-velocity, 2.5 km/s $< V_n < 7$ km/s :

$$d_c = \left[\frac{t_w (\sigma / 70)^{0.5} + t_T (\rho_T / \rho_{Al})^{0.5}}{1.01 (\cos \theta) \rho_p^{0.5}} \right] \times \left[\frac{7.0 - V \cos \theta}{4.5} \right] + \left[0.82 (t_T + 0.5 t_{HC})^{1/3} t_{w+SIP}^{2/3} \rho_p^{-1/3} (\sigma / 70)^{1/3} \right] \times \left[\frac{V \cos \theta - 2.5}{4.5} \right] \quad (5-10)$$

The equivalent thickness of the substrate wall and SIP, t_{w-SIP} (cm), is given by:

$$t_{w+SIP} = t_w + t_{SIP} (equivalent) = t_w + m_{SIP} / \rho_{Al} \quad (5-11)$$

Where

d_c = critical projectile diameter at failure threshold of the tile and substrate (cm)

ρ_p = projectile density (g/cm³)

ρ_T = tile density (g/cm³)

ρ_{Al} = aluminum density (g/cm³) = 2.8 g/cm³

m_{SIP} = SIP areal density (g/cm²) = 0.18 g/cm²

σ = substructure wall 0.2% offset tensile yield stress (ksi) (note 1ksi=1000 lb_f/in² = 6.895 MPa)

t_T = tile thickness (cm)

t_{HC} = overall honeycomb panel thickness (cm)

t_w = substructure wall thickness (cm) = either the aluminum plate thickness or the sum of both honeycomb facesheet thickness for honeycomb panel substrates

t_{w+SIP} = combined substructure wall and equivalent SIP thickness (cm)

θ = impact angle from target normal (deg); note impact at $\theta = 0$ deg is normal to the target

V = projectile velocity (km/s)

V_n = normal component of projectile velocity (km/s) = $V \cos\theta$

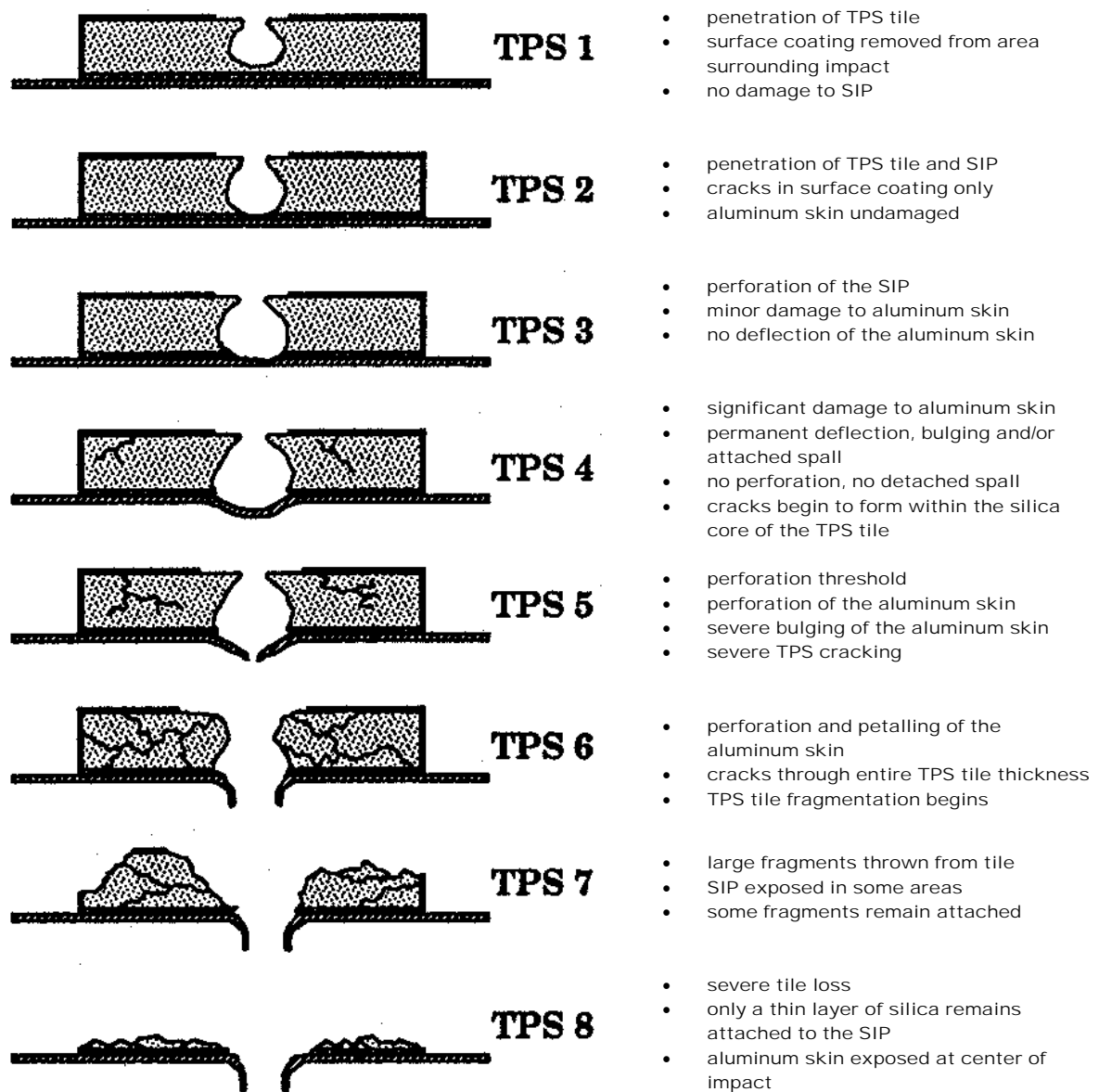


Figure 5-1. Hypervelocity damage modes for TPS tiles.

5.4 Tile and Composite Honeycomb Substructure Penetration Equations

The following equations define the critical particle size causing threshold perforation of a 5.1-cm-thick TUFI-coated AETB-8 tile bonded to 0.4-cm-thick SIP and to a graphite-cyanate composite honeycomb panel. More details of the target and HVI test results are found in reference [53]. The graphite composite honeycomb sandwich has 0.2-cm-thick graphite-cyanate composite facesheets, and has an overall thickness of 3.8 cm including the honeycomb core. Failure is defined as any hole or through-crack in the second facesheet of the honeycomb panel.

High-velocity, $V_n \geq 7$ km/s:

$$d_c = 2.98 \rho_p^{-1/3} (V \cos \theta)^{-2/3} \quad (5-12)$$

Low-velocity, $V_n \leq 2.5$ km/s:

$$d_c = 2.64 \rho_p^{-1/2} (\cos \theta)^{-5/3} V^{-2/3} \quad (5-13)$$

Intermediate-velocity, $2.5 \text{ km/s} < V_n < 7 \text{ km/s}$:

$$d_c = \left[\frac{1.43}{(\cos \theta) \rho_p^{0.5}} \right] \times \left[\frac{7.0 - V \cos \theta}{4.5} \right] + \left[0.814 \rho_p^{-1/3} \right] \times \left[\frac{V \cos \theta - 2.5}{4.5} \right] \quad (5-14)$$

Where

d_c = critical projectile diameter at failure threshold of the tile and substrate (cm)

ρ_p = projectile density (g/cm³)

θ = impact angle from target normal (deg); note impact at $\theta = 0$ deg is normal to the target

V = projectile velocity (km/s)

V_n = normal component of projectile velocity (km/s) = $V \cos \theta$

5.5 Penetration Equations for Insulated Aluminum Rear Wall behind Tile and Composite Substrate

The following equations define the critical particle size causing threshold perforation of an aluminum rear wall panel that is located at distance S behind a 5.1-cm-thick TUF-1-coated AETB-8 tile bonded to a 0.4-cm-thick SIP and a graphite-cyanate composite honeycomb panel. The graphite composite honeycomb sandwich has 0.2-cm-thick graphite-cyanate composite facesheets, and has an overall thickness of 3.8 cm including the honeycomb core. A high-temperature insulation pad, consisting of a beta-cloth bag filled with silica fiber insulation (0.2 g/cm² areal density for the entire insulation pad), was located directly on top of the aluminum panel. More details of the target and HVI test results are found in reference [53]. Failure is defined as any hole or through-crack in the aluminum rear wall.

High-velocity, $V_n \geq 7$ km/s:

$$d_c = \frac{2.98 \rho_p^{-1/3} V_n^{-2/3}}{3.19 \rho_p^{-1/3} V_n^{-2/3} S^{1/3} (t_w + 0.36 m_{MLI})^{2/3} (\sigma / 40)^{1/3}} + \quad (5-15)$$

Low-velocity, $V_n \leq 2.5$ km/s:

$$d_c = \frac{2.64 \rho_p^{-0.5} (\cos \theta)^{-5/3} V^{-2/3}}{1.67 \rho_p^{-1/2} V^{-2/3} (\cos \theta)^{-5/3} (t_w + 0.36 m_{MLI}) (\sigma / 40)^{1/2}} + \quad (5-16)$$

Intermediate-velocity, 2.5 km/s $< V_n < 7$ km/s :

$$d_c = d_{c-Lo} + (d_{c-Hi} - d_{c-Lo}) \left(\frac{V_n - 2.5}{4.5} \right) \quad (5-17)$$

$$d_{c-Lo} = \frac{1.43 \rho_p^{-0.5} (\cos \theta)^{-1}}{0.905 \rho_p^{-1/2} (\cos \theta)^{-1} (t_w + 0.36 m_{MLI}) (\sigma / 40)^{1/2}} + \quad (5-18)$$

$$d_{c-Hi} = \frac{0.814 \rho_p^{-1/3}}{0.872 \rho_p^{-1/3} S^{1/3} (t_w + 0.36 m_{MLI})^{2/3} (\sigma / 40)^{1/3}} + \quad (5-19)$$

Where

d_c = critical projectile diameter at failure threshold of the tile, substrate and aluminum rear wall (cm)

d_{c-Lo} and d_{c-Hi} = intermediate projectile diameter (cm)

ρ_p = projectile density (g/cm³)

m_{MLI} = areal density of insulation blanket (g/cm²)

S = standoff distance from back of substrate to front of rear wall (cm)

t_w = rear wall thickness (cm)

θ = impact angle from target normal (deg); note impact at $\theta = 0$ deg is normal to the target

σ = rear wall 0.2% offset tensile yield stress (ksi) (note 1ksi=1000 lb_f/in² = 6.895 MPa)

V = projectile velocity (km/s)

V_n = normal component of projectile velocity (km/s) = $V \cos \theta$

5.6 Advanced Flexible Reusable Surface Insulation Blanket Penetration Equation

Advanced Flexible Reusable Surface Insulation (AFRSI) is a TPS material consisting of bulk insulating layer of fibrous ceramic batting sandwiched between inner and outer ceramic fabric layers. The material has a quilt-like appearance with ceramic thread stitching. A gray ceramic C-9 coating covers the AFRSI. The penetration equations are valid for an AFRSI blanket bonded by RTV adhesive to a substrate. The equations could underestimate penetration depth for AFRSI not bonded to a substrate.

$$P = 1.44 d \rho_p^{0.5} (V \cos \theta)^{2/3} \quad (5-20)$$

Rearranging this equation:

$$d_c = 0.69 P_c \rho_p^{-0.5} (V \cos \theta)^{-2/3} \quad (5-21)$$

Where

d = projectile diameter (cm)

d_c = critical projectile diameter at threshold of critical penetration depth into the AFRSI (cm)

P = penetration depth into AFRSI (cm)

P_c = critical penetration depth at failure threshold (cm)

ρ_p = projectile density (g/cm^3)

θ = impact angle from target normal (deg); note impact at $\theta = 0$ deg is normal to the target

V = projectile velocity (km/s)

5.7 AFRSI and Composite Honeycomb Substructure Penetration Equations

Penetration equations below provide the critical particle size causing threshold perforation of a 2.2-cm-thick AFRSI blanket bonded to a graphite-cyanate composite honeycomb panel. The graphite composite honeycomb sandwich has 0.2-cm-thick graphite-cyanate composite facesheets, and has an overall thickness of 3.8 cm including the honeycomb core. Failure is defined as any hole or through-crack in the second facesheet of the honeycomb panel.

High-velocity, $V_n \geq 7$ km/s:

$$d_c = 2.0 \rho_p^{-1/3} (V \cos \theta)^{-2/3} \quad (5-22)$$

Low-velocity, $V_n \leq 2.5$ km/s:

$$d_c = 2.19 \rho_p^{-1/2} (\cos \theta)^{-5/3} V^{-2/3} \quad (5-23)$$

Intermediate-velocity, $2.5 \text{ km/s} < V_n < 7 \text{ km/s}$:

$$d_c = \left[\frac{1.189}{(\cos \theta) \rho_p^{0.5}} \right] \times \left[\frac{7.0 - V \cos \theta}{4.5} \right] + \left[0.547 \rho_p^{-1/3} \right] \times \left[\frac{V \cos \theta - 2.5}{4.5} \right] \quad (5-24)$$

Where

d_c = critical projectile diameter at failure threshold of the AFRSI blanket and composite honeycomb substrate (cm)

ρ_p = projectile density (g/cm^3)

θ = impact angle from target normal (deg); note impact at $\theta = 0$ deg is normal to the target

V = projectile velocity (km/s)

V_n = normal component of projectile velocity (km/s) = $V \cos \theta$

5.8 Penetration Equations for Insulated Aluminum Rear Wall behind AFRSI Blanket and Composite Substrate

The following equations define the critical particle size causing threshold perforation of an aluminum rear wall panel, that is located at distance S behind a 2.2-cm-thick AFRSI blanket (with C-9 ceramic coating) bonded to a 0.4-cm-thick SIP and a graphite-cyanate composite honeycomb panel. The graphite composite honeycomb sandwich has 0.2-cm-thick graphite-cyanate composite facesheets, and has an overall thickness of 3.8 cm including the honeycomb core. A high-temperature insulation pad, consisting of a beta-cloth bag filled with silica fiber insulation (0.2 g/cm^2 areal density for the entire insulation pad), was located directly on top of the aluminum panel. More details of the target and HVI test results are found in reference [53]. Failure is defined as any hole or through-crack in the aluminum rear wall.

High-velocity, $V_n \geq 7 \text{ km/s}$:

$$d_c = 3.19 \rho_p^{-1/3} V_n^{-2/3} S^{1/3} \left(t_w + 0.36 m_{MLI} \right)^{2/3} (\sigma / 40)^{1/3} + 2.0 \rho_p^{-1/3} V_n^{-2/3} \quad (5-25)$$

Low-velocity, $V_n \leq 2.5 \text{ km/s}$:

$$d_c = \frac{2.19 \rho_p^{-0.5} (\cos \theta)^{-5/3} V^{-2/3}}{1.67 \rho_p^{-1/2} V^{-2/3} (\cos \theta)^{-5/3} (t_w + 0.36 m_{MLI}) (\sigma / 40)^{1/2}} + \quad (5-26)$$

Intermediate-velocity, $2.5 \text{ km/s} < V_n < 7 \text{ km/s}$:

$$d_c = d_{c-Lo} + (d_{c-Hi} - d_{c-Lo}) \left(\frac{V_n - 2.5}{4.5} \right) \quad (5-27)$$

$$d_{c-Lo} = \frac{1.19 \rho_p^{-0.5} (\cos \theta)^{-1}}{0.905 \rho_p^{-1/2} (\cos \theta)^{-1} (t_w + 0.36 m_{MLI}) (\sigma / 40)^{1/2}} + \quad (5-28)$$

$$d_{c-Hi} = \frac{0.547 \rho_p^{-1/3}}{0.872 \rho_p^{-1/3} S^{1/3} (t_w + 0.36 m_{MLI})^{2/3} (\sigma / 40)^{1/3}} + \quad (5-29)$$

Where

d_c = critical projectile diameter at failure threshold of the AFRSI blanket, substrate and aluminum rear wall (cm)

d_{c-Lo} and d_{c-Hi} = intermediate projectile diameter (cm)

ρ_p = projectile density (g/cm^3)

m_{MLI} = areal density of insulation blanket (g/cm^2)

S = standoff distance from back of substrate to front of rear wall (cm)

t_w = rear wall thickness (cm)

θ = impact angle from target normal (deg); note impact at $\theta = 0$ deg is normal to the target

σ = rear wall 0.2% offset tensile yield stress (ksi) (note $1 \text{ ksi} = 1000 \text{ lb}_f/\text{in}^2 = 6.895 \text{ MPa}$)

V = projectile velocity (km/s)

V_n = normal component of projectile velocity (km/s) = $V \cos \theta$

5.9 Reinforced Carbon-Carbon Penetration Equations

RCC is a structural composite used as the TPS for the high-temperature areas of the Space Shuttle Orbiter (WLE and NC) and other space vehicles. A silicon carbide barrier is included on the exterior surfaces of the RCC to provide oxidation resistance and provide for reusability.

The RCC substrate is an all-carbon composite laminate fabricated in a multiple pyrolysis and densification process from a phenolic-graphite layup. The substrate has a density of 1.44 g/cm^3 to 1.6 g/cm^3 . A 0.5- to 1.0-mm-thick silicon carbide coating is formed on exterior surfaces of the RCC in a reaction diffusion process. Further oxidation resistance is provided by impregnation via treatment with tetrethyorthosilicate that, when

cured, leaves a silicon dioxide residue throughout the coating and substrate. Any remaining porosity and microcracks in the coating are filled by an application of a surface sealant (sodium silicate-silicon carbide mixture) in final steps of the fabrication process. For the Shuttle vehicle, typical RCC thickness is 6.4 mm, with the substrate 4.3 mm to 5.3 mm thick and the remainder silicon carbide coating.

A penetration equation for RCC [49-50] is as follows:

$$P = 0.61 d (\rho_p / \rho_t)^{0.5} (V \cos \theta)^{2/3} \quad (5-30)$$

Rearranging this equation:

$$d_c = 1.64 P_c (\rho_p / \rho_t)^{-0.5} (V \cos \theta)^{-2/3} \quad (5-31)$$

Where

- d = projectile diameter (cm)
- d_c = critical projectile diameter at threshold of critical penetration depth into the RCC (cm)
- P = penetration depth into RCC (cm)
- P_c = critical penetration depth at failure threshold (cm)
- ρ_p = projectile density (g/cm³)
- ρ_t = target density (g/cm³) = 1.6 g/cm³ for RCC
- θ = impact angle from target normal (deg); note impact at θ = 0 deg is normal to the target
- V = projectile velocity (km/s)

Figure 5-2 shows typical hypervelocity damage modes for RCC. Damage thresholds were established as a function of the projectile's normal component kinetic energy (the specified damage mode occurs at and above the given kinetic energy).

RCC becomes completely penetrated with increasing projectile size and/or velocity as the growing front-side crater meets the rear-side spall. The required thickness of RCC to prevent perforation is greater than the penetration depth as follows.

$$t_{\text{prevent_perforation}} = 2.3 P \quad (5-32)$$

And to prevent rear-side spall, the minimum RCC thickness is:

$$t_{\text{prevent_spall}} = 4.5 P \quad (5-33)$$

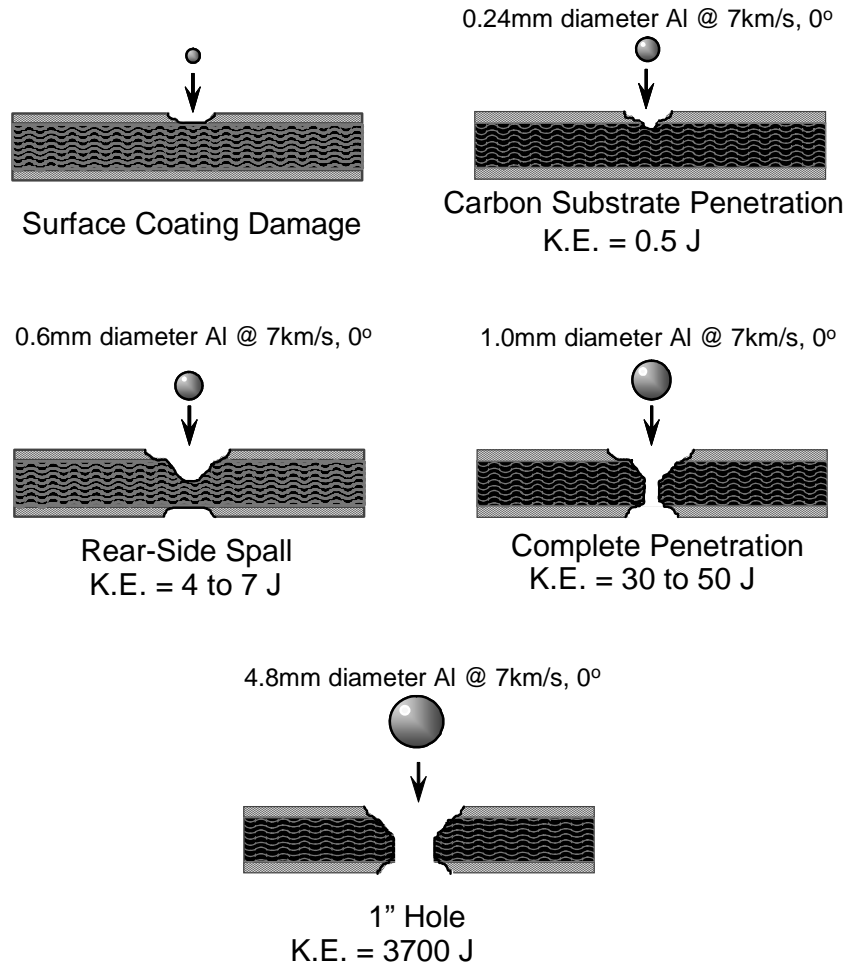


Figure 5-2. Hypervelocity impact damage modes and kinetic energy thresholds for RCC.

The following equation has been developed [49] to predict through-hole diameter in RCC if complete penetration occurs:

$$D_H = 2.20 d \rho_p^{1/3} (V \cos \theta)^{1/3} - 0.36 \quad (5-34)$$

Where

d = projectile diameter (cm)

D_H = hole diameter in RCC (cm) = equivalent circular hole diameter for elliptical holes = $(D_{\max} * D_{\min})^{0.5}$

ρ_p = projectile density (g/cm^3)

θ = impact angle from target normal (deg); note impact at $\theta = 0$ deg is normal to the target
 V = projectile velocity (km/s)

5.10 Penetration Equations for Ablators

Penetration equations have been developed for two types of TPS ablators: Phenolic Impregnated Carbon Ablator (PICA) and Avcoat. PICA was developed by NASA Ames Research Center and was the primary TPS material for the Stardust sample return capsule. PICA is being considered for use on Orion. Avcoat is an alternative heat shield material being considered for Orion, and it was the Apollo heat shield material.

5.10.1 Phenolic Impregnated Carbon Ablator Penetration Equation

PICA is a combination of carbon fiberform and phenolic resin that is made in a range of densities, from 0.24 g/cm³ for nominal density PICA to 0.48 g/cm³ for high-density PICA. A penetration equation for PICA based on impact test data is as follows:

$$P = 0.72 d^{0.85} \rho_p^{0.5} \rho_{PICA}^{-0.92} (V \cos \theta)^{2/3} \quad (5-35)$$

“Penetration” in this equation refers to the maximum cavity depth (see figure 5-3). In some cases, projectile fragments leave trails that penetrate beyond the open cavity in the PICA. The depth of these fragments is not predicted by the above equation. Rearranging this equation:

$$d_c = 1.47 P_c \rho_p^{-0.588} \rho_{PICA}^{1.082} (V \cos \theta)^{-0.784} \quad (5-36)$$

Where

d = projectile diameter (cm)
 d_c = critical projectile diameter at threshold of critical penetration depth into the PICA (cm)
 P = cavity penetration depth into PICA (cm)
 P_c = critical penetration depth at failure threshold (cm)
 ρ_p = projectile density (g/cm³)
 ρ_{PICA} = target density (g/cm³) = 0.24 – 0.48 g/cm³ for PICA
 θ = impact angle from target normal (deg); note impact at $\theta = 0$ deg is normal to the target
 V = projectile velocity (km/s)



Figure 5-3. Results from Test HITF-6023. Nominal density PICA. Top view on left, x-ray side view on right. Projectile: 0.32-cm-diameter Al 2017-T4 sphere, 6.59 km/s, 0° impact angle (normal to target). Damage size: 2.0 x 2.3 cm entry hole, 6.1 cm cavity depth, 3.8 cm maximum cavity diameter.

5.10.2 Avcoat Ablator Penetration Equation

Avcoat is a glass-phenolic ablative material used in the Apollo heat shield. The process to manufacture Avcoat was reconstituted and impact tests performed on the new Avcoat formulation. Previous Apollo-era Avcoat penetration equations [54] were modified based on results from the recent tests, as follows.

$$P = 1.25 d^{1.06} \rho_p^{0.5} (V \cos \theta)^{2/3} \quad \text{when } \rho_p / \rho_t < \text{or} = 4 \quad (5-37)$$

$$P = 1.61 d^{1.06} \rho_p^{0.5} (V \cos \theta)^{2/3} \quad \text{when } \rho_p / \rho_t > 4 \quad (5-38)$$

Where

d = projectile diameter (cm)

P = penetration depth into Avcoat (cm)

ρ_p = projectile density (g/cm^3)

ρ_t = target density (g/cm^3) = $0.528 \text{ g}/\text{cm}^3$ for Avcoat

θ = impact angle from target normal (deg); note impact at $\theta = 0$ deg is normal to the target

V = projectile velocity (km/s)

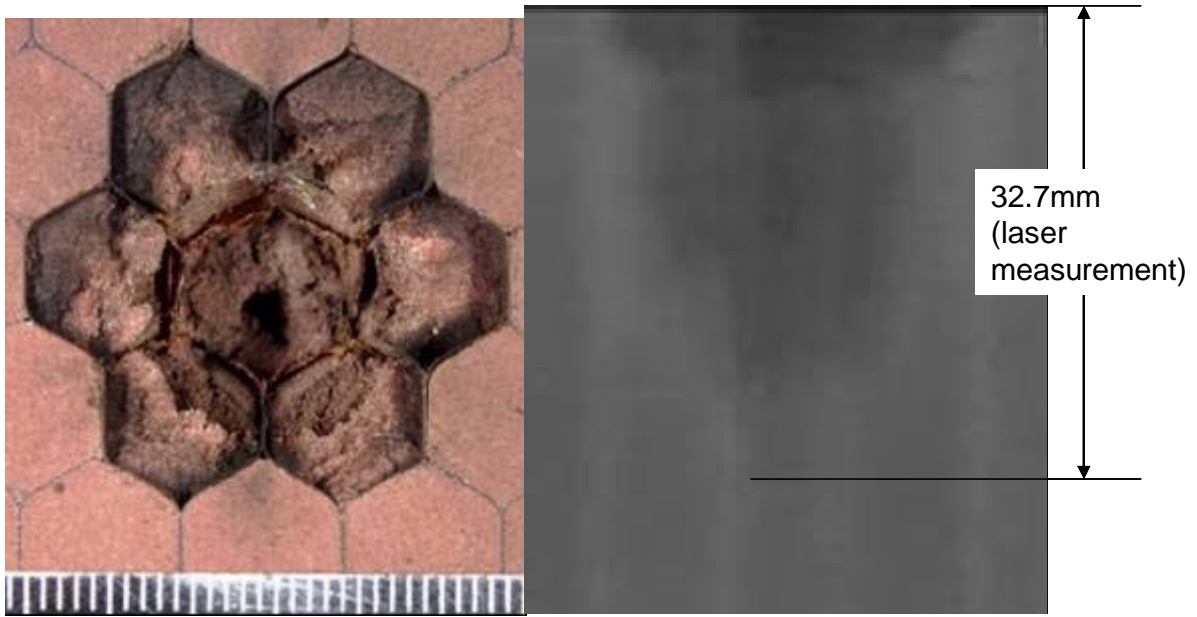


Figure 5-4. Results from Test HITF-8360 on Avcoat. On left is a top view and on right is an x-ray side view. Projectile: 0.34-cm-diameter Al 2017-T4 sphere, 6.98 km/s, 0° impact angle (normal to target). Damage size: 2.8 x 2.9 cm entry hole/surface damage size, 3.3 cm cavity depth.

6 Equations for Predicting Failure Limits of Spacecraft Hardware

This section provides BLEs for spacecraft hardware, including honeycomb panels, toughened MLI, and fused silica glass (used in window ports).

6.1 Honeycomb Panels

Honeycomb panels are often used in space vehicle construction due to their light weight and high strength and stiffness. However, honeycomb panels are more easily penetrated by hypervelocity MMOD particles compared to two walls of each thickness to the facesheets of the honeycomb panel (i.e., the panel without a honeycomb core), or compared to other core fills such as metal foam. The honeycomb core tends to channel the debris cloud behind the first facesheet, which results in greater penetration of the second facesheet compared to without the honeycomb core. A rough estimate of the ballistic limit for honeycomb sandwich structures is to use the Whipple shield equations (i.e., Equations 4-22 through 4-24 for example), and constrain the standoff distance to the product of twice the honeycomb cell diameter, or to the core thickness, whichever is less as follows:

$$S = \min (2 D_{Cell}, t_{HC-core}) \quad (6-1)$$

Where

S = shield standoff distance (cm)

D_{Cell} = honeycomb cell diameter (cm)

$t_{HC-core}$ = honeycomb core thickness (cm)

Additional honeycomb sandwich panel BLEs can be found elsewhere [48]. Methods to improve honeycomb sandwich ballistic limits include: (1) increase the diameter of the honeycomb cells; or (2) substitute a core material that does not channel the debris cloud, such as metal foam.

6.2 Toughened MLI

MLI thermal blankets cover many areas of the ISS and other spacecraft. These thermal blankets consist of 20 or more layers of ultra-thin materials (aluminized mylar or kapton for instance), with thicker exterior covers (both sides) to improve handling characteristics. MLI thermal blankets typically do not provide a large amount of additional MMOD protection. Toughening MLI thermal blankets with Nextel ceramic cloth and Kevlar high-strength fabric has been investigated in previous work [10, 55, 56]. For instance, a cooperative effort with the Canadian Space Agency resulted in toughening the MLI over critical electronic and propulsion systems on the RADARSAT satellite [56]. The RADARSAT MLI was modified to include one to two layers of Nextel AF10 ceramic fabric. The added mass was 0.25 to 0.5 kg/m², while the risk of penetration dropped by a factor of 3 [56].

Ballistic limits for a non-toughened (baseline) MLI thermal blanket (0.188 g/cm² mass per unit area) at a short distance (1.5 cm) from an aluminum rear wall are as follows. Failure criterion is defined as any hole or through-crack in the aluminum rear wall.

High-velocity, $V \geq 6.0 (\cos\theta)^{-0.5}$ km/s:

$$d_c = K_H t_w^{2/3} \rho_p^{-1/3} (V \cos\theta)^{-2/3} \quad (6-2)$$

Low-velocity, $V \leq 2.5 (\cos\theta)^{-1}$ km/s:

$$d_c = K_L V^{-2/3} (\cos\theta)^{-4/3} \rho_p^{-0.5} [t_w + 0.37 m_b] \quad (6-3)$$

Intermediate-velocity, $2.5 (\cos\theta)^{-1}$ km/s $< V < 6.0 (\cos\theta)^{-0.5}$ km/s :

$$d_c = \left[\frac{K_{li} [t_w + 0.37 m_b]}{(\cos\theta)^{2/3} \rho_p^{0.5}} \right] \times \left[\frac{6.0 (\cos\theta)^{-0.5} - V}{6.0 (\cos\theta)^{-0.5} - 2.5 (\cos\theta)^{-1}} \right] + \left[K_{hi} t_w^{2/3} \rho_p^{-1/3} (\cos\theta)^{-1/3} \right] \times \left[\frac{V - 2.5 (\cos\theta)^{-1}}{6.0 (\cos\theta)^{-0.5} - 2.5 (\cos\theta)^{-1}} \right] \quad (6-4)$$

Where

d_c = critical projectile diameter at failure threshold of the rear wall (cm)

K_H = high-velocity coefficient = 2.9 (for baseline MLI)

K_{hi} = high-intermediate velocity coefficient = 0.878 (for baseline MLI)

K_{li} = low-intermediate velocity coefficient = 0.923 (for baseline MLI)

K_L = low velocity coefficient = 1.7 (for baseline MLI)

ρ_p = projectile density (g/cm³)

m_b = areal density of MLI thermal blanket (g/cm²) = 0.188 g/cm² for baseline MLI

t_w = rear wall thickness (cm)

θ = impact angle from target normal (deg); note impact at $\theta = 0$ deg is normal to the target

V = projectile velocity (km/s)

V_n = normal component of projectile velocity (km/s) = $V \cos\theta$

Ballistic limits for a toughened MLI thermal blanket (0.307 g/cm² mass per unit area) at a short distance (1.5 cm) from an aluminum rear wall are as follows. The

toughened MLI in this case contains two layers of Nextel style AF10 (0.027 g/cm² each) added to the MLI just under the outer cover. In addition, three layers of Kevlar KM2 style CS-705 fabric (0.023 g/cm² each) are added to the back of the MLI. The areal density of the toughened MLI blanket is 0.307 g/cm². The general ballistic limits for the toughened MLI over aluminum rear wall are given below. Failure criterion is defined as any hole or through-crack in the aluminum rear wall.

High-velocity, $V \geq 6.2 (\cos\theta)^{-0.25}$ km/s:

$$d_c = K_H t_w^{2/3} \rho_p^{-1/3} (V \cos\theta)^{-2/3} \quad (6-5)$$

Low-velocity, $V \leq 2.5 (\cos\theta)^{-1}$ km/s:

$$d_c = K_L V^{-2/3} (\cos\theta)^{-4/3} \rho_p^{-0.5} [t_w + 0.37 m_b] \quad (6-6)$$

Intermediate-velocity, $2.5 (\cos\theta)^{-1}$ km/s $< V < 6.2 (\cos\theta)^{-0.25}$ km/s :

$$d_c = \left[\frac{K_{li} [t_w + 0.37 m_b]}{(\cos\theta)^{2/3} \rho_p^{0.5}} \right] \times \left[\frac{6.2 (\cos\theta)^{-0.25} - V}{6.2 (\cos\theta)^{-0.25} - 2.5 (\cos\theta)^{-1}} \right] + \left[K_{hi} t_w^{2/3} \rho_p^{-1/3} (\cos\theta)^{-1/3} \right] \times \left[\frac{V - 2.5 (\cos\theta)^{-1}}{6.2 (\cos\theta)^{-0.25} - 2.5 (\cos\theta)^{-1}} \right] \quad (6-7)$$

Where

d_c = critical projectile diameter at failure threshold of the rear wall (cm)

K_H = high-velocity coefficient = 1.34 (for Nextel/Kevlar toughened MLI)

K_{hi} = high-intermediate velocity coefficient = 0.729 (for toughened MLI)

K_{li} = low-intermediate velocity coefficient = 0.923 (for toughened MLI)

K_L = low velocity coefficient = 1.7 (for toughened MLI)

ρ_p = projectile density (g/cm³)

m_b = areal density of MLI thermal blanket (g/cm²) = 0.307 g/cm² for Nextel/Kevlar toughened thermal blanket

t_w = rear wall thickness (cm)

θ = impact angle from target normal (deg); note impact at $\theta = 0$ deg is normal to the target

V = projectile velocity (km/s)

V_n = normal component of projectile velocity (km/s) = $V \cos\theta$

Table 6-1 provides example critical particle sizes for the two MLI concepts (baseline and Nextel/Kevlar enhanced MLI) with a 0.19-cm-thick AMG-6 rear wall assumed in the calculated BLEs for the two concepts. Another example of the use of a toughened MLI option is to upgrade the current baseline MLI thermal blanket on the Orbital Module of the Soyuz with a toughened blanket. The Orbital Module of the Soyuz (the round pressurized crew module at the front of the vehicle) represents the MMOD risk driver for the Soyuz. Over 80% of the Soyuz MMOD risk is due to the Orbital Module [10], because of the thin shielding in this region of the vehicle; i.e., MMOD protection is with the baseline MLI blanket at short distance (1.5 cm) from a 0.19-cm-thick aluminum pressure shell (alloy AMG6). Adding Nextel and Kevlar to the MLI blanket provides considerable improvement in MMOD protection. The Nextel ceramic fabric in the enhanced MLI blanket acts like an additional bumper to improve projectile breakup. The Kevlar is a good debris cloud “catcher.” Table 6-2 shows the reduction in MMOD risks using the enhanced blanket in place of a baseline blanket, and the option adds 20 kg to the vehicle if implemented.

Table 6-1. Example Aluminum Particle Diameters at Ballistic Limit of two MLI Configurations (baseline and Nextel/Kevlar toughened) at 1.5 cm Standoff from 0.19-cm-thick Aluminum AMG6 Rear Wall

Impact Conditions	Critical particle diameter for baseline MLI (cm)	Critical particle diameter for toughened MLI (cm)
At 3 km/s, 0° impact angle	0.152	0.190
At 7 km/s, 0° impact angle	0.186	0.286
At 9 km/s, 45° impact angle	0.198	0.295

Table 6-2. MMOD Penetration Risk over 15 years for Soyuz Protection Options [10]. Penetration is defined as a hole or through-crack in the pressure shell or critical damage to propellant tanks.

Protection Case	PNP	MMOD Risk	MMOD Risk Reduction
Baseline MLI	0.900	10%	-
Toughened MLI over Orbital Module	0.966	3.4%	Factor of 3X

6.3 Transparent Materials

Fused silica glass is typically used for window ports on the Shuttle, ISS, and other spacecraft. Recent work on polycarbonate materials indicates they have greater damage tolerance from MMOD impact than conventional fused silica glass.

6.3.1 Fused Silica Penetration Equations

The following equation predicts penetration depth into fused silica glass [57].

$$P = 0.53 d^{1.06} \rho_p^{0.5} (V \cos \theta)^{2/3} \quad (6-8)$$

$$d_c = \left[1.89 P_c \rho_p^{-0.5} (V \cos \theta)^{-2/3} \right]^{0.94} \quad (6-9)$$

Where

d = projectile diameter (cm)

d_c = critical projectile diameter at threshold of critical penetration depth into fused silica glass (cm)

P = cavity penetration depth into fused silica glass (cm)

P_c = critical penetration depth at failure threshold (cm)

ρ_p = projectile density (g/cm^3)

θ = impact angle from target normal (deg); note impact at $\theta = 0$ deg is normal to the target

V = projectile velocity (km/s)

For no perforation of the fused silica glass, the thickness must be two times greater than the penetration depth in semi-infinite glass, that is:

$$t_{\text{prevent_perforation}} = 2 P \quad (6-10)$$

To prevent rear-side detached spall, the minimum glass thickness is:

$$t_{\text{prevent_spall}} = 3 P \quad (6-11)$$

And to prevent any cracks on the rear side of the glass, the minimum glass thickness is:

$$t_{\text{prevent_spall_cracks}} = 7 P \quad (6-12)$$

Rearranging:

$$d_{c_perforation} = 0.95 t^{0.94} \rho_p^{-0.47} (V \cos \theta)^{-0.63} \quad (6-13)$$

Where

d = projectile diameter (cm)

$d_{c_perforation}$ = critical projectile diameter at threshold of completely penetrating a fused silica glass plate of thickness t (cm)

t = thickness of fused silica glass (cm)

ρ_p = projectile density (g/cm³)

θ = impact angle from target normal (deg); note impact at $\theta = 0$ deg is normal to the target

V = projectile velocity (km/s)

6.3.2 Penetration Equations for Polycarbonate

Hyzod AR⁶ polycarbonate is a transparent amorphous thermoplastic with a hard coated surface that resists abrasion providing high impact strength and high modulus of elasticity. Hyzod AR has impact strength 250 times stronger than float glass and 30 times stronger than acrylic. Hyzod polycarbonate is currently being used as a transparent cover protecting ISS hatch windows. Details of HVI testing and damage equations for polycarbonate are given in reference [56, 57].

The impact particle size at the perforation limit of a polycarbonate plate is given by the following equation.

$$d_{c_perforation} = 1.04 t_{PC} \rho_p^{-1/3} V^{-2/3} (\cos \theta)^{-1/3} \quad (6-14)$$

The impact particle size at the detached spall threshold from rear side of a polycarbonate plate is given by:

$$d_{c_detached_spall} = 0.98 t_{PC} \rho_p^{-1/3} V^{-2/3} (\cos \theta)^{-1/3} \quad (6-15)$$

The impact particle size at the attached spall threshold from rear side a polycarbonate plate is given by:

$$d_{c_attached_spall} = 0.65 t_{PC} \rho_p^{-1/3} V^{-2/3} (\cos \theta)^{-1/3} \quad (6-16)$$

Where

d = projectile diameter (cm)

⁶ Hyzod AR is a trademark of Sheffield Plastics, Inc.

$d_{c_perforation}$ = critical projectile diameter at threshold of completely penetrating a fused silica glass plate of thickness t (cm)
 t_{PC} = thickness of polycarbonate (cm)
 ρ_p = projectile density (g/cm^3)
 θ = impact angle from target normal (deg); note impact at $\theta = 0$ deg is normal to the target
 V = projectile velocity (km/s)

Polycarbonate reduces the mass to stop a given size particle compared to fused silica, as given in figure 6-1.

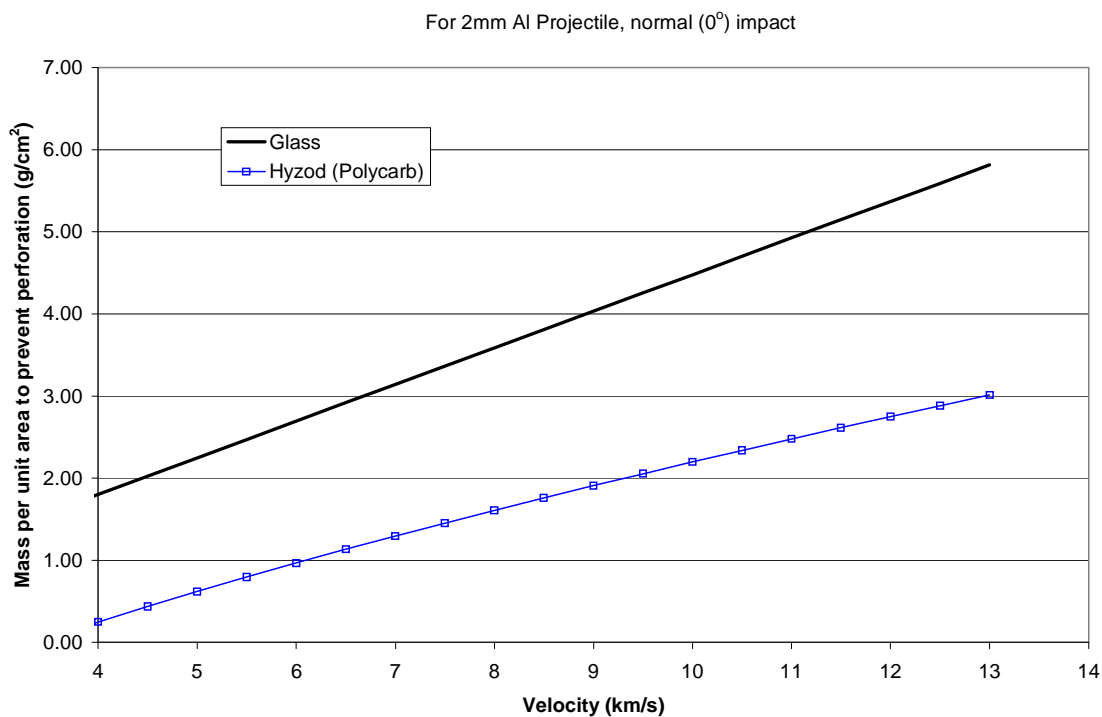


Figure 6-1. Hyzod and Fused Silica mass per unit area to prevent perforation, as a function of impact velocity for a 0.2-cm-diameter aluminum projectile at 0° impact angle.

7 MMOD Damage Detection Sensors

NASA has developed a number of systems that detect MMOD impact strikes on spacecraft. Knowledge of a strike can simply be noted if there is no damage, or it can provide a powerful clue if an air leak occurs, or if there is some other equipment malfunction.

In the case of the Mir accident, for instance, months passed while the Russian Space Agency determined exactly where on the pressure hull the breach had occurred. With the use of damage detection sensors, there is additional information to investigate these types of problems.

This becomes more significant with long spaceflights. In the case of Mir, or the ISS, if there is a serious breach of pressure integrity (i.e., the craft is leaking air) the crew can always “come home.” They are in Earth orbit and space rules dictate that there is always the capacity to return crew members in the event of an emergency. A mission to the moon, however, or a mission to Mars, takes days or months and immediate return is not usually possible.

In a spacecraft with a breached pressure hull, the crew would have to spend a lot of time, if not all of it, in spacesuits, with the accompanying long-term problems of eating, drinking, and sanitation. With knowledge of where the strike occurred, the crew has an opportunity to repair the damage and regain pressure integrity in their vessel.

7.1 Impact Damage Detection using Piezoelectric Film Sensors

One type of “Strike Detector” utilizes a blanket approach to detecting projectile impacts. It covers the area to be monitored with a piezoelectric film that has the property that a mechanical impact on the film causes an electrical output. An example of the piezoelectric effect is found as an accessory on backyard gas grills. These grills typically have an igniter. Pressing the button on the igniter results in a mechanical impulse, which hits a piezoelectric element and creates an electrical spark to start the flame. The piezoelectric film operates in a similar manner as the backyard grill igniter, except it is much thinner and will not create as great a voltage. Nevertheless, it will output an easily measurable signal.

The piezoelectric film consists of a polyvinylidene fluoride (PVDF) plastic with a metalized layer on each side (figure 7-1). The voltage difference that results from a mechanical strike occurs between the two metalized layers. This voltage difference is detected and the location of the strike determined by subdividing the film into distinct sections.

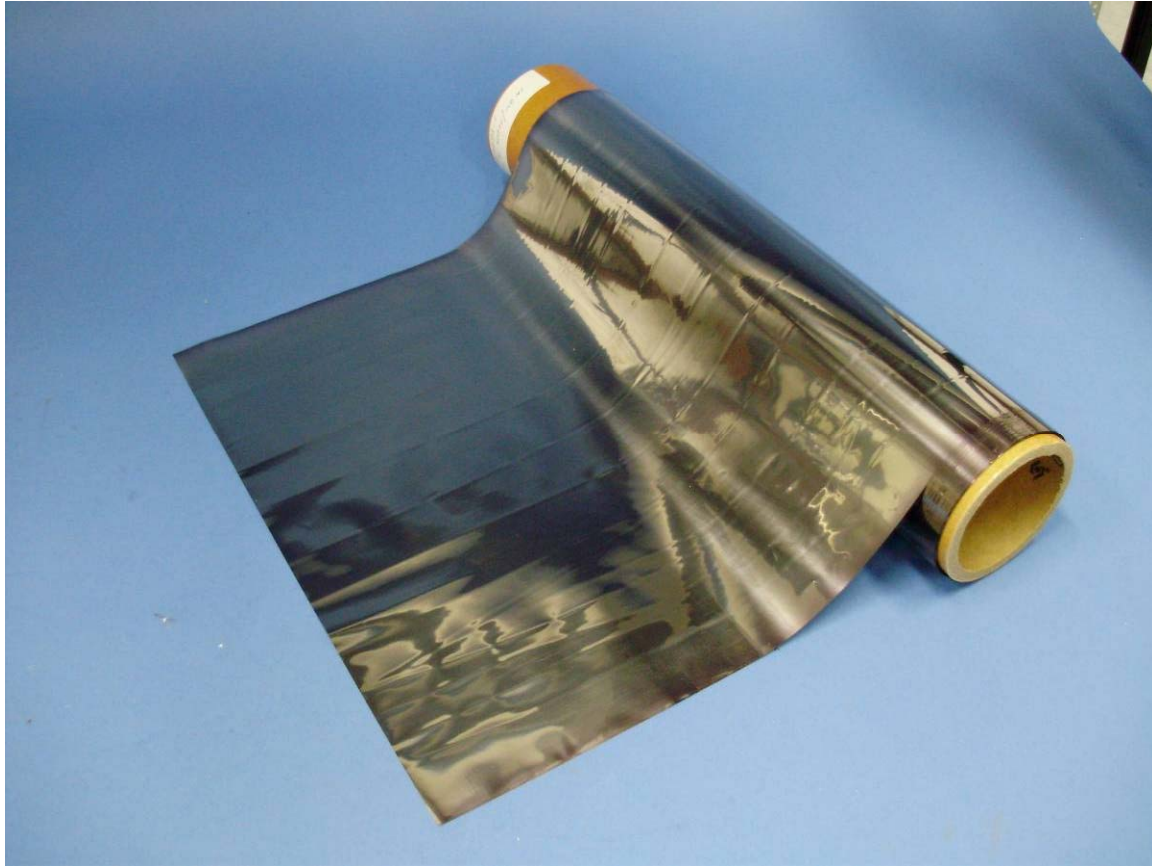


Figure 7-1. PVDF film.

7.1.1 Application of Piezoelectric Blanket Strike Detector to Spacecraft

Covering the spacecraft with a piezoelectric blanket is not that much of a burden. There is typically an MLI thermal blanket covering the hull or exterior a spacecraft. There may also be shielding consisting of light aluminum panels covering the sensitive areas of the spacecraft. The addition of a layer of film does not have a significant effect on the overall combination.

The Strike Detector consists of a series of panels, arranged together in an array to cover whatever surface area needs monitoring. The panels are usually of a uniform size and type, but this is not required. A typical size for a panel could be 2 feet x 3 feet. The panels are attached to each other in an X and Y direction, until the area of interest is covered (figure 7-2). It is not required that the panels all be uniform, and if circumstances dictate that another size of panel would be better for a particular area, that can be done.

The panels are all in communication with a centralized electronics module that is typically located inside the pressure hull. The centralized module talks with the various panels and makes decisions based on the information received. The module displays the information to the spacecraft crew and provides data for telemetry to the ground. A typical centralized module consists of a laptop computer attached to a small electronics unit.

A 2-wire buss system connects the panels. These two wires provide power and data to all panels. Each panel can be built with the 2-wire buss running to each of its four sides so that it is possible to add a new panel by attaching it onto the top, bottom, left, or right of any existing panel. An array of panels can cover any imaginable surface.

The panels physically nearest the centralized electronics module connect to it via the two-wire buss. Since the module is typically inside the pressure hull and the panels are outside, this requires two electrical feed-throughs through the pressure barrier.

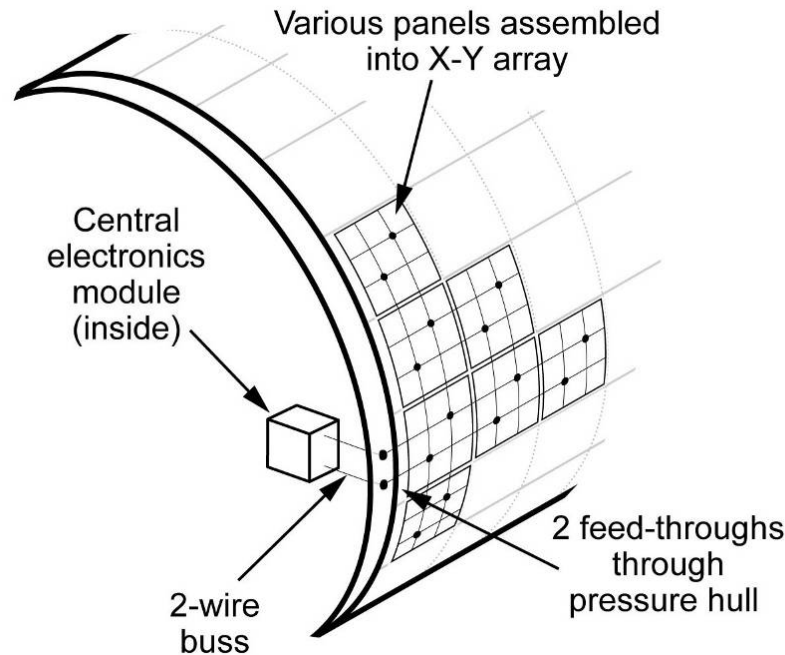


Figure 7-2. Panels arranged into a detector array.

7.1.2 Inside a Strike Detector Panel

Each panel is (usually) similar to every other panel, although each is maintained as a unique entity. A panel has its own set of electronics to communicate with the central module, and inside the electronics is a unique software address to identify the panel specifically. A particular panel can be located almost anywhere, but there needs to be a log of exactly where each one is being used.

Panels are subsequently divided into “pixels” (figure 7-3). Each pixel represents the smallest area where an impact can be located. For instance, if a 2-foot by 3-foot panel is divided into six 1-foot square pixels, then an impact could be detected from any of the six pixels. Each pixel has a separate wire to connect it to the panel electronics.



Figure 7-3. Picture of film divided into 48 pixels.

In the panel electronics, there is a register that equates to the number of pixels. If the panel has 12 pixels, there is an associated “Main” register of 12 bits, where each bit corresponds to a particular pixel. If a signal is generated by pixel #3, and if the signal exceeds the threshold requirement, then it will set the #3 bit in the Main register. The panel registers will subsequently be read by the central electronics module, which will now know the identity of the panel, and the identity of the pixel(s) that are reporting being hit.

There is a second register in each panel electronics, similar to the Main register. The second register is referred to as the First-To-Arrive (FTA) register and is exactly the same size as the Main. The purpose of the FTA register will be discussed in a later section.

Finally, each panel can perform secondary tests on its pixels. One test is to check if any pixels are shorting to the backplane. Shorting is a common consequence of an impact, usually as a result of the piezoelectric material being torn and allowing the conductive layers on each side to touch together.

Another secondary test that each panel can perform on its pixels is to conduct a capacitance test. Each pixel will normally have a certain amount of capacitance,

dependent on its physical size. If a pixel is significantly “blown away” by an impact, or if the wiring to the pixel is cut, there will be a dramatic reduction in the amount of capacitance measured.

These secondary tests can provide valuable information in addition to the primary piezoelectric signal.

7.1.3 Testing and Characterization of the Strike Detector

Extensive testing of the detector has taken place at NASA’s facilities at JSC, at Rice University in Houston, and at NASA’s White Sands Test Facility in New Mexico. Results show that the piezoelectric film does a good job of detecting when a projectile hits a pixel in a panel.

In a majority of the cases, the sensitivity of the pixels is high enough that one impact has the effect of being detected by multiple pixels, and not just the one being hit. To some extent this is a useful mechanism, since viewing the area where the pixels are responding will indicate an area, in the middle of which is where the actual impact took place. The number of pixels that are responding gives an indication of the severity of the impact.

To improve the resolution as to which pixel actually got hit, a technique was developed using the time occurrence of the various signals. The non-impacted pixels that respond are detecting the mechanical vibrations from the impact. These mechanical forces travel across the surface of the detector at sonic velocity, so there is a measurable difference in the time in which each signal arrives. The pixel that suffered the impact will always be the first to respond, and it is recorded in the FTA register, which then inhibits itself to any further inputs. All subsequent signals are recorded in the Main register. The pixel signals are thus resolved into the FTA and then everybody else. Typically, after a hit, there will be one bit set in the FTA register, and several bits set in the Main register.

Interestingly, it is not absolute that there will only be one bit set in the FTA register. The realities of the electronics are that it takes a short, but finite, amount of time for the FTA register to realize it has a bit set, and inhibit itself to any more inputs. Currently, this amount of time is around 40 nanoseconds. Therefore, if the first two signals (or more) are less than 40 nanoseconds apart, then both of them will set bits in the FTA register. This situation never happens when there is a clean shot on the detector, but it is not unknown to occur when the detector is behind a shield, or some other barrier that produces a debris cloud or cone of debris. Particles of the debris cloud can hit the detector at the same time (arriving within the 40-nanosecond gate) and produce multiple FTA bits. The detector is reporting what it is experiencing. If multiple FTAs happen, then that provides information that there was a debris cloud and the lateral extent of the debris cloud.

The secondary data from the Shorts and Capacitance tests also give insight into the nature and extent of the damage. If pixels are measured as being shorted after an impact, that indicates that the material has been torn, or at least showered with debris, and it must have been near the hit. If a pixel has lost capacitance, that is evidence that material has disappeared, and it was presumably located where the hit occurred.

7.1.4 Specifications of the Strike Detector

A cross-sectional diagram of a typical strike detector is shown in figure 7-4. The type of PVDF used in the current version of the NASA Strike Detector is a film 27 microns thick. This film is usually manufactured in rolls up to 24 inches wide. Thus, a panel can be as long as desired, and up to 24 inches wide. Each film is encapsulated front and back with 1-mil-thick polyimide, currently Kapton, and conductive ink is screen printed onto the polyimide for the wiring. The electronics are also located on this layer.

Another layer of polyimide, with conductive ink traces, carries the 2-wire power and data buss.

Two more layers of polyimide carries a second set of wiring and electronics, and a second 2-wire buss. These provide redundancy for the detector, hence some survivability. The detector will always note the first hit quite well; however, depending on the amount of damage, an area may be in poor condition to report on any subsequent events. Providing a second path for all functions means that the detector can still respond, until at least a second hit to that area at least, or until the damaged panel can be replaced.

Finally, a top and bottom layer of polyimide is used to provide an overall cover to the assembly. The detector cross section is then one layer of foil, and seven layers of polyimide. The weight per area of the complete detector (figure 7-5) is 5.185 oz/ft² (1.6 kg/m²).

Power consumed by the Strike Detector is small while it is in its normal monitoring mode. Since the actual detection mechanism is piezoelectric, no power at all is required by the sensing element. The film will convert the kinetic energy of an incoming projectile into an electrical signal.

Some power is needed by the associated panel electronics, however. The electronics consist mostly of a Complementary Metal-Oxide Semiconductor gate array and typically uses around 10 milliwatts. If the secondary electronics is also turned on, it would require an identical amount.

When a strike is detected, the affected panel signals the central electronics. The central electronics module will command the panels out of monitoring mode and into a higher power communications mode. When this happens, embedded processors in the panels will awaken and become available for bidirectional communication with the module. The amount of power required when in the communication mode is greater than when in the regular monitoring mode, but after communications are finished the panels are put back into the low-power monitoring mode.

Since a large part of the panel electronics is a single gate array, there is a practical limit on how many pixels can be in a panel. Each pixel has to have a unique line into the gate array, and there are a maximum number of pins available on the gate array. Currently, the NASA Strike Detector uses a 160-pin gate array, which makes available 96 pins for pixels. Thus, there is a limit of 96 pixels per panel.

The software address for each panel is 8 bits in length so, at the present time, the maximum number of panels is 256. That number is easily changed, of course.

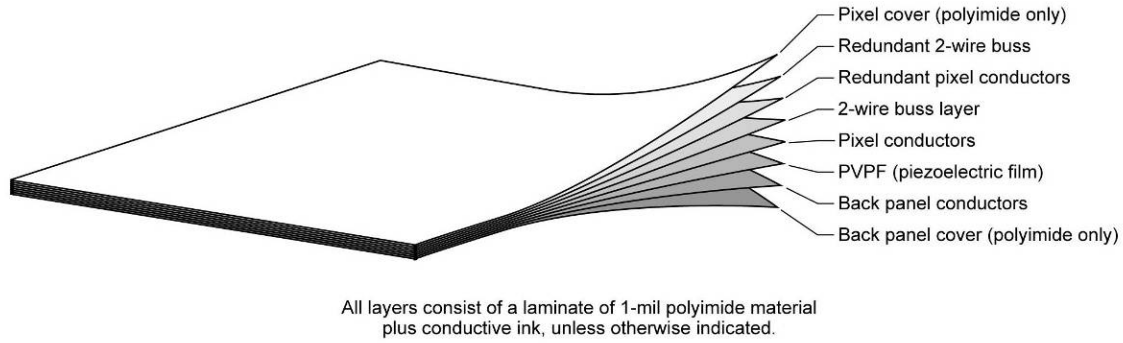


Figure 7-4. Cross-section of panel construction.

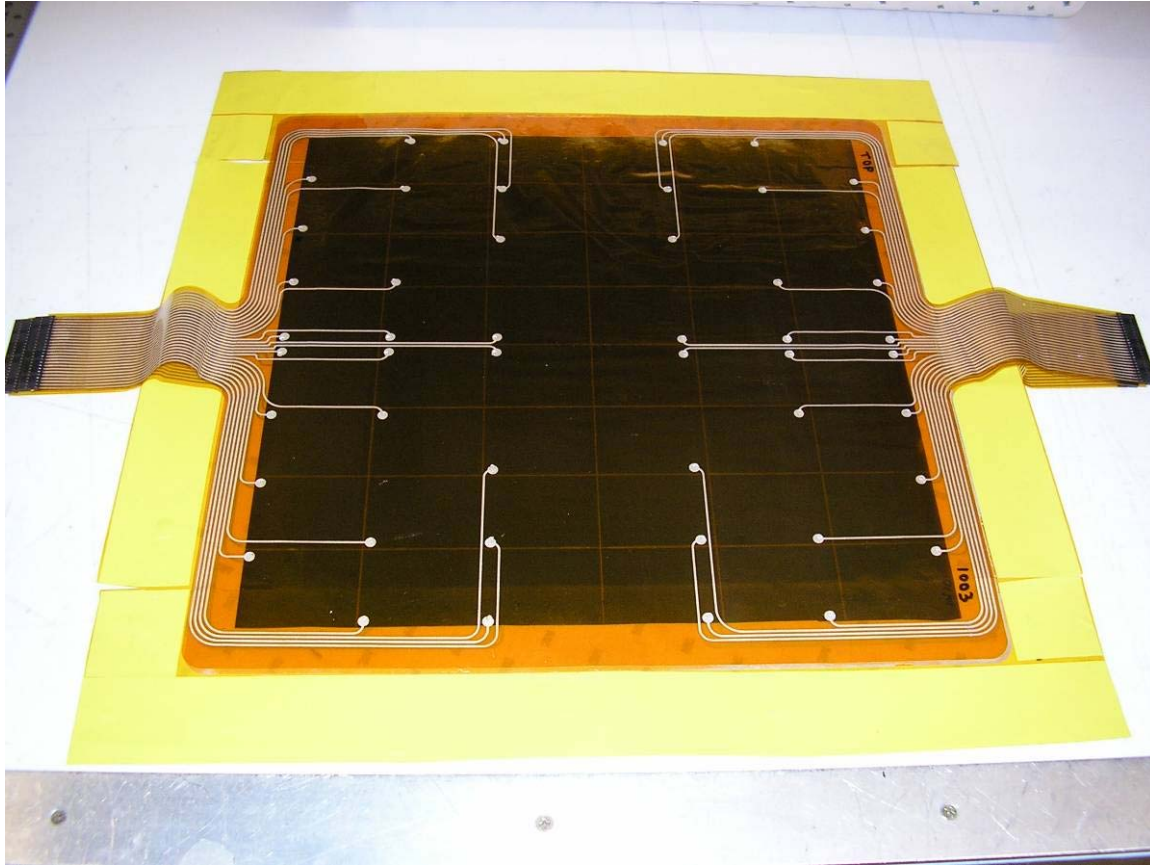


Figure 7-5. Piezoelectric pixels encapsulated with polyimide layers and conductive ink circuitry applied.

7.1.5 Example Application

An example could be a cylindrical object of 10 feet diameter and 30 feet long, a large but not unreasonable size for spacecraft components. For purposes of this discussion, the area at the ends will be neglected, but these can be “added on.”

The area of interest is the circumference times the length, or an area of 942 ft².

Since each panel can be a maximum of 24 inches wide, the panels could be constructed to travel down the length of the cylinder. Each panel would then be 24 inch x 30 feet, or 60 ft². This would mandate just over 15 panels to completely cover the sides of the cylinder. If 1 ft² resolution is acceptable as a criterion for actual strike detection and location, then there would be 60 pixels per panel. Overall, there would be 942 pixels, since the area is 942 ft².

The weight of a single panel, with full redundancy, would be 5.185 oz/ft² x 60 ft² = 19.4 lbs. The total weight of all the panels would be 305 lbs.

Individual panel power would be 10 milliwatts, for a total power of 160 milliwatts in monitor mode (assuming 16 panels). The power would increase to several watts when in communication mode.

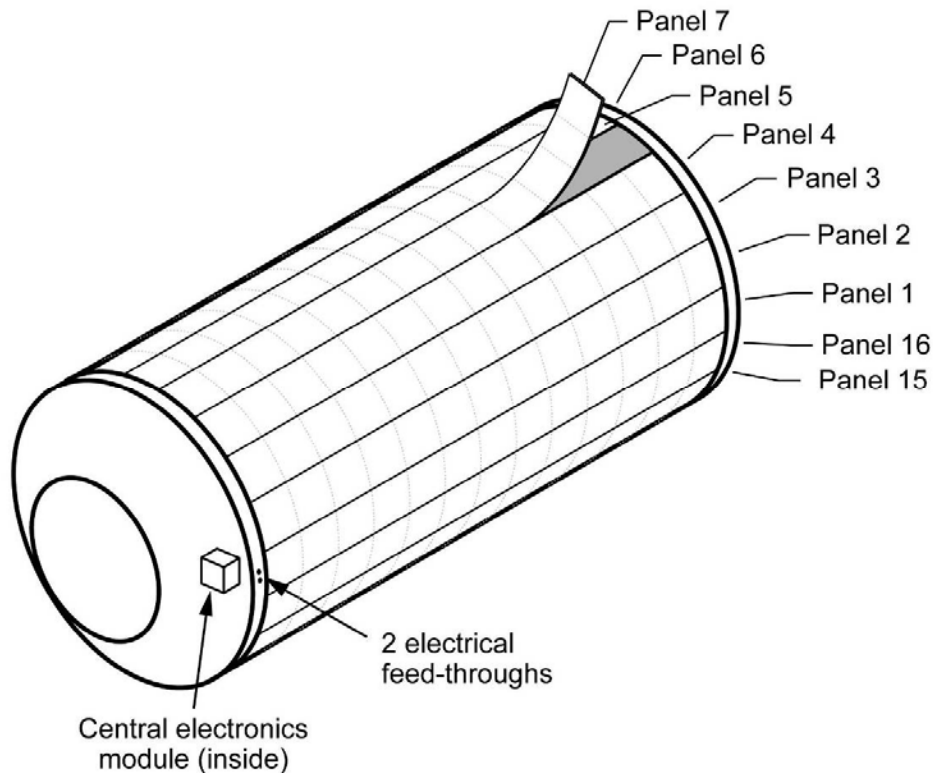


Figure 7-6. Application example showing 16 panels (2 ft wide x 30 ft long) to cover spacecraft shell.

7.1.6 Operational Scenario

When the detector described in the previous section receives a hit, the following process would take place.

- The pixel, or pixels, that received the impact would send the signals to their panel's electronics. The panel electronics would store this information in its Main and FTA registers.
- The panel electronics would then signal to the Central Module that it had recorded a hit.
- The Central Module would then bring all the panels into communicate mode. At this time, the module does not know which panel was struck, only that one had raised the alarm.

- The Central Module then broadcasts a request for the panel that raised the alarm to identify itself. A broadcast command is received by all panels because it has a generalized address that is received by them all.
- The affected panel communicates to the module. If there is more than one panel that needs to respond, there is a buss arbitration protocol to ensure that all panels get a chance to communicate.
- The module then requests the Main and FTA register information of the particular panel, which the panel sends. The module then directs the panel to perform the secondary tests, Shorts and Capacitance, to determine the extent of the damage. The panel complies by performing the secondary tests and reports the results to the module.
- The module repeats this sequence on any other panels that may have indicated being struck. When finished, it broadcasts a reset command to all the panels and puts them all back into monitor mode.
- The central electronics module then examines and presents the data to the crew and spacecraft telemetry. It presents a graphical image showing where the hit occurred on the structure, and how much damage the detector suffered. The amount of damage suffered by the detector indicates the seriousness of the strike.

This entire process takes a matter of seconds, so the information presented to the crew is basically real-time.

7.1.7 Number of Detectors

The NASA Strike Detector is a straightforward way to determine when and where an impact occurs. There have been many tests of the technique, and it has proven to be robust and reliable, particularly for the first impact. Accuracy of a detector receiving a clean shot is basically 100%.

A variation is to use two detectors, one a few inches above the other, to determine characteristics about the projectile. If there is a clean signal from each detector, various parameters can be determined by comparing the two signals' location and timing, such as the projectile trajectory vector and its speed. In actual tests of this concept, the reliability of the numbers depends in part on the angle the projectile relative to the detector planes. If the trajectory is normal to the plane, the numbers are typically quite good. But if it is at a significant angle, say 45 to 60 degrees, then in about half the cases there is some ambiguity. The first detector always indicates correctly, but the second detector can be subjected to a shower of debris that can distort the reading. In these high-angle cases, the possibility of getting a non-ambiguous reading on the second detector (i.e., only one pixel in the FTA) is approximately 50%. Even in these cases, however, there is still valuable information. It can still be determined in which general direction the impact came from, even though the exact angle may be somewhat ambiguous.

Survivability after the first impact is being evaluated now, and reliability is being improved with the addition of a backup set of electronics and the power/data buss. This may not be required for all cases. If the detector is protecting an inflatable structure, for instance, a strike that is big enough to significantly damage the detector is big enough that repairs would be warranted on the structure, so the detector panel could be replaced at that time.

If the backup reliability is not required, two layers of polyimide could be dispensed with, saving nearly 30% of the weight. In the 10-foot by 30-foot cylinder example, the weight would drop from 305 lb to 217 lb.

It is even theoretically possible to garner some projectile information from the signal shape itself, although tests have revealed this to be rather involved. It is an area for future development.

The best use of the Strike Detector depends on the exact requirements. At this time, to monitor the pressure hull of a typical spacecraft it would seem that a single layer of the detector, with a second level of redundancy, should be located against the pressure hull. Dust and small debris that do not make it to the pressure hull would not be measured. More significant projectiles that do make it to the hull would be detected. Even stronger impacts that are capable of doing damage would be measured and damage noted on the secondary tests.

This Strike Detector promises a reliable and affordable way to monitor the impact environment around a spacecraft. It was the subject of a disclosure in the NASA Tech Briefs [58].

7.2 Acoustic Sensor Detector

When a particle impacts the target, it generates a transient acoustic signal. The impacts are energetic (typically greater than 100 micro-joule); hence, the resulting acoustic signal is typically strong. This transient acoustical signal travels through the structure developing small structural strains as it propagates. These strains are easily detected using PVDF sensors. The resulting electrical signal is conditioned by an associated preamplifier and is passed to the data acquisition system. The frequency content of signals generated is typically in the 100 kHz range. An example is shown in figure 7-7.

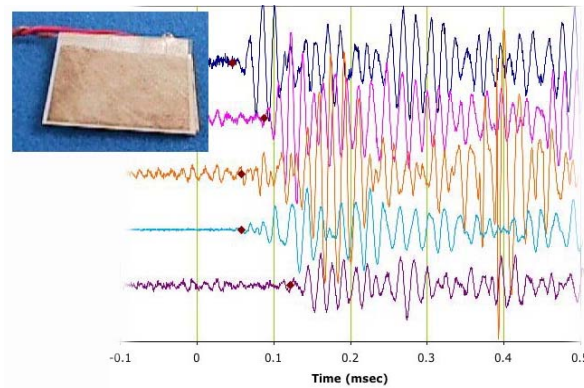


Figure 7-7. Typical sensor signals from 1 milli-Joule impact.

7.2.1 *PINDROP Acoustic Sensor System*

The Particle Impact Noise Detection and Ranging on Autonomous Platform (PINDROP) acoustic sensor system detects a HVI by sensing the acoustic wave generated in a target material. The sensors used are typically small (2 cm), thin (25 micron) PVDF piezoelectric polymers. These sensors generate an electrical signal in response to an acoustic strain, where the signal amplitude provides a measure of the impact energy or momentum (depending on target material). Hypervelocity particles larger than 30 micron are easily detected and, if desired, the impact location of the particle on the target can be deduced from the signal arrival times at multiple sensors.

The sensor system is applicable to a wide variety of target materials and structures. Because of this versatility, this sensor system is usually not developed as a separate independent structure, but rather makes use of other structures already present or proposed. For example, initially it was developed for use in combination with an aerogel capture tray. It has also been studied for use in combination with other sensor (resistive, optical, etc.) to provide accurate event timing and additional information about the impacting particle.

An alternative deployment is to simply distribute an array of sensors on the spacecraft or lunar habitat structures to form a large area sensor system. The versatility of this approach has been demonstrated in HVI tests, where large signals were measured for particle impacts on MLI thermal blankets (front and back layers), single- and multi-layer woven Kevlar fabric shields, thin Mylar film, graphite composite boards, and solid aluminum plates and structures. Hence, promising locations for sensors include antennas, solar panels, Whipple shields, and thermal blankets. This type of deployment is more complicated to marry to the spacecraft or lunar structures, since the structural complexity along the path from impact location to sensor must be minimized. However, the approach is quite suitable for detecting impacts by meteoroids larger than 50 micron. Because of its large effective aperture, it can improve our statistical sampling of these large micro-meteoroids by nearly an order of magnitude over what can be achieved with a system using a dedicated surface, and this can be done at a considerable mass savings.

In general, the system requirements are modest. The sensor, cable, and preamplifier have a combined mass of typically 20 gm per sensor, and power consumption of 15 mW per sensor. A typical system, consisting of 32 sensors with two 16-channel preamplifier modules, has a total system mass of less than 1 kg and a power draw of 0.5 watts (continuous).

This PINDROP project was originally developed under the NASA Planetary Instrument Definition and Development Program. It became a key component of the Large Area Debris Collector (LAD-C) aerogel collector system (intended for flight on the ISS as a Department of Defense [DoD] Space Test Program payload). The system passed Preliminary Design Review and was undergoing space qualification tests when the LAD-C program was discontinued, a direct result of NASA's decision to terminate the STS program in 2010. The principal development still needed for the PINDROP system would be calibration of the target material and structure selection, space qualification of the components, and development of the electrical interface to the spacecraft. Also, parts and prototype implementations conform to the potential space environment, and since the sensor system was tested with realistic supporting elements, the system is felt to be at Technology Readiness Level (TRL)-5.

7.2.2 Acoustic Sensor Application Considerations for Metallic Modules

In a series of tests, data was collected on hypervelocity (5 km/s) particles impacting aluminum plates (figure 7-8). The plates were type 6061 aluminum, 25 cm (10 inches) square, and 1.59 mm (1/16 inch) thick. The 0.8 mm particles penetrated the sample, leaving a hole approximately 3 mm in diameter. The large acoustic signal developed at each of these sensors was found to have a voltage level of approximately 0.8 volts p/p. Similar signal voltage levels were found for both normal (perpendicular) and 45° particle impacts. Smaller 0.3-mm-diameter particles did not penetrate, and generated acoustic signals on the order of 0.3 volts p/p. Hence, from this limited data, the signal levels (in volts) are approximately the same as the particle diameter (mm). For a 100 micron particle, the initial signal level should then be approximately 100 mV p/p.

The loss factor measured for these samples was about 0.13% for these 25 cm square plates. While much of this loss is due to reflection losses at the plate edges, this loss factor sets a maximum allowable signal reduction with propagation distance. Using this and the lowest speed estimate (for a plate wave in aluminum) of 1350 m/sec, the initial signal decreases to 10% of its initial level in 8.8 m (6.5 msec), 1% in 18 m (13.1 msec), and 0.1% in 27 m (19.6 msec).

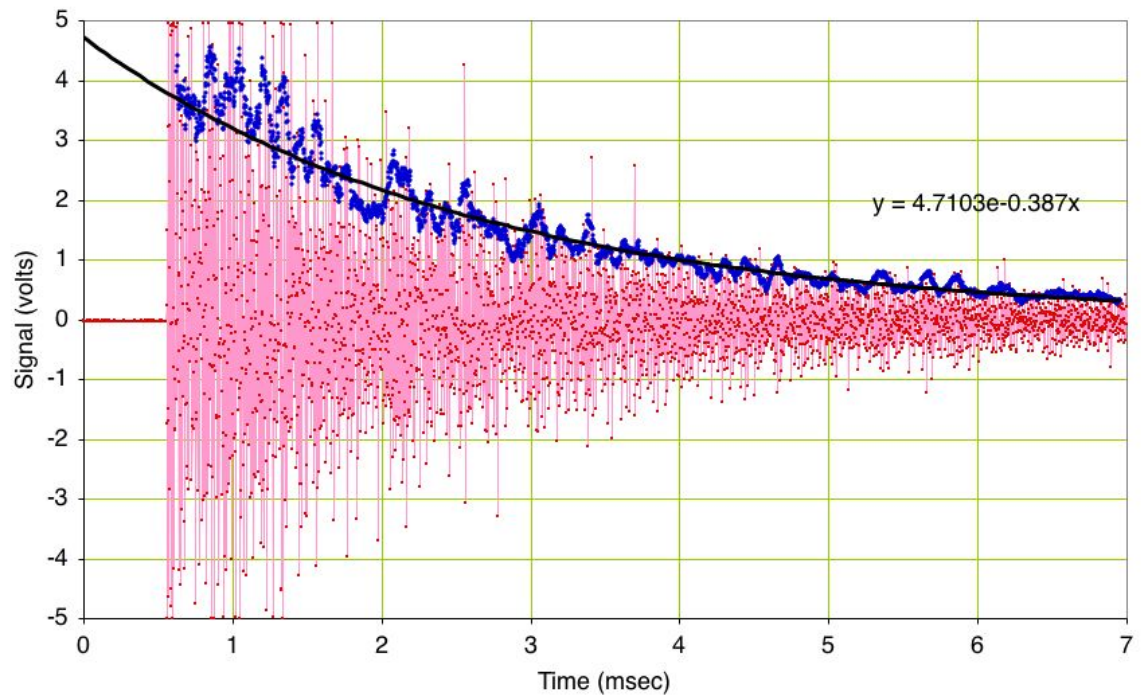


Figure 7-8. Typical signal from impact with aluminum plate (with envelope and exponential fit).

A second factor is signal loss due to spreading. In this test, the sensors were placed approximately 10 cm from the point of impact. Signal amplitude in the plate will decrease approximately as the square root of the distance (due to “cylindrical spreading”). Hence, it will be reduced to 10% of its original magnitude at a distance of 10 meters.

Considering the two sources of signal loss, for a 100 micron particle striking at a distance of 10 meters from the sensor, we expect 10% reduction from spreading and no more than an additional 99% reduction due to damping. Hence, the final signal level will be 0.1 mV p/p. This is approximately the anticipated noise floor of a reasonably quiet facility or platform. (The actual background noise level at the facility used in these tests was 1.3 mV; however, the system has also been used in quieter facilities approaching the limiting system noise level of 0.003 mV.) This corresponds to a detection capability at 10 m range for a 100 micron particle.

The above is for detection on a bare aluminum plate with uniform impedance. When impedance discontinuities are present (i.e., support frames or ribs), a portion of the signal will be reflected and another portion will be lost due to mode conversion into more dissipative waves. Hence, the detection range will be reduced. This topic requires additional study, but an initial suggestion is that each frame support may reduce signal intensity by 20%.

An initial set of measurements has been performed on the small-scale test structure, fabricated to include the features of one proposed lunar habitat (figure 7-9). These measurements support the above conclusions [59].



Figure 7-9. Small-scale test structure designed to evaluate signal propagation.

The presence of MLI thermal blankets will have two influences. They will add a small additional contribution to the damping (loss factor) and will slow (and possibly break) the incoming particle. Hypervelocity tests with 1 mm particles developed acoustic signals of approximately 0.8 V p/p on the aluminum layers, and of 0.10 V p/p on the Kapton outer cover layer. This suggests a potentially significantly reduced impact energy is available at the underlying aluminum surface. Additionally, while the hole formed in the front Kapton layer was 1 mm diameter, the hole in the final aluminum foil layer was 3 mm diameter. Either significant mass of the MLI material is breaking off and also impacting the underlying surface, or (less likely) the particle is breaking up. Unfortunately, the signals formed on aluminum plates when covered with thermal blankets has not yet been measured.

The above suggests a rough design formula for the sensor layout. For impact detection, we need sensors separated by no more than five frame supports or no more than 10 meters distance (whichever is less). For localization, we need four sensors, preferably separated by no more than three frame supports to reduce complicating reflections. These estimates are tentative and should be refined by additional tests. However, based on the data in hand, we can make an estimate. If we consider a cylindrical structure, with a

diameter of 8 m and a length of 36 m, placed on its side, then this structure would have a top side area of about 400 m². If hull supports are placed every meter and bulkheads every 4 m, then this structure would require approximately 32 sensors. With 100% sensor system redundancy, the mass of our system would be approximately 2 kg. Its power consumption would be 1 w. The system would be capable of detecting a HVI by large (ca. 100 micron) particles and would provide a localized position for the impact. This system could be monitored by a single dedicated microprocessor system, or the data could be fed into the structure's own housekeeping computer for analysis. The detection threshold could be adjustable or it could be fixed depending on the experience gained and the particular application.

7.2.3 Acoustic Sensor Application Considerations for Inflatable Modules

Test data were also collected for sensors mounted on other materials (HDPE, Kevlar fabric, etc.) which might find use in shielding applications. Signal levels from these sensors are also satisfactory, though losses are higher. If such material is used to shield the structure, and we monitor impacts directly from such material, the sensors would probably have to be more closely spaced than would be the case if the aluminum structure was directly monitored. The number of sensors required would depend, in some measure, on how the shielding material was attached to the structure and to adjacent shielding.

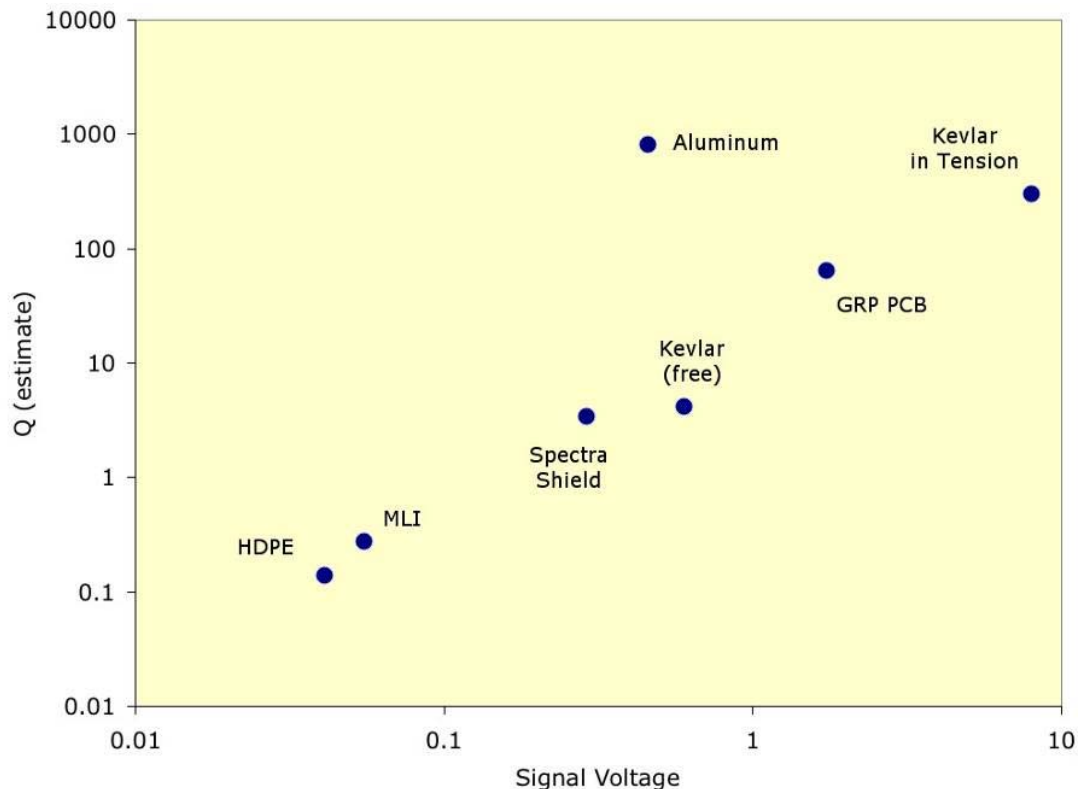


Figure 7-10. Measured signal voltage and Q for hypervelocity 1 mm particle impacts. (Q is the inverse of the loss factor.)

7.3 Fiber Optic Micrometeoroid Impact Sensor

The Fiber Optic Micrometeoroid Impact Sensor (FOMIS) was originally developed as a very low-mass, large-area instrument for particle flux measurements in space or lunar environments, with initial emphasis on inflatable structures and sails. It consists of a thin polymer or metal film in tension. When a particle strikes the film, it behaves as a drum and vibrates. Because of its resonant structure, the motions induced are relatively large and occur at well-defined frequencies. The vibratory motion of this film is then detected by a non-contact Fiber Optic Displacement (FOD) sensor. For particles sufficiently large to penetrate the film (i.e., greater than 10 micron) the signal amplitude is related to particle size. Also, since only these larger particles will pass through the film, it can serve as a particle size-filter for any other sensors placed below.

The FOD sensors are commercially available for other applications. However, the system developed for the FOMIS application was optimized at the Naval Research Lab for low power and mass, and for measuring motions as large as 1 mm with 1 Angstrom resolution. These sensors are small, non-contact glass fiber probes, which inherently are essentially unaffected by temperature or radiation. As shown in figure 7-11, the sensor end of the optical fiber bundle is positioned in proximity to an optically reflective surface. A light-emitting diode, located at the other end, sends light down a central fiber in the bundle. Reflected light is returned in the outer fibers. Only the intensity of the reflected signal is measured, which is linearly related to the separation distance over small distances.

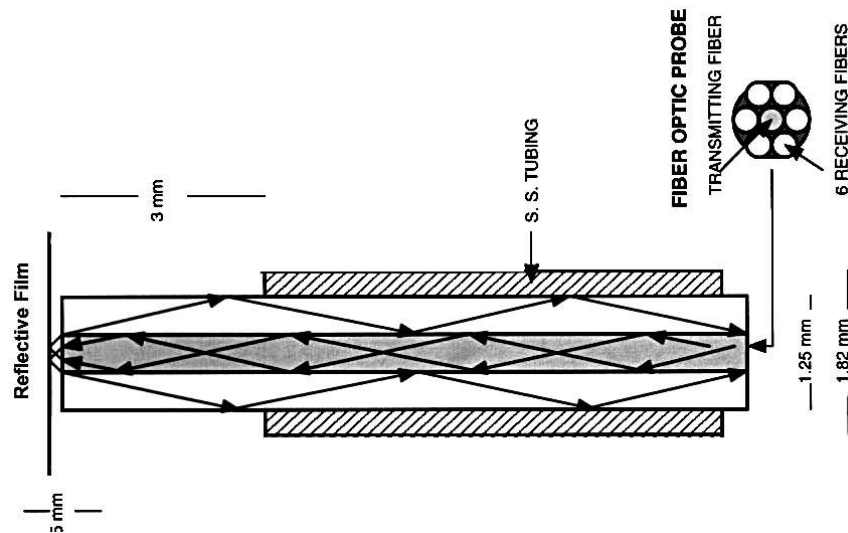


Figure 7-11. Fiber optic displacement sensor (exaggerated size).

The impact target material (drum head) was originally a thin, lightweight aluminized Mylar film. However, in HVI tests, the sensors have demonstrated a wider applicability. They have been successfully used with woven Kevlar fabric (under tension), as well as aluminum sheets, and are generally applicable to any material that transmits bending-type vibrations (i.e., out-of-plane motion). The sensitivity of the instrument will depend on the thickness and type of material used. For thin Mylar film,

the detection threshold (from statistical fluctuation theory) is a hypervelocity particle 0.5 micron diameter. For a thick woven fabric, it is obviously higher. This is supported by the measurements performed in the HVI facility at the University of Kent, using the fabric and sensor holders shown in figure 7-12.



Figure 7-12. Test unit containing three sensors (one shown), for HVI studies.

The voltage output from the detector is typically an audio-frequency signal lasting less than one second. In laboratory tests, this signal is captured and processed. For spacecraft use, it would be sufficient to use a peak-hold analog circuit to capture the amplitude, and pass only this DC voltage level to the spacecraft system for storage and transmittal. The power requirement of the system is approximately 300 mW continuous, which can support up to 18 sensors. If deployed as a stand-alone mechanical structure, the mass will largely be that of the tensioning ring; total mass is estimated as 3 kg per square meter of aperture. If designed as an attached structure, or an inflatable, the required mass is much less.

The FOMIS system has proven reliability and ruggedness, and is similar to other FOD systems used in commercial applications. However, it has not flown or been qualified for spacecraft use. The principal development needed would be designing a low-mass support, and the mechanical and electrical interface to the spacecraft. Consequently, it is estimated that this system is at TRL-4, but at an advanced stage at that TRL. It is anticipated that TRL-5 can be achieved in the very near future.

7.4 Resistive Grid Sensor System

The Resistive Grid Sensor (RGS) is a passive dust particle-flux measuring device capable of directly measuring particle size. It was originally designed as a very robust system requiring little system resources (i.e., mass, power, telemetry). Its development emphasized large particles (greater than 50 micron) that might pose a hazard to space assets. It is anticipated that the RGS would be deployed over a large area to acquire adequate statistics of the flux of the less-abundant larger particles. The RGS relies on a simple concept for its functionality. Thin resistive lines, lying in parallel, are produced by a lithographic process on a suitable space-qualified substrate. Approximately 1000 resistive lines that are 75 micron wide and 15 cm long, separated by a 75 micron gap can be consistently produced by standard present technology. Several grids have been made to this specification. The 1000 parallel lines are linked to buses, as illustrated in figure 7-13, to create a sensitive pad measuring about 15 cm x 15 cm.

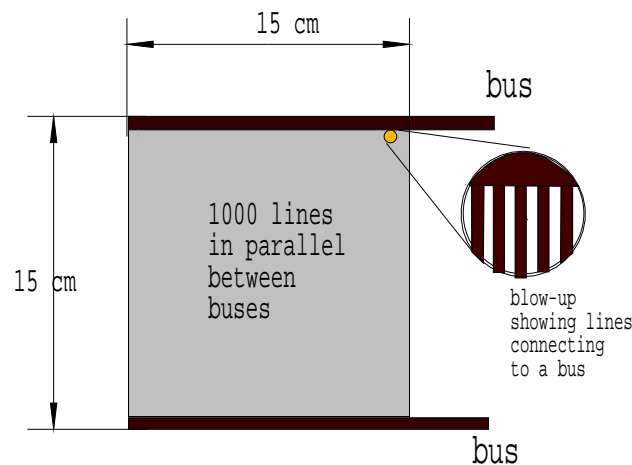


Figure 7-13. RGS.

The sensor relies, for its functionality, on the physical action of a hypervelocity particle on impacting a surface. In the size regime for which the sensor was developed two basic interactions can occur, depending on the thickness of the substrate on which the RGS is mounted and the characteristic of the particle. Either the particle will penetrate or it will cavitate the substrate, destroying an area from 3 to 10 times its diameter. If the particle is sufficiently large, greater than 50 micron, it will destroy one or more of the resistive grid lines in this process. By measuring the resistance of the sensor (between the buses) the number of lines destroyed can be determined and, therefore, a measure of the size of the impacting particle. Resistance measurements can be made at intervals or when other instruments (such as PINDROP) indicate an impact. The resistance is then compared with previous measurements (corrected for temperature) to determine the number lines destroyed by the impact. Generally, particles smaller than 10 micron will erode the grid lines, but these will not destroy an entire line; in this case, the change in resistance of the RGS will be very small (and will not be mistaken for a line break even if many small particles impact the sensor between resistance measurements). Particles in between 10 and 50 micron may, with statistical predictability, take out a single line.

Whereas 50 micron and greater hypervelocity particles of any significant density will always take out one or more lines.

Because each RGS is only 15 cm x 15 cm, several RGSs are tiled (typically on the same backing substrate) to form a larger sensor area. As with other sensors, the sensor area needed depends on the mission duration and the anticipated particle flux of the largest particles of interest. The electronics to measure resistance of an RGS consists of a voltage reference and a 12 bit A/D. A microprocessor is used to control the measurement and record the data for download. Only one voltage reference and A/D is required for the entire RGS array since the measurement is infrequent and multiplexed.

The mass of an RGS system with a 1 m² area would be 1.1 kg (using the current configuration of a 0.5 mm G10 epoglass board with carbon fiber honeycomb support). Electronics, housing, and wire would add another 0.7 kg. Power requirements of the system during measurements would be 32 mw for about 1 sec. If resistance measurements were made once an hour, the total electrical energy requirement (without heaters) would be the quiescent consumption of the microprocessor.

To date, the RGS has not flown. It is under development as part of the DoD Space Test Program Debris Resistive Acoustic Grid Orbital Navy Sensor – or DRAGONS – mission, a 1-year, 800 km to 1000 km altitude flight. The RGS has been built and subjected to hypervelocity testing. Figure 7-14 shows the effect of a 100 micron glass particle at 5 km/s. The RGS array relies completely on available and proven technology, and since its construction is static, robust, and very straightforward, its implementation for a 2010 delivery should not be difficult. The principal development issue envisioned is likely to be the interface to a spacecraft and the placement of a sufficient area to obtain statistically significant data. It has not yet been interfaced with realistic electronics and is, therefore, considered to be at TRL-4, but the path to TRL-5 is straightforward and is expected to be reached shortly.

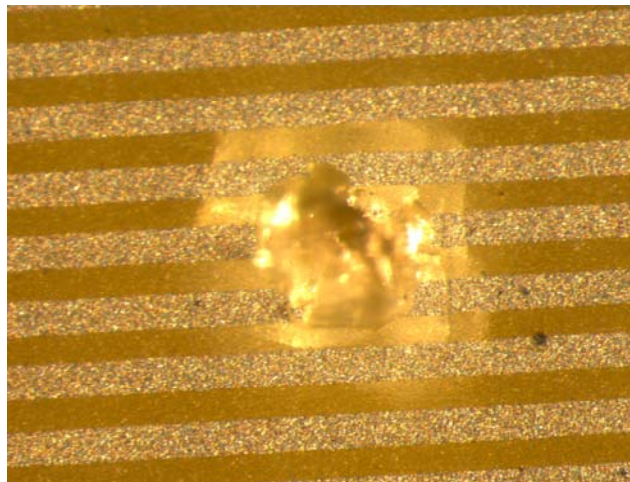


Figure 7-14. Damage from a 100 um glass hypervelocity impact.

7.5 Micrometeoroid Impact Detection System

The basic configuration of Micrometeoroid Impact Detection System (MIDS) includes a solid metal plate with a dimension of 1 m x 1 m, and a thin film under tension placed about 1 cm above the plate (figure 7-15). The sensor suite consists of PINDROP acoustic sensors to detect the signals generated by particle impacts with the bottom plate, and FOD sensors to measure film motion caused by particles impacting or penetrating the film. The thin film also serves to filter out smaller and slower secondary ejecta from impacting the metal plate, and also to filter out charged lunar fines, such as those that contaminated the Apollo 17 Lunar Ejecta and Meteorite experiment. In addition, the thickness of the thin film can be varied for different 1 m x 1 m units. Since the velocity distribution of micrometeoroids does not vary significantly from a few microns to several hundred microns, the thickness of the film can be used to place constraints on the minimum mass threshold for micrometeoroids penetrating the film, then hitting the metal plate.

The thin film layer of MIDS monitored by the FOMIS detector provides a good indication of particle diameter, while the aluminum plate monitored by PINDROP reacts to energy or momentum of the particle (dependent on configuration parameters of the structure). If the film and plate can be separated by tens of centimeters and the impact location of the impact on both the film and aluminum plate determined by the acoustic propagation, then the velocity of the particle can be determined. When combined with the diameter and momentum or energy, the density of the impacting particle can be deduced. The TRL for MIDS is estimated to be somewhere between TRL 2 and 3.

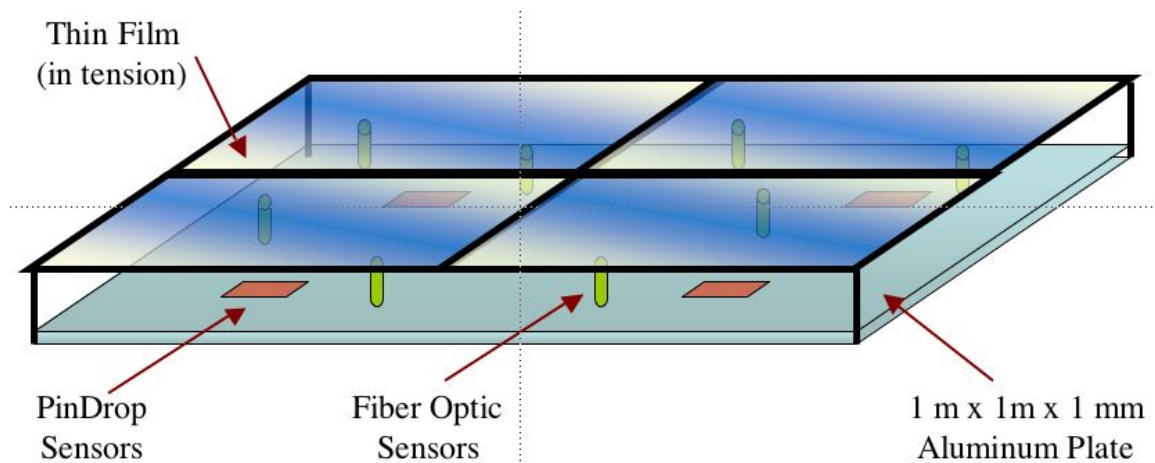


Figure 7-15. MIDS.

7.6 Debris Resistive Acoustic Grid Orbital Navy Sensor

This sensor system combines the RGS with the PINDROP acoustic sensors. One possible configuration has been constructed and tested with HVIs. It consists of a circuit board with resistive grids imprinted on one side, and PINDROP acoustic sensors attached to the other (back) side. The impact of a hypervelocity particle destroys lines proportional to the diameter of the particle while the acoustic sensor records signals related to impact momentum/energy. In addition to impact flux, the combined data could lead to an estimation of the density and mass of each impacting particle.

7.7 Secondary Ejecta Detection System and Dual-Layer Optical Curtain Sensor

The basic configuration of Secondary Ejecta Detection System (SEDS) includes a Dual-Layer Optical Curtain Sensor (DOCS) and the PINDROP acoustic sensors that are attached to a solid plate behind the second optical curtain of the DOCS. The SEDS is designed to characterize the impact flux, velocity, size, mass, and density of the detected secondary ejecta particles.

To better measure the lunar secondary ejecta environment, a DOCS can be developed. Its design is based on the Grain Impact Analyzer and Dust Accumulator dust flux instrument developed for the European Space Agency (ESA) Rosette mission. Although this system has been satisfactorily flown, changes in the electronics and configuration for better lunar secondary ejecta detection are needed. Therefore, DOCS can be considered to be at TRL-7. The principal disadvantage of DOCS is its small area and relatively high power consumption. However, since the secondary ejecta flux is several orders of magnitude higher than that of the micro-meteoroid background, the small sensing area (hundreds of cm^2) is adequate to monitor the secondary ejecta environment.

The operation of the DOCS system depends on lunar secondary ejecta passing through two separate light curtains. The resulting scattered light from each layer is recorded by photometers. The data can be analyzed to estimate the impact speed and the size of the particle. PINDROP will also be added below the second curtain to establish the approximate position of the particle through the light beam, providing a correction to the intensity measured as the particle transits each light beam. In addition to the position determination, the acoustic signals provide an estimate of the momentum of the particle. Thus, knowing the velocity from the light curtain passage, and the momentum from the acoustic sensors, the mass of the particle can be estimated. Knowing the mass and size of the ejecta particle, its density can be estimated. Although the density is not expected to show great variation, it may aid our understanding of the regolith formation. The DOCS design will optimize the determination of the velocity, size, mass, and density (in order of decreasing accuracy) of the secondary ejecta. By keeping the internal scattering to a minimum, particles of at least 1 micron moving at 100 m/sec can be detected and fully characterized, and that for particles as small as a few tenths of a micron, velocities can be determined.

8 Concluding Remarks

This report provides guidelines for design and implementation of effective MMOD protection. Important aspects of MMOD protection system design include: (1) performing risk assessments to identify regions of the vehicle that drive MMOD risk; and (2) evaluating design and operational methods to reduce MMOD risk, focusing on the MMOD risk drivers.

Based on knowledge gained by NASA in implementing MMOD protection for ISS and other spacecraft, multi-wall shields provide more effective MMOD shielding than single- or two-wall MMOD shields. For instance, Nextel/Kevlar stuffed Whipple shields are lighter, and provide higher levels of MMOD protection than all-aluminum 2- or 3-wall shields.

Detecting and locating damage to critical hardware and the rear walls of MMOD shields can reduce the risk from MMOD impact. Significant progress has been made in developing MMOD impact sensors. Consideration should be given in future vehicle programs to add requirements to integrate damage detection and location sensors into MMOD shields.

Periodic updates to this report will be made in the future as new data is obtained and new MMOD protection solutions are evaluated and characterized.

9 References

1. B.J. Anderson (Ed.) and R.E. Smith (Compiler), Natural Orbital Environment Guidelines for Use in Aerospace Vehicle Development, NASA TM 4527, 1994.
2. H. McNamara, J. Jones, B. Kadfhan, R. Suggs, W. Cooke, S. Smith, Meteoroid Engineering Model (MEM): A Meteoroid Model for the Inner Solar System, 2004.
3. J.-C. Liou, M.J. Matney, P.D. Anz-Meador, D. Kessler, M. Jansen, and J.R. Theall, The New NASA Orbital Debris Engineering Model ORDEM2000, NASA TP-2002-210780, 2002.
4. NASA, Meteoroid Environment Model, Space Station Program Natural Environment Definition for Design, SSP-30425, Rev.B, 1993.
5. E.L. Christiansen, Space Station Freedom Debris Protection Techniques, Advances in Space Research, Vol. 13, No.8, pp.(8)191-(8)200, 1993, (Proceedings of the 29th COSPAR, August 1992).
6. J.P. Loftus, D.J. Pearson, and E.L. Christiansen, Orbital Debris Risk Assessments and Collision Avoidance Procedures for the Space Shuttle, IAA-97-IAA.6.5.03, 48th International Astronautical Congress, October 1997.
7. A.I. Nazarenko, V.P. Romanchenkov, V.G. Sokolov, and A.V. Gorbenko, Analysis of the Characteristics of Orbital Debris and the Vulnerability of an Orbital Station's Structural Elements to Puncture, Space Forum, Vol. 1, pp. 285-295, ISBN 90-5699-072-1, 1996.
8. J.L. Hyde and E.L. Christiansen, Space Shuttle Meteoroid & Orbital Debris Threat Assessment Handbook: Using the BUMPER-II Code for Shuttle Analysis, JSC-29581, 2001.
9. F. Whipple, Meteorites and Space Travels, Astronomical Journal, no.1161, p. 131, 1947.
10. E.L. Christiansen, Meteoroid/Debris Shielding, NASA TP-2003-210788, 2003.
11. NASA SP-8042, Meteoroid Damage Assessment, Space Vehicle Design Criteria (Structures), May 1970.
12. Inter-Agency Space Debris Coordination Committee Working Group #3, MMOD Protection Manual, version 3.3, 2004.

13. E.L. Christiansen, Design Practices for Spacecraft Meteoroid/Debris (M/D) Protection, Hypervelocity Shielding Workshop Proceedings, Institute of Advanced Technology Catalog Number IAT.MG-0004, 1999.
14. E.L. Christiansen, J.L. Hyde, and G. Snell, Spacecraft Survivability in the Meteoroid and Debris Environment, AIAA Paper No. 92-1409, 1992.
15. J.L. Crews and E.L. Christiansen, "The NASA JSC HITF," AIAA Paper No. 92-1640, 1992.
16. F. Terrillon, H.R. Warren, and M.J. Yelle, Orbital Debris Shielding Design of the RADARSAT Spacecraft, IAF-91-283, 1991.
17. NASA, CxP 70023, Constellation Program Design Specification for Natural Environments, December 15, 2006.
18. B.G. Cour-Palais, Hypervelocity Impact in Metals, Glass, and Composites, International Journal of Impact Engineering, 10, 135-146, 1990.
19. B.G. Cour-Palais, Hypervelocity Impact Investigations and Meteoroid Shielding Experience Related to Apollo and Skylab, in Space Debris, NASA Conference Publication 2360, 247-275, 1982.
20. E.L. Christiansen, E. Cykowski, and J. Ortega, Highly Oblique Impacts into Thick and Thin Targets, International Journal of Impact Engineering, 14, 157-168. 1993.
21. F. Schaefer, E. Schneider, M. Lambert, Review of Ballistic Limit Equations for CFRP Structure Walls of Satellites, 5th International Symposium on Environmental Testing for Space Programmes, ESA SP-558, Noordwijk, June 15-17, 2004.
22. M. Ratliff, Single-wall equation for titanium shield, NESC Study of meteoroid protection for JWST cryogenic harnesses, May 2008 (included in final NESC report: James Webb Space Telescope [JWST] Integrated Science Module (ISIM) Electrical Cable Protection, August 2008).
23. F. Lyons, S. McMurray, E. Christiansen, JSC-62803, Return to Flight (RTF) Hypervelocity Testing on Impact Penetration Sensor System (IPSS), Medium and High Fidelity Testing on Fiberglass and Reinforced Carbon-Carbon Panels, March 2005.
24. E. Christiansen, unpublished data, 1990-2008.
25. A. Davis, *et al.*, Hypervelocity Impact (HVI) Test Plan for Crater Characterization for Cut Glove Investigation (Plate Testing), April 2008.

26. F. Hörz, M.J. Cintala, Penetration Experiments in Aluminum 1100 Targets by Soda-Lime Glass Projectiles, NASA TM-104813, 1995.
27. R. Kinslow (ed): High-Velocity Impact Phenomena, Academic Press, New York, 1970.
28. B.G. Cour-Palais, A Career in Applied Physics: Apollo through Space Station, International Journal of Impact Engineering, 23, 137-168, 1999.
29. H.F. Swift, Hypervelocity Impact Mechanics, In: Impact Dynamics (Zukas, ed.), John Wiley & Sons, 1982.
30. C.J. Maiden, J.W. Gehring, A.R. McMillian, Investigation of Fundamental Mechanism of Damage to Thin Targets by Hypervelocity Projectiles, NASA TR-63-225, 1963.
31. A.K. Hopkins, T.W. Lee, and H.F. Swift, Material Phase Transformation Effects Upon Performance of Spaced Bumper Systems, Journal of Spacecraft and Rockets, 9, 342-345, May 1972.
32. M.L. Alme and C.E. Rhoades, A Computational Study of Projectile Melt in Impact with Typical Whipple Shields, International Journal of Impact Engineering, 17, 1-12, 1995.
33. M.L. Alme, E.L. Christiansen, and B.G. Cour-Palais, Hydrocode Simulations of the Multi-Shock Meteoroid and Debris Shield, Proceedings of the APS 1991 Tropical Conference on Shock Compression in Condensed Matter, Williamsburg, VA, 1991.
34. E.L. Christiansen, Design and Performance Equations for Advanced Meteoroid and Debris Shields, International Journal of Impact Engineering, 14, 145-156, 1993.
35. H.-G. Reimerdes, D. Nölke, F. Schäfer, Modified Cour-Palais/Christiansen Damage Equations for Double-Wall Structures, International Journal of Impact Engineering, 33, 645-654, 2006.
36. NASA SP-8042, Meteoroid Damage Assessment, Space Vehicle Design Criteria (Structures), May 1970.
37. A.J. Piekutowski, Fragmentation initiation threshold for spheres impacting at hypervelocity, International Journal of Impact Engineering, 29, 563-574, 2003.
38. E.L. Christiansen, Ballistic Limit Equations for Node 2/3 Whipple Shields, version I, internal NASA memo, 9 November 2006.

39. R. Destefanis, M. Faraud, "Node 3 PNP Assessment Report," Alenia Technical Report: N3-RP-AI-0020, issue 3, 29 July 2005.
40. E.L. Christiansen, J.L. Crews, J.E. Williamsen, J.H. Robinson, A.M. Nolen, Enhanced Meteoroid and Orbital Debris Shielding, *International Journal of Impact Engineering*, 17, 217-228, 1995.
41. E.L. Christiansen, et al., Hypervelocity Impact Testing Above 10km/s of Advanced Orbital Debris Shields, *Shock Compression of Condensed Matter – 1995*, AIP Conference Proceedings 370, Part 2, pp.1183-1186, 1995.
42. J.L. Crews and B.G. Cour-Palais, US Patent Number 5,067,388, Hypervelocity Impact Shield, 1991.
43. B.G. Cour-Palais and J.L. Crews, A Multi-Shock Concept for Spacecraft Shielding, *International Journal of Impact Engineering*, 10, pp. 95-106, 1993.
44. J.L. Crews, E.L. Christiansen, J.H. Robinson, J.E. Williamsen, A.M. Nolen, US Patent Number 5,610,363, Enhanced Whipple Shield, 1997.
45. E.L. Christiansen and J.H. Kerr, Mesh Double-Bumper Shield: A Low-Weight Alternative for Spacecraft Meteoroid and Orbital Debris Protection, *International Journal of Impact Engineering*, 14, pp.169-180, 1993.
46. E.L. Christiansen, Advanced Meteoroid and Debris Shielding Concepts, AIAA Paper No. 90-1336, AIAA/NASA/DOD Orbital Debris Conference: Technical Issues and Future Directions, Baltimore, MD, April 16-19, 1990.
47. E.L. Christiansen, International Space Station (ISS) Meteoroid/Orbital Debris Shielding, *Cosmonautics and Rocket Engineering*, Russian Academy of Sciences, TsNIIMASH, No.18, pp.166-180, 2000.
48. Interagency Space Debris Coordination Committee, Protection Manual, version 3.3, 2004, http://www.iadc-online.org/index.cgi?item=docs_pub .
49. E.L. Christiansen and L. Friesen, Penetration Equations for Thermal Protection Materials, *International Journal of Impact Engineering*, 20, pp. 153-164, 1997.
50. E.L. Christiansen, D.M. Curry, J.H. Kerr, E. Cykowski, and J.L. Crews, Evaluation of the impact resistance of reinforced carbon-carbon, *Proceedings of the ninth International Conference on Composite Materials (ICCM-9)*, 1993.
51. E.L. Christiansen and J. Ortega, Hypervelocity impact testing of Shuttle Orbiter thermal protection system tiles, AIAA Paper No. 90-3666, 1990.

52. E.L. Christiansen, R. Bernard, J. Hyde, J.H. Kerr, K.S. Edelstein, J.L. Crews, Assessment of high velocity impacts on exposed Space Shuttle surfaces, Proceedings of the First European Conference on Space Debris, ESA SD-01, pp. 447-452, 1993.
53. R.R. Burt and E.L. Christiansen, Hypervelocity Impact Tests of X-38 Crew Return Vehicle (CRV) Thermal Protection Materials, Part III, JSC Report JSC-28121, 2001.
54. B.G. Cour-Palais, A Career in Applied Physics: Apollo through Space Station, International Journal of Impact Engineering, 23, pp.137-168, 1999.
55. J.L. Crews and E.L. Christiansen, The NASA JSC HITF, AIAA Paper No. 92-1640, 1992.
56. F. Terrillon, H.R. Warren, and M.J. Yelle, Orbital Debris Shielding Design of the RADARSAT Spacecraft, IAF-91-283, 1991.
57. B.G. Cour-Palais, Hypervelocity Impact in Metals, Glass, and Composites, International Journal of Impact Engineering, 5, pp. 221-237, 1987.
56. E.L. Christiansen and R.R. Burt, Hypervelocity Impact Testing of Transparent Spacecraft Materials, HVIS 2003, International Journal of Impact Engineering, 2003.
57. R.R. Burt, E.L. Christiansen, and J.H. Kerr, Pre-declared HVI Testing of ISS Hatch Window Cover, NASA Report JSC-29411, 2001.
58. T. Byers, F. Gibbons, and E.L. Christiansen, MMOD Strike Detector, NASA Tech Briefs, July 2008.
59. J.C. Liou, Estimated Acoustic Sensor Capability on Aluminum Structure, NASA JSC KX unpublished report, 2008.

REPORT DOCUMENTATION PAGE			Form Approved OMB No. 0704-0188	
Public reporting burden for this collection of information is estimated to average 1 hour per response, including the time for reviewing instructions, searching existing data sources, gathering and maintaining the data needed, and completing and reviewing the collection of information. Send comments regarding this burden estimate or any other aspect of this collection of information, including suggestions for reducing this burden, to Washington Headquarters Services, Directorate for Information Operations and Reports, 1215 Jefferson Davis Highway, Suite 1204, Arlington, VA 22202-4302, and to the Office of Management and Budget, Paperwork Reduction Project (0704-0188), Washington, DC 20503.				
1. AGENCY USE ONLY (Leave Blank)		2. REPORT DATE June 2009		3. REPORT TYPE AND DATES COVERED NASA Technical Memorandum
4. TITLE AND SUBTITLE Handbook for Designing MMOD Protection			5. FUNDING NUMBERS	
6. AUTHOR(S) Dr. Eric L. Christiansen Contributors: Jim Arnold, Alan Davis, James Hyde, Dana Lear, J.-C. Liou, Frankel Lyons, Thomas Prior, Martin Ratliff, Shannon Ryan, Frank Giovane, Bob Corsaro, George Studor				
7. PERFORMING ORGANIZATION NAME(S) AND ADDRESS(ES) Lyndon B. Johnson Space Center Houston, Texas 77058			8. PERFORMING ORGANIZATION REPORT NUMBERS S-1038	
9. SPONSORING/MONITORING AGENCY NAME(S) AND ADDRESS(ES) National Aeronautics and Space Administration Washington, DC 20546-0001			10. SPONSORING/MONITORING AGENCY REPORT NUMBER TM-2009-214785	
11. SUPPLEMENTARY NOTES				
12a. DISTRIBUTION/AVAILABILITY STATEMENT Available from the NASA Center for AeroSpace Information (CASI) 7121 Standard Hanover, MD 21076-1320 Category: 18			12b. DISTRIBUTION CODE	
13. ABSTRACT (Maximum 200 words) Spacecraft are subject to micro-meteoroid and orbital debris (MMOD) impact damage which have the potential to degrade performance, shorten the mission, or result in catastrophic loss of the vehicle. Specific MMOD protection requirements are established by NASA for each spacecraft early in the program/project life to ensure the spacecraft meets desired safety and mission success goals. Both the design and operations influences spacecraft survivability in the MMOD environment, and NASA considers both in meeting MMOD protection requirements. The purpose of this handbook is to provide spacecraft designers and operations personnel with knowledge gained by NASA in implementing effective MMOD protection for the International Space Station (ISS), Space Shuttle, and various science spacecraft. It has been drawn from a number of previous publications, as well as new work. This handbook documents design and operational methods to reduce MMOD risk. In addition, this handbook describes tools and equations needed to design proper MMOD protection. It is a living report in that it will be updated and re-released periodically in future with additional information.				
14. SUBJECT TERMS spacecraft design, micrometeoroids, space debris, shielding, protection			15. NUMBER OF PAGES 152	16. PRICE CODE
17. SECURITY CLASSIFICATION OF REPORT Unclassified	18. SECURITY CLASSIFICATION OF THIS PAGE Unclassified	19. SECURITY CLASSIFICATION OF ABSTRACT Unclassified	20. LIMITATION OF ABSTRACT Unlimited	
